Low Emission AMTEC Automotive Power System

Final Report for

Department of Energy Contract
DE-FG02-94ER81696

Prepared by Thomas K. Hunt

Advanced Modular Power Systems, Inc.
4370 Varsity Drive
Ann Arbor, Michigan 48108

17 April 2001

DOE Patent Clearance Granted
4/22/01
Date

Daniel D. Park
(630) 252-2308
E-mail: daniel.park@ch.doe.gov
Office of Intellectual Property Law
DOE Chicago Operations Office

DISCLAIMER

Low Emission AMTEC Automotive Power System

1. Introduction

Air pollution from automobile exhaust is a serious problem in many urban areas in this country and there is thus a pressing need to lower vehicle emissions. Electric vehicles powered by currently practical battery systems do not have the range/performance required to make them attractive to most potential customers and are thus unlikely to make much impact on the pollution problem even if made available for general purchase. Range extension through development of Hybrid-Electric Vehicles (HEV) may greatly lower emissions while providing adequate range by using on board liquid fuels and an efficient auxiliary power unit (APU) to run and/or charge the vehicle. Conventional hybrid/electric power systems use small internal combustion (IC) engines coupled to alternators to provide steady state power for cruise and battery charging, while the batteries are utilized to provide additional power for peak loads. Unfortunately, small IC engines tend to be inefficient even under full load, often must operate on part load at much lower efficiencies and tend to have serious emission problems. Use of an external combustion converter in either a series or parallel hybrid-electric vehicle offers the possibility of extremely low emissions while maintaining acceptable range. If the hybrid system prime power source has sufficient dynamic range at high efficiency the system can also reduce the stress on the battery by using the battery only for occasional peak power thus largely eliminating frequent deep discharge cycles which can reduce battery life and lead to the high costs associated with more frequent battery replacement. AMTEC, capable of producing electric power at efficiencies comparable to small constant speed IC engine powered generator sets, uses external combustion to eliminate the high pressure, high temperature combustion which , in I.C. engines, leads to NO_x formation. External combustion as used in AMTEC systems can be accomplished at lower temperatures and atmospheric pressure with negligible nitrogen oxide formation and if done catalytically can eliminate most hydrocarbon emissions as well. It is expected that the burners appropriate for AMTEC systems will easily exceed the Tier II emissions standards. Thus AMTEC can offer a new, potentially very important new option for producing an environmentally benign vehicle.

2. Phase II Objectives

The fundamental Phase II objective was to determine whether AMTEC converters can significantly improve the efficiency and emission characteristics of vehicles. The focus is on civilian automotive power systems, but AMTEC's general performance characteristics suggest that systems for military vehicles, marine

propulsion and auxiliary power systems may also be suitable commercialization targets following the development and demonstrations proposed in Phase II. The specific technical objectives were: 1) the design, development, fabrication and testing of a subscale, multi-tube AMTEC cell at the 100 watt level. It was hoped that a cell at this power level could reach efficiency approaching 40%. This objective was not reached during this program. The laboratory operation of the 100 W module was intended to be used to validate the analytical codes for converter performance and later to test the combustor and recuperator design analysis and fabrication approach. Recognizing that a workable vehicle generator would probably be assembled from a number of modules, a second objective was the completion of a credible conceptual design of a full scale module based on the data from the subscale module tested during the program. The full scale system design was to have a peak output of 55 kWe. The conceptual design arrived at in the Phase I program is a full scale system comprised of 192, 0.3 kWe modules that could, as a unit, provide power over the range from maximum efficiency at 15 kWe part load to peak power output at 55 kWe. The minimum thermal efficiency of the AMTEC converter over this range is 30% and the peak at 40%. This design was to have had input from personnel of the Hybrid Electric Vehicle program at the Ford Motor Company to ensure that the real system constraints are maintained in the design; 3) Performance of subscale system tests; 4) Conclusion of Phase III teaming arrangements and development commitments with specific developers/manufacturers of high efficiency combustors and recuperators suitable for incorporation in the system design.
The four main objectives of the proposed Phase II effort were to be achieved by the successful completion of the following 4 major tasks:

1.) **Project Management:** Integrate the work of the subcontractors and do the required monthly, interim, and final reports. Develop plans and partners for the Phase III commercialization program. Result As a considerable result of the technical progress supported by this program interest in commercial applications of AMTEC has led to licensing of the technology to a U.S. commercial company for terrestrial applications and current discussions with two European firms for licensing to applications there.

2.) **Automotive Power System Design** Develop the Phase I conceptual design into a system design with sufficient detail to guide the design of both the AMTEC cells required and the burner and recuperator systems needed to achieve the program efficiency goals. Carry out rational comparisons between AMTEC systems and the competing technologies including fuel cells, and direct injection Diesel and Otto cycle engines. Result A full automotive converter system design was not completed and for this reason only preliminary comparisons were made with competing automotive technologies. It was deemed more valuable at this stage of AMTEC development to concentrate effort on the critical tasks in converter development in lieu of system design and fabrication.

3.) **Converter Development** Carry out design and modeling of the multi-tube cells. Complete the development of high performance cell components and their integration into complete cells. Result A variety of converter designs were conceived and several built and tested to demonstrate the capability of critical subsystems. Electrode consistency and performance were improved through the use of a newly designed, simple, test apparatus that permitted separation of the effects of anode, cathode and BASE resistence contributions. New anode compositions and deposition methods were devised, improved current collection buses for both anode and cathode were developed and a novel concept for ensuring that the entire length of the BASE tubes reaches and stays at a uniform temperature was developed and demonstrated.

4.) **System Functional Demonstration** Using the cell and system development results from the previous two tasks, develop a working module of the full system and test it for efficiency and power performance through a test cycle appropriate for vehicle operation. Result The full system at a power level suitable

for an automotive system module was not built. Smaller combustion heated systems were tested to evaluate the technologies needed for the full system. These smaller systems

3. Brief Task Summary

As the program progressed, it became clear that the major thrust of the technical work needed to be concentrated on development at the cell/converter level as that hardware was not yet ready for a full system implementation. The system design effort directed the cell component and converter development toward electrode and material innovations and to an understanding of the efficiency potential of the selected designs. Power density comparisons were made with other non-IC engine converter systems and these are reported here. During the period of performance of the Phase II program, a wide variety of advances were made, some in collaboration with efforts on other programs. Some of the relevant work carried out under other programs is reported here in order to give a more complete picture of the technology status to which this program contributed. The development of prototype modules based on portions of the work performed in this program is beginning under commercial funding as this report is written.

Important advances made during the period of performance include

1. Potassium BASE performance measurement showing higher output at lower operating temperatures
2. Internal self-heat piping which allows uniform electrolyte temperature, higher power density and retains cell to cell electrical isolation to enable series connections within the hot zone.
3. Identification of ionic current leakage paths in directly brazed BASE tube connections to cell structure.
4. An understanding of the nature of capillary pumping of alkali metals and demonstration of long-lived operation (> 14,000 hours) under load in a sodium-based system.
5. Identification of the issues related to hydrogen permeation into cells from combustion products and resolution of the problem through material choice and inclusion of getter materials in the cell chambers.
6. Measurement of the effect of high voltage in a low pressure sodium atmosphere to allay concerns about possible arc discharge when internal voltages exceed the ionization potential of the alkali metal.

4. Test Cell Design and Testing

Cell development for higher power density and higher efficiency required a rapid process for testing the new approaches to electrodes, current collection and sealing. To that end this program developed a new, simple test apparatus capable of rapid turn-around testing. This apparatus has since become the standard test vehicle for novel electrode compositions, consistency validation of electrode and current collector performance and a vehicle for thermal cycle testing including seals and current collector grids. The following section describes this apparatus and a series of tests run under this program using it.

METC Operation Testing Many of the tests of components carried out under this program were conducted, for convenience, in devices known as Mini-Electrode Test Cells (METC's). These are once-through AMTEC cells that sacrifice long term operation requiring recirculation of the alkali metal for simplicity in fabrication, testing and low cost. The standard METC cell configuration is shown in Figure 1. Several variations on this design have been used, but for each the principles are the same. The BASE tube and its components that are to be investigated is mounted on a tube support plate in the same manner as in a fully recirculating cell. Heaters are arranged outside the cell wall to heat the BASE tube by radiation and or conduction from the cell wall and the tube support plate. A reservoir for the alkali metal (AM = sodium or potassium) is heated separately so that the AM pressure can be controlled independently of the BASE temperature. The AM passing through the BASE is condensed toward the 'upper' end of the cell which is kept cold enough to freeze the AM and keep the vapor pressure in the condenser space very low. It is noteworthy that the BASE tubes can be run either in a vapor-vapor mode in which the anode (inner electrode) is in contact only with the vapor or in a liquid anode mode in which the BASE tube is filled with liquid alkali

metal. The latter situation generally leads to a very low impedance at the anode-BASE interface and so isolates the combined effects of the BASE conductivity and the cathode -BASE interfacial impedance and cathode pressure drop. Because the condenser space is quite wide open, there is a very low pressure drop to the condenser and the measurements of the BASE tube assembly and electrode are quite clean. The vapor-vapor mode corresponds to the situation required in a converter with a number of cells connected in series to raise the output voltage without shunting current through a common AM film. The small electrode areas typical of the METC testing also lend themselves to the use of AC impedance measurements which make it possible to isolate internal impedance contributions from interfaces between electrodes and the BASE and that due to the BASE conductivity itself.

Many METC tests were run in connection with this program and with other programs carried out in parallel with this. We report here on a limited number of these tests that bear on the specific goals of this Phase II program.

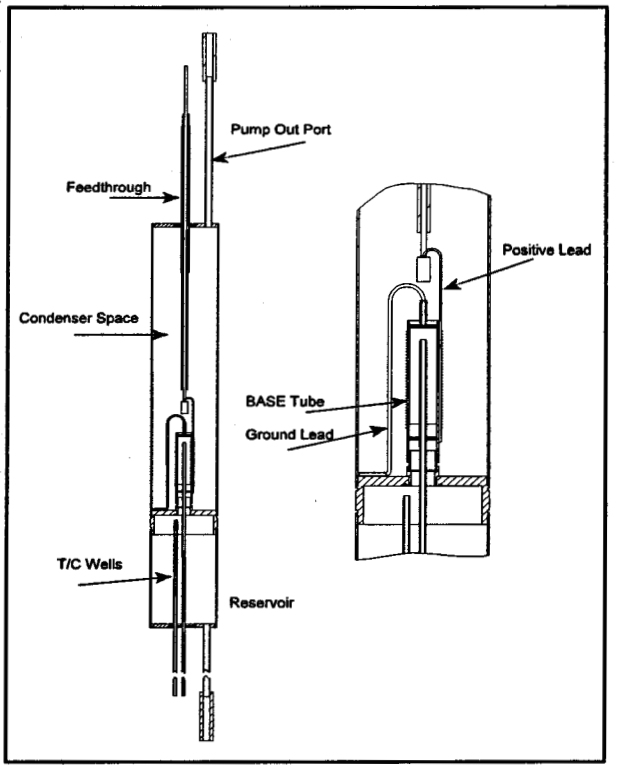

Figure 1 Mini-Electrode Test Cell.

Mini-Electrode Test Cells

Single-tube, once-through, demountable AMTEC test cells (DTC) have been used for years to permit rapid testing of electrodes. Previous versions of this type have generally utilized closed end BASE tubes with an argon cover gas to protect an O-ring seal connecting the BASE tube to the cell. Current AMTEC cell designs use, for most applications, internal series connection of BASE tube elements in order to increase cell voltage. To prevent undesirable internal shunt connections, such cells are generally operated in a vapor anode-vapor cathode mode, in which liquid sodium is not allowed to accumulate at the anode. The DTC design cannot be operated with the anode in vapor-fed mode due to the assembly methods which utilize rubber O-rings that are unable to stand the high cell temperature and sodium vapor environment. The METC apparatus used here was designed to allow both vapor-vapor and liquid-vapor operation on a single BASE tube/electrode sample run. A schematic diagram of the 'mini-electrode test cell' is shown in Figure 1. The cell consists of two chambers, a 'lower' chamber, as shown, that contains the initial sodium inventory and an 'upper' chamber into which the BASE tube intrudes and which serves as the condenser

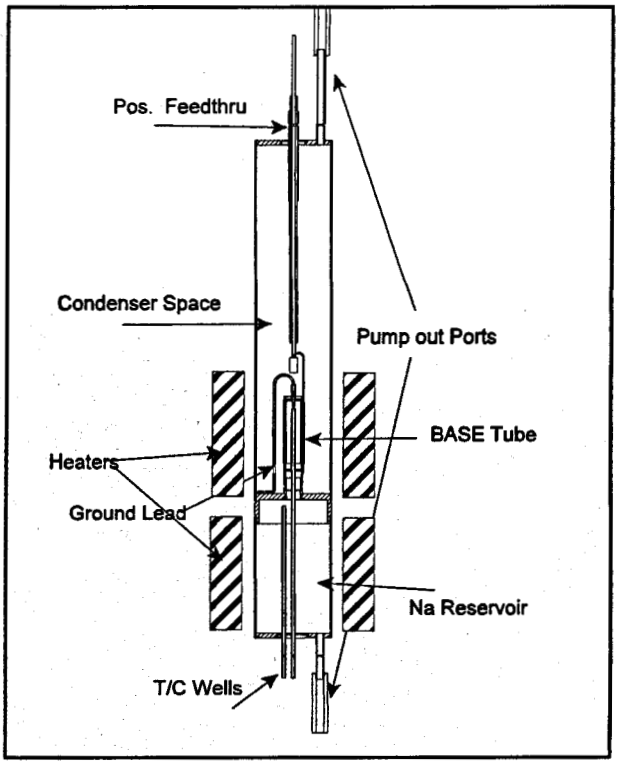

Figure 2 Standard METC Configuration.

space. The chambers are separated by the BASE tube support plate into which the BASE tube assembly is welded. The condenser end of the cell is fitted with an insulated feedthrough which is used to extract the cathode current. The two chambers are fitted with individual external shell heaters so that the sodium reservoir temperature (and thus the anode sodium vapor pressure) and the BASE temperature can be controlled independently. The BASE tube, its electrodes and current collectors can be run through the entire range of operating conditions expected to be encountered in a practical application. As a test system, the METC design has the further advantage that by simply inverting the cell and its heater assemblies as shown in Figure 2, the BASE tube can also be operated in liquid anode mode. The combined liquid and vapor anode data allow a more detailed examination of the sodium/electrode/current collector interface properties. METC testing has also been used to qualify BASE tubes from different suppliers prior to their use in complete multi-tube cells.

In normal testing, an METC sample is run through a series of reservoir and BASE tube temperature combinations and at each state, current voltage data are taken in a rapid sweep method running from open circuit conditions to short circuit and back to open circuit in approximately 5 to 10 seconds. The changes in temperature due to BASE tube cooling during high current operation generally lead to the observation of modest hysteresis in the I-V plots observed for increasing and decreasing currents. Temperature data are recorded for the reservoir and BASE tube using axial wells to allow insertion of Type-K thermocouples inside the BASE tube and reservoir chamber. The cold end and cell wall temperatures are also monitored. The I-V curves are recorded using an X-Y recorder and subsequently analyzed. Using these analyses, we can readily determine the peak power behavior and internal cell resistance as a function of temperature. The data are then used to assess the effectiveness of design modifications intended to enhance power and efficiency.

Cell Tests

METC-1 - This cell was designed to examine the electrode performance in a cell not encumbered with arteries, wicks of any sort or significant back pressure due to heat shields. It is a once through system that is nearly as simple as an AMTEC cell can get. For testing vapor-fed BASE tubes and electrodes, its function replaces that of the DTC which cannot operate in V-F mode. In addition to operating in the vapor-fed mode for which it was intended, it is also designed to be inverted about its midline so as to allow the electrodes to be run either in a liquid fed or a vapor-fed condition. Running in these two modes allows us to isolate problems due to vapor-fed issues from those due to cathode and cathode current collector performance. This cell design is substantially simpler to fabricate than the fully recirculating cells that are the current state of the art. It has the advantage of being relatively inexpensive to run and with a rapid turn around for experiments. A schematic diagram of the cell design is shown in Figure ?.

The cell was baked out for a relatively brief period with vacuum pumping from both chambers at the same time and was then loaded with 20 grams of Na to provide a reasonable running time for performance tests. In this mode, durability/lifetime tests are not feasible. The cell was mounted initially in the upright position with the sodium reservoir down so as to operate in the vapor-fed mode. Initial open circuit voltages were normal, but an abrupt decrease occurred while operating at 650°C. Following this event, the open circuit voltage responded to temperature increases but the cell, in the vapor state exhibited no significant current capability. The cell was then inverted so as to operate in the liquid-fed mode. Under these conditions it operated with an I-V curve as shown in Figure ?. The series resistance of this cell, operating in this mode can be deduced from a simple fit to the I-V curve. The resulting value is ~0.35 ohms, a value far in excess of the sum of all component resistances measured separately. This resistance is somewhat above that seen for the single tubes in the MMV-4 cell.

Conclusions The problem with operation in the V-F state appears to have been an excess of non-condensible gas in the reservoir end of the cell. This gas was trapped in the anode section of the BASE tube and prevented delivery of Na to the anode accounting for the lack of current capability. One of the principle concerns with respect to the V-F small tube multi-tube cells has been a possible problem with the anode and its current collector system. This cell, with a liquid anode appears to exhibit the same excess resistance. We make the tentative conclusion that the difficulty lies with the cathode side of the cell. There are several distinct differences between the ways that the large, MT-n cells are fabricated and the procedures used consistently for the small tubes. Significant differences may affect the cathode region. Among these are: 1) The sputtered electrode on the small tubes has been contacted by the usual copper screen wrapped, not with a continuous coil of .015" Mo wire, but with a series of approximately five 0.005" Mo wire 'tie wraps'. These appear to be substantially looser than the continuous wraps routinely used on the larger, 15 mm diameter, tubes. An increased contact resistance between the screen and its Cu buss wire and the sputtered TiN cathode may account for part of the excess resistance; 2) The sputtered TiN cathode, normally deposited prior to the active metal seal brazing operation in both small and large tubes is, for the small, short, tubes, exposed over its entire length, to the very high (~900°C) temperatures associated with the brazing operation; 3) The pressure during the two brazing operations is normally in the 1 x 10^{-6} torr range. At this pressure, oxygen contact with the sputtered electrode surface is unavoidable and a TiO_2 surface oxide layer is likely to form thus further isolating the cathode from the current collector attachments.

METC-2

In this experiment, a Ceramatec tube with a Weber anode and a sputtered TiN cathode was wrapped with a continuous 0.005" diameter moly wire holding the standard Cu screen in place. The tube was mounted in the usual fashion, baked out under vacuum at temperatures up to 650°C and then loaded with 20 grams of Na using the standard protocol for filling the recirculating cells. The cell was mounted using the two independent heaters for the Na reservoir and BASE tube.

Initial operation was carried out in the V-F mode at a range of temperatures. Current-voltage curves were taken at various points and the cell internal resistance deduced, primarily from the data at the higher currents. The maximum power points were determined from each of the I-V curves. These curves were taken rapidly so as to preserve the measured temperature through the measurement period. The deduced internal resistance values for this cell in the liquid and vapor modes of operation are plotted in Figure 3. The liquid mode clearly has a lower internal impedance, but with the limited data set in the liquid mode it appears that the impedances may be converging at higher temperatures.

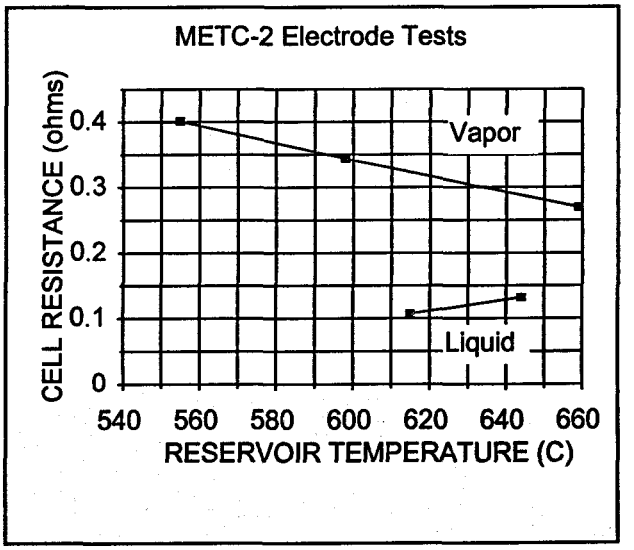

Figure 3 Effective Internal Resistance of METC 2

While the internal resistance of the METC-2 tube in vapor-fed mode is higher than that in the liquid-fed state, the peak power shows a less significant improvement for the liquid mode. It too may be converging at higher values as the temperature of the Na reservoir is increased. The power vs. temperature data are plotted in Figure 4.

Conclusions

The use of the Moly wire wrapped coil instead of the tie wrap approach seems to be beneficial. The internal resistance is substantially reduced with respect to the METC-1 cell. The power density of the tube in the vapor mode is comparable to that of the best small tube, vapor-fed cells tested thus far. The internal resistance value, however, is still significantly above the sum of impedances of all the components as measured independently. It thus appears that the cathode, its current collector and their connections, remain substantial contributors to the problem.

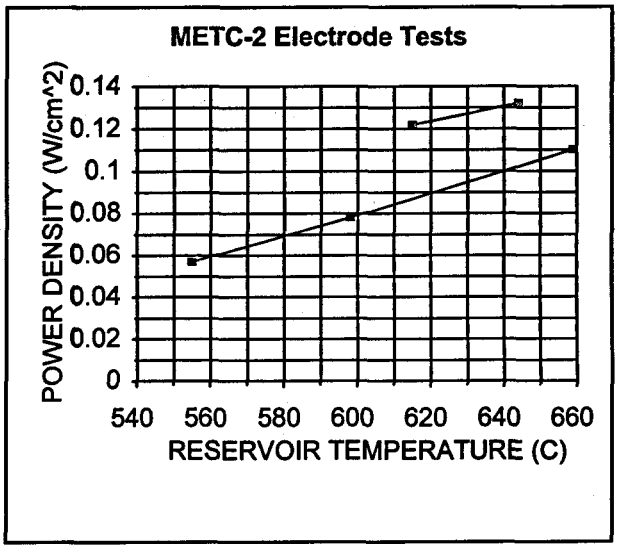

Figure 4 Power Density vs. Temperature - METC 2

The next experiment in the series will utilize a BASE tube for which the sputtered TiN cathode is deposited after the Weber electrode deposition and after the brazing of the seals at the two ends of the tube. This should prevent inducing morphological changes in the TiN electrode due to exposure to the high temperatures during the brazing operations. Possible surface oxidation of the TiN during the brazing operation should also be avoided by performing the steps in this order. The experiment will also use a BASE tube supplied by Ionotec, Ltd[1]. The wrapped cathode current collector will also be incorporated in METC-3.

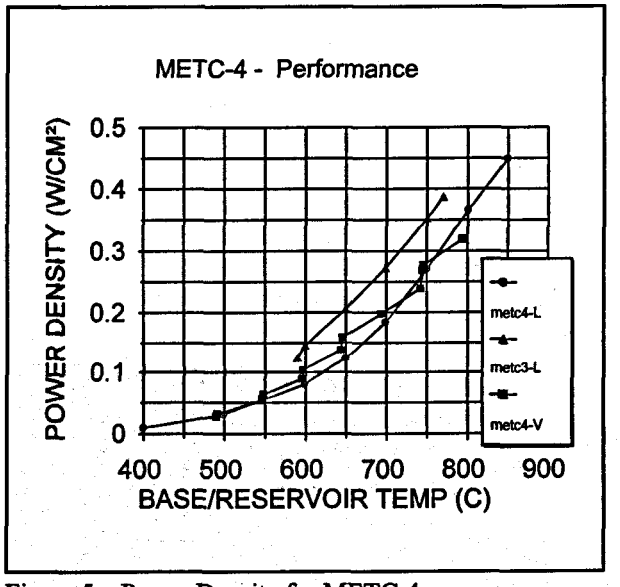

Figure 5 Power Density for METC-4.

METC-3 - This cell used a Ceramatec tube with a Weber anode and a sputtered TiN cathode. The distinction from the previous tests was that the sputter deposition of the cathode was carried out after the brazing operations used to seal the ends of the BASE tube. It was expected that this would avoid the problems with the possible overheating in vacuum of the sputtered TiN and the possible deleterious morphological changes that treatment might cause. The tube was wrapped with the 0.005" Mo wire as was the case in METC-2 as that seemed to improve the situation over the METC-1 sample. This cell was run only in the liquid-fed mode because in filling the cell reservoir with Na, the level came sufficiently close to the opening of the BASE tube that it was not possible to maintain an adequate temperature differential between the reservoir and the BASE to prevent condensation of Na on the anode side. A series of measurements were taken in the liquid mode however and the results gave rather high power density levels. The maximum power density at 770 C was 0.388 W/cm^2. This value is excellent for an electrode of this size and at this temperature and is comparable to the good TiN electrodes produced by Duane Schmatz at Ford on 15 mm diameter tubes. The

[1] Ionotec, Ltd., 14 Berkeley Court, Manor Park, Runcorn, Cheshire WA71TQ, England

internal resistance was also quite low and relatively constant over the entire temperature range from 590°C to 770°C.

METC-4 - This experiment was the first to use an Ionotec tube in a functioning cell. An I-tec tube 3 cm long with a 7.6 mm O.D. and a 0.5 mm wall thickness supplied with a Weber internal electrode (anode) and a sputtered TiN cathode was sealed in the usual fashion and run. The cathode current collector was wrapped with the 0.005" Mo wire securing an annealed Cu screen to the sputtered cathode. The cathode area was 6 cm^2, larger by a factor of 2 than was the case for the Ceramatec tubes in METC-1 and 2, whose overall length was 2 cm with a 1.25 cm electrode length. The electrode was deposited only after completion of the TiCuNi braze sealing operations on both ends of the BASE tube. This was intended, as with METC-3 , to prevent unwanted modification of the cathode film due to the heating attendant on the brazing operations.

The cell was filled with ~ 20 cm^3 of Na following a conventional bake out at temperatures up to 650° C. It was set up to run in the vapor mode and operated over a range of temperatures up to a reservoir temperature of 800° C. At all times the BASE tube temperature was kept at least 50 C higher than the reservoir temperature. The effect of variations in the temperature differential were also investigated at a number of points during the run. Larger differentials led, in every case, to higher output for a given reservoir temperature, thereby confirming that the cell was operating in the vapor-fed mode. The power density is plotted as a function of reservoir temperature in Fig 5. The deduced effective internal cell resistance is shown as a function of temperature in Figure 6.

Figure 5 also shows the liquid state data from METC-3. While the METC-3 data appears to exhibit higher power density, this may be an artifact of the temperature measurement differences between the two experiments. The temperature recorded in METC-3 was that of the reservoir and because these cells are heated from the outside radially the reservoir temperature, as measured, was probably below the BASE tube temperature. The difference is not easily determined from the measurements made. A preliminary calculation of the resistance of the various components of the electrical circuit in the METC-4 cell indicate an expected internal resistance, at an operating temperature of 800° C, of approximately 35 mohms. This is substantially less than that seen in any of the operating conditions measured during the METC-4 runs as can be seen from the data as shown in Fig. 6. The details of the measured/calculated resistance for the many components of the electrical circuit within the cell are currently under investigation.

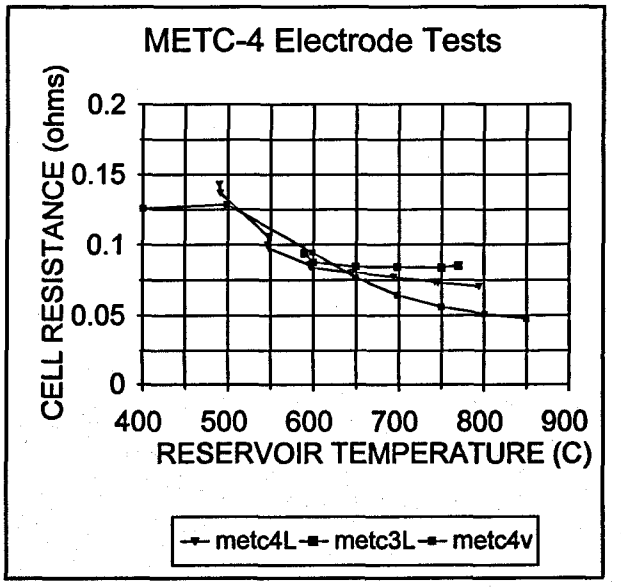

Figure 6 Internal Cell Resistance

Conclusions This cell produces power at approximately the same level in either the liquid-fed or vapor-fed operating mode. The internal resistance is somewhat higher in the vapor anode mode as should be expected from the presence of the sodium in parallel with the internal current collector in the liquid anode mode. The power density for this cell is comparable to the METC-3 liquid fed performance as can be seen in Fig. 5. It appears that the internal current collector system used in this cell is adequate to avoid significant losses due to resistance in the lead connections to the anode. It appears further that the modified assembly procedures used in METC-4 do correct the low power levels observed previously in all of the MMV cells and in the PX-1 series of cells.

The data taken here will be inserted into the full cell analysis and performance predictions made for the PX-2 series design.

METC-5 - This test incorporated a sputtered TiN cathode applied following the several brazing operations connecting the BASE tube to the tube support plate. The anode was deposited according to the same procedure that was used in the case of METC-4, using the Weber chemical deposition technique. Additional experiments were conducted to examine the effect of temperature differential between reservoir (evaporator) and BASE tube. Otherwise the test was designed to check the reproducibility of the process. The current voltage curves are shown in the X-Y plot attached in the appendix to this report. The power density is shown in Figure 7 as a function of temperature. The squares indicate the METC-5 output in the vapor-anode mode. The triangles indicate the liquid-anode performance and the circles are the values from METC-4 for comparison. The internal cell resistance is shown in Figure 6. The unusual behavior of the resistance in the liquid anode situation is suggestive of an onset of wetting phenomenon, but the details are not understood at present. The resistive values are consistent with the power performance seen in Figure 7.

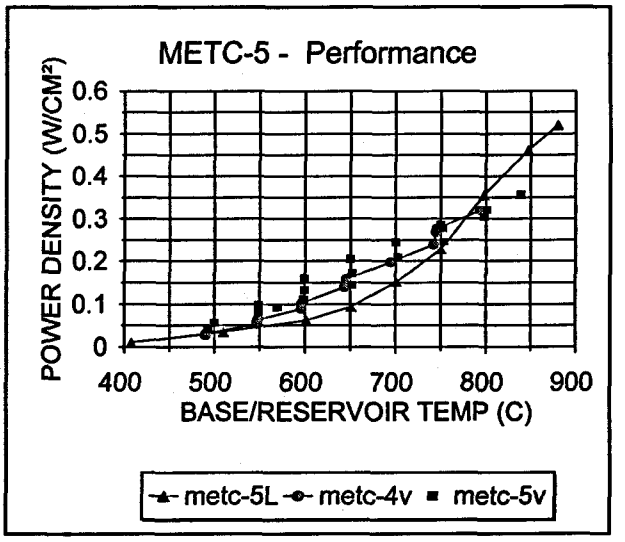

Figure 7 METC-5 Power Density

Conclusions This test verified that the high performance observed in the vapor-anode operation of METC-4 can be reproduced with considerable accuracy. Taken with similar results obtained on each of the tubes in MMV-5, it appears that the production of consistent, high power electrodes is achievable with our current practices and procedures. The former practice of carrying out the BASE-metal sealing operation following the deposition of the sputtered TiN electrode appears to have caused the degradation in electrode performance. While it is not yet known whether this was due to surface oxidation or physical morphology changes during the brazing operation, the change in procedure appears to have rectified the situation.

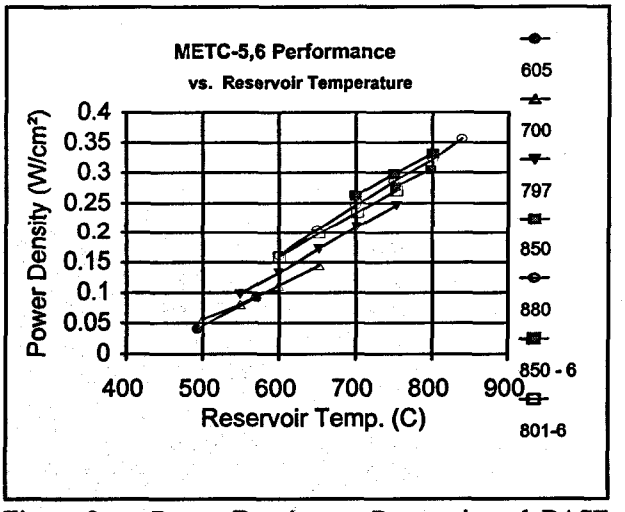

Figure 8 Power Density vs. Reservoir and BASE Temperatures for METC- 5 and METC-6.

METC-6 - This test examined the effect of substituting a molybdenum screen for the copper used as the outer current collector in all of the METC tests to date. A 11.8 x 11.8 to the cm mesh screen woven from 0.01 cm diameter molybdenum wire was tied on to the sputtered TiN cathode with Mo

wire using the same procedures as are conventionally used with the Cu screen in the previous 5 METC tests. The bus wire strapped to the screen for subsequent connection to the feedthrough lead was made of stranded Mo wire. The available Mo screen is much less conductor dense than the Cu screen used in previous tests. The resistance of the Mo screen was measured as were the complete set of accessible resistance values within the cell. The cell was baked out, filled with ~20 cm^3 of Na and outgassed in place on the sodium fill station. A series of I-V curves were taken in the usual manner at a matrix of values for both BASE tube and Na reservoir temperatures. The results for the power density are summarized in Figure 8 in which they can be compared easily with the data from METC-5. It can be seen that the Mo CC is at or above the power output of the Cu CC for all combinations of the reservoir and BASE tube temperatures. Within the expected limits of sample to sample variability, the power densities appear to be equivalent. Because the resistance of the Mo screen is substantially higher than the Cu it replaced for this test, this result was unanticipated. The imputed resistance of METC-5 is shown in Figure 9. The possibility of enhanced performance due to the presence of sodium molybdate, Na_2MoO_4, potentially formed on the surfaces of the screen during sodium flow was investigated. The cell was maintained at a BASE temperature of 850°C for over 100 hours and the I-V curve taken again. The power was slightly higher than that taken during the original testing at ~ 3 hours. The vapor pressure of the molybdate is sufficiently high that no layer of it should have remained for this period at this temperature.

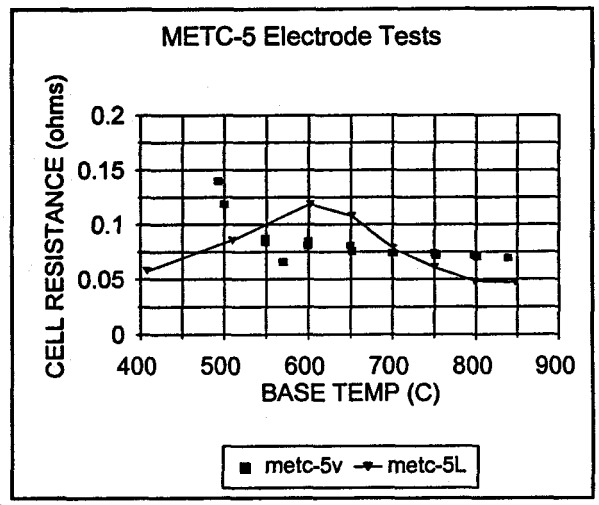

Figure 9 Internal Cell Resistance for METC-5.

Conclusions The long term durability of AMTEC cells using Cu screen for the cathode current collector is questionable due to the significant vapor pressure of Cu at cell operating temperatures. The use of molybdenum for the current collector and its components was therefore tested. Mo has a negligible vapor pressure at any practical AMTEC operating temperature. Mo also has a very low solubility in Na and is unlikely to be attacked under AMTEC conditions. Mo is denser than Cu and stiffer with lower electrical conductivity. The METC-6 test examined the effect of these properties on cell performance. It appears that use of Mo will not result in a significant performance loss, and may provide some enhancement.

MMV-5 - This experiment, involving 2 BASE tubes prepared in the same manner as those of METC's 4 and 5, yielded results consistent with those of the METC tests, as corrected for the pressure drop associated with the radiation shielding effects due to the hotter condenser and concentrated tube output. The cell was fitted with two positive feedthroughs to allow for monitoring the performance of the two

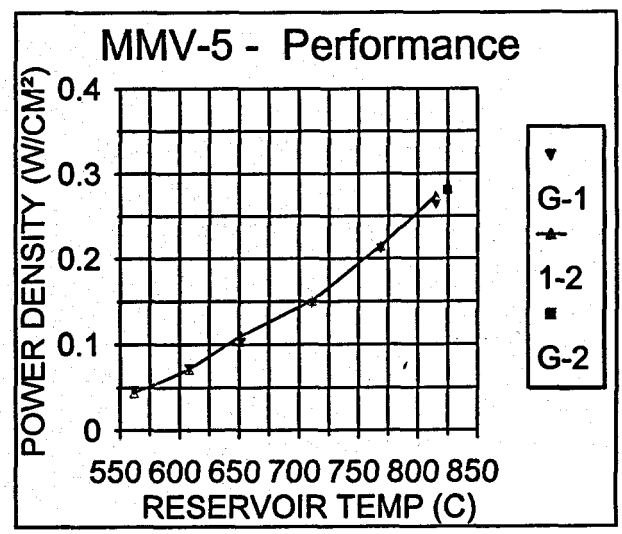

Figure 10 Peak Power Output of the 2 BASE Tubes in MMV-5.

tubes separately as well as in series. Figure 10 shows the peak power of the two tubes, labeled as ground to 1, 1 to 2 and ground to 2, based on the feedthrough numbering scheme. The two tubes had remarkably consistent performance and their summed output accurately reflected their separate contributions. The ground isolation from stray ionic currents appears to be adequate.

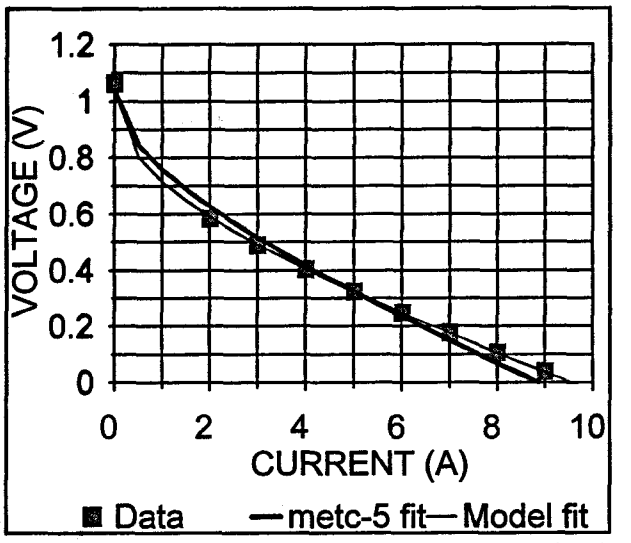

Figure 11 MMV-5 Current Voltage Data Compared with Projection Based on METC-5 Data.

In order to compare these results with those of the METC series, the TK Solver model for the MMV-5 cell was invoked using the performance parameters found in the METC-4 and METC-5 cells experiments. In Figure 11, the current voltage data from the MMV-5 experimental runs is shown plotted together with 1) a curve fitted directly to the data and 2) a projection using the TK model based on the electrode and current collector properties determined in the METC-5 experiments. The agreement, while not perfect is rather good and the projection and data diverge primarily due to the slightly higher resistance predicted from the METC data.

METC-7 - This test was intended to examine the performance of a cell that uses a Weber type cathode in addition to the now customary Weber anode. The cathode was produced by spray painting the outer surface of the BASE tube with a light coating of TiH_2 prior to processing the tube in the standard manner in the hydrogen furnace. The cell was assembled with the conventional copper inner and outer current collectors for simplicity. The maximum power points observed are shown as a function of reservoir temperature in Figure 12. The power density level was substantially lower than is usually observed for sputtered TiN electrodes as measured in earlier METC tests. Additional tests to examine ways to optimize Weber cathodes will be carried out in the future.

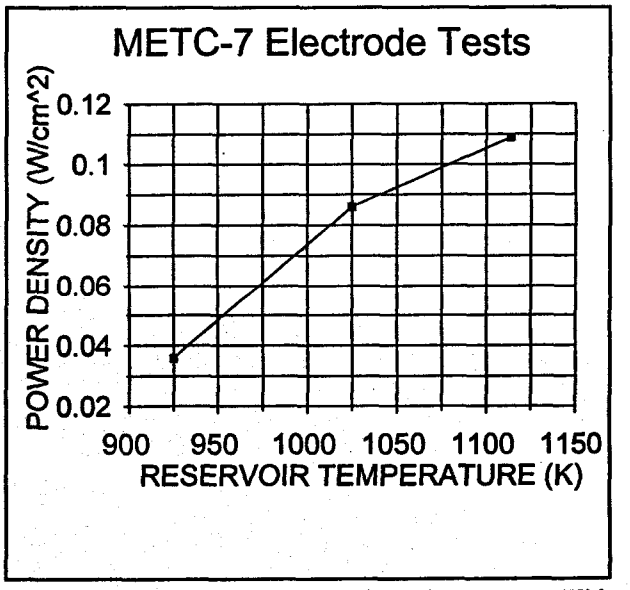

Figure 12 Peak Power for METC-7, First Attempt With Weber Cathode.

METC-8 This cell was the second METC used to test the performance of a molybdenum outer current collector. As before, the intent was to replace the usual Cu OCC with Mo in order to avoid changes in cell performance over time due to evaporation and or diffusion of the Cu. A Mo screen made by Unique Wire Weaving, was used in lieu of the copper. The screen mesh was 30 x 30 to the inch and was woven of 0.004" Mo wire. The inner current collector and its splined brace were still made in the usual manner with Cu screen, Ta cage and Ta struts. The Cu screen was attached to the Ta end plate and pin with a separate 'wad' of the same Cu screen. The performance of the combined system fell slightly below that of the best previous cell, METC-6, but above or equivalent to other all-Cu collected cells. The Mo screen has an in-plane resistance approximately 5 times that of the Cu

screen it replaced, being both sparser and of finer wire. The connecting pin from the anode to the outside was Cu as usual as was the connection from that pin to the tube support plate. The positive feedthrough also remained Cu for this test. No special effort was made to clean the Mo screen prior to installation in the OCC.

Conclusion This test confirms that use of a Mo screen for the OCC does not significantly handicap the performance of these cells. The resistance of this cell element is clearly not the limiting factor in cell output. One of the vulnerable links in the cell has thus been resolved.

METC-9 This cell had a molybdenum outer current collector screen that was wrapped to the BASE tube with a Mo wire and a stranded Mo bus wire was attached in the usual way, underneath the Mo wire wrap. This is now standard procedure. This time the inner current collector was also made using a piece of the same Mo screen together with a standard Ta splined cage. No adjustment was made in the size of the cage to accommodate the thinner Mo screen. A tight fit was achieved nevertheless. The Mo screen was not cleaned in any way prior to installation inside the tube. The performance of this cell, shown in Figure 13, was decidedly weaker than for those cells using the Cu internal current collector. The short circuit current was lower and the internal cell resistance as determined from fitting the I-V data in the simple, conventional way was much higher than the typical Cu ICC cell. The cell was also run in the liquid-vapor mode to identify the source of the additional resistance. The resulting power density data is also shown in Fig. 13.

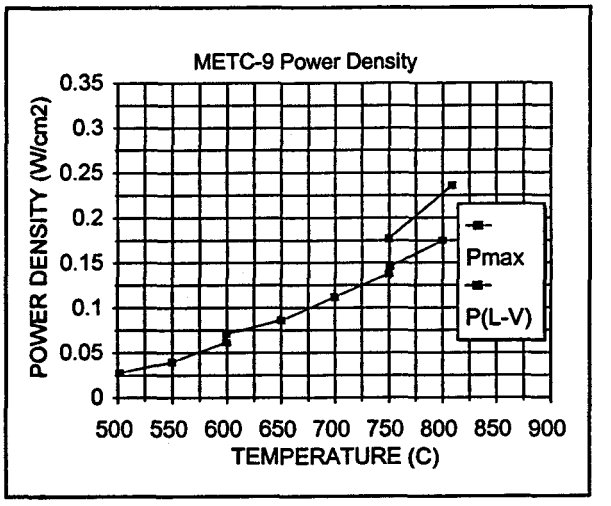

Figure 13 Power Density for Vapor-Vapor and Liquid-Vapor Operation Showing Effect of Reduced ICC Resistance.

Conclusion The Mo ICC screen must be more carefully managed to reduce its resistance contribution. Special cleaning and surface treatments will be tried to reduce the contact resistance between the anode and ICC.

METC-10 This cell had a number of changes incorporated. Both internal and external molybdenum current collectors were used in place of the copper used in most previous AMTEC cells in the vapor-vapor operational mode series. The Mo screens were washed ultrasonically in "MicroWash" a strong detergent. They emerge from this cleaning with a bright finish. In addition, the Cu anode connection pin was replaced with a nickel tube into which the interconnect wire was pinched. Further the braze filler material used to join both end fixtures, plate and thimble, was TiNi rather than the previously used TiCuNi. Evidence showing that the Cu leaves the TiCuNi joints probably rendering them

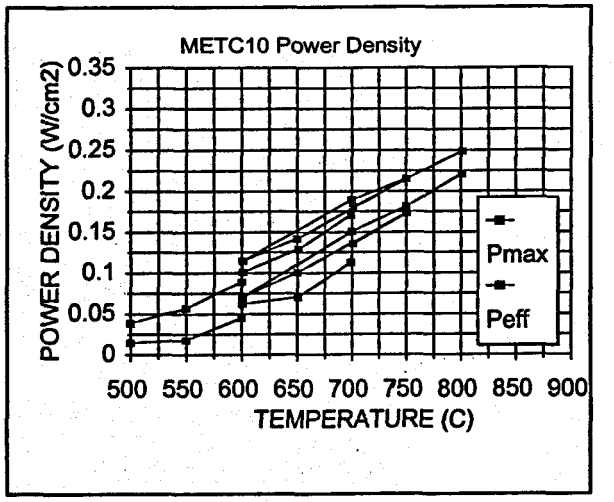

Figure 14 Power Density Curves for Mo/Mo Current Collector Tube Showing P_{max} and P_{eff} Data as a Function of Reservoir Temperature.

porous contributed to this choice. It can be seen in Figure 14 that the maximum power levels are lower than for the all copper current collectors and lower than the METC-8 cell with its copper inner collector screen and Mo outer screen, Mo bus wire and Mo wrap. They are however significantly better than those of METC-9 the screen for which appears to have been inadequately cleaned. The lower set of curves shows the power density produced by this tube, for each temperature, at a standard 0.6 volt output. This is the approximate voltage required of each of the 6 tubes in a PX series cell as contemplated for the ARPS program and is close to the peak efficiency point for tubes as assembled into a 6-tube cell. It can be seen that at the higher temperatures, the drop off from peak power is only about 20% at a power level which is actually quite close to maximum efficiency. The various points shown for each of the two power criteria at a temperature reflect the variation due to different BASE tube temperatures.

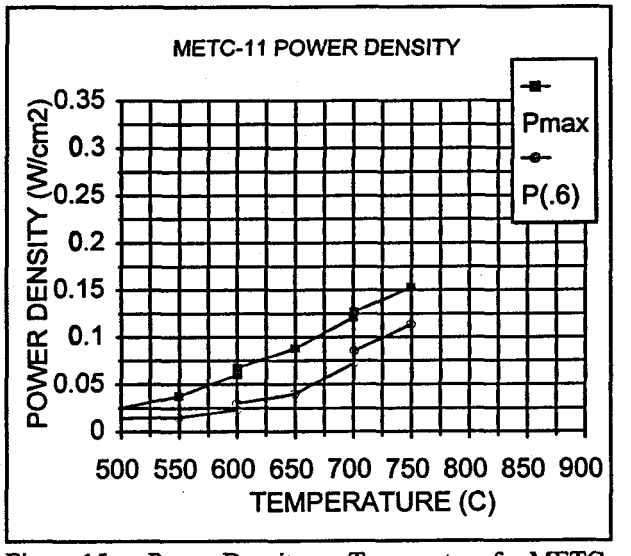

Figure 15 Power Density vs. Temperature for METC-11, Hydrogen Baked ICC and OCC screens.

Conclusion The higher resistance of the Mo inner current collector leads to a reduction in the peak power capability. The power levels, nevertheless, are nearly adequate to provide the required output for the ARPS program. We will continue fine tuning the inner current collector design to reduce the impedance. Use of Mo screen with a more dense weave is expected to be useful in this regard. A combination of finer weave and finer wire should be tried. Unique Wire Weaving makes such material.

METC-11 This cell was built to examine the effect of a different treatment of the ICC Mo screen. The Mo screen for this cell was baked in the hydrogen furnace at 1034 C prior to insertion in the tube. The rest of the assembly procedure was similar to that for METC-10. The power/temperature performance is shown in Figure 15. It can be seen that the results appear to be inferior to those of METC-10 for which the detergent cleaning approach was used.

Conclusion The more complex approach to cleaning the Mo screen using the H_2 furnace is not necessary and may be less effective than the detergent/U.S. approach. Additional approaches to reducing the contact resistance will be tried and denser screen will also be tested.

METC-12 This cell was similar to #11 with the exception that the 30x30/inch Mo screen used for the internal current collector was coated with a sputtered TiN film. The sputtering run was carried out during a deposition of cathodes for another cell. As with #11, the Mo screen was baked out to clean it in the hydrogen furnace at 1034 C. The power vs. reservoir temperature data are plotted in Figure 16. The lower curve is that for the power at a cell voltage of 0.6 volts. It will be seen that the peak power for both

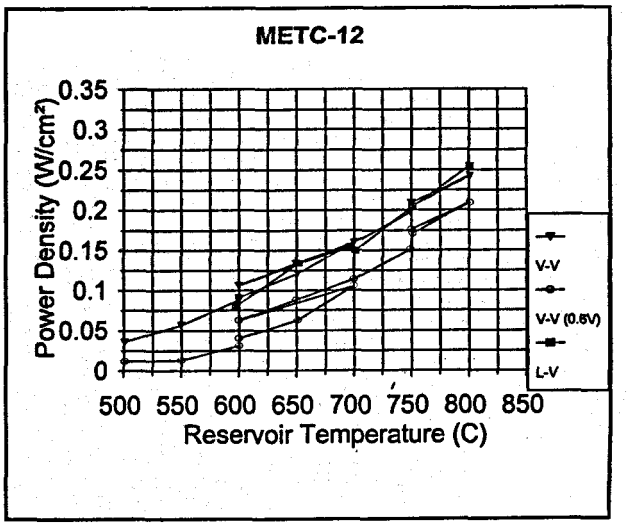

Figure 16 Power Density vs. Temperature for METC-12 showing both Peak Power and Power at 0.6 volts/tube,

vapor-vapor and liquid-vapor operating modes are essentially identical over the full test range. This is the case in spite of the fact that the internal cell resistance is substantially lower in the L-V case. It appears that the vapor anode case has a higher open circuit voltage and thus, in spite of its higher resistance, it gives the same peak power at the current for which that occurs in each case. The overall cell resistance in the liquid anode state increases slightly with temperature as shown in Figure 17. If we assume that the resistance contribution from the anode side is small with the liquid sodium present, the increase with temperature may be attributed to the increase with temperature of the cathode side metallic elements since the BASE resistivity falls slightly over this temperature range. Knowing that the metallic materials are primarily Mo, we should be able to deduce the total external Mo resistance.

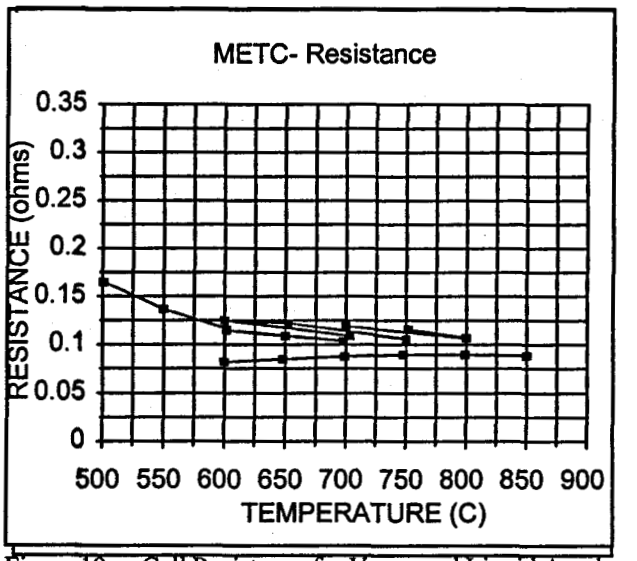

Figure 17 Internal Cell Resistance for METC-12 for both Vapor and Liquid Anode States.

Figure 19 Cell Resistance for Vapor and Liquid Anode Runs on METC-13

METC-13 This cell was assembled with a Weber anode and sputtered TiN cathode as usual. The top 'plate' on the BASE tube was thicker Ta, 0.010" vs usual 0.005". The internal current collector used 60x60 to the inch Mo screen knit from).004" Mo wire. The screen was cleaned ultrasonically in micro-wash solution. The OCC wrap was of Mo wire with a stranded Mo wire bus as has now become standard. The intention was to examine the effect of the higher density Mo ICC screen on the power density and I-V curves as a function of temperature.

As can be seen clearly in Figure 18, the values of the power densities for liquid and vapor anode cases are very close. Note also that in this test, the BASE heater temperature was raised until the BASE temperature reached 930 °C. At this temperature the voltage dropped rapidly to zero indicating that the BASE-Ta braze had let go. This temperature is, within probable error limits, the same as the 942°C upper limit for the TiNi braze filler material.

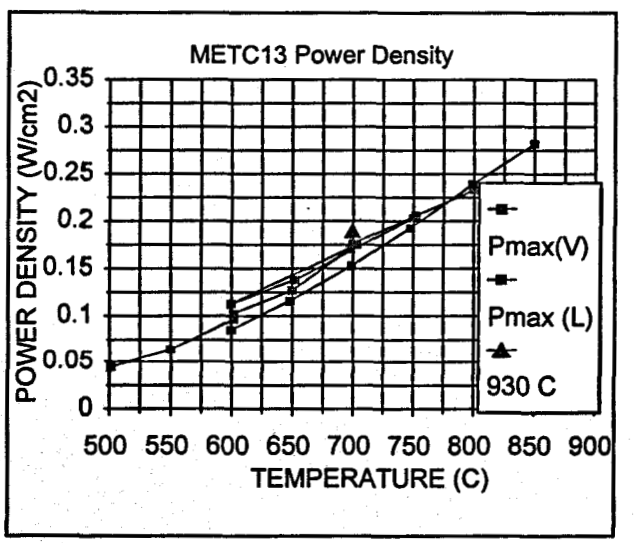

Figure 18 Power Density for METC-13. Data Point at Highest T_{beta} Before Braze Failure.

Figure 19 shows the resistance, measured from the extended section of the I-V curves, for #13 in the liquid and vapor anode runs. The difference between the two curves at the upper temperatures is ~ 15 mΩ - 25 mΩ. This is a lower differential than was seen in any of the previous METC cells.

Conclusions While the peak power for 13 is not as high as for #6, the denser ICC screen and revised internal connection of screen to crimp pin appears to have reduced the internal cell resistance differential between liquid and vapor anode runs.

Figure 20 shows two I-V curves taken at essentially the same reservoir temperature but different BASE temperatures. While both have nearly the same peak power, the high BASE temperature curve has a higher resistance and thus a lower short circuit current. This may be due to the higher resistance of the internal cell metallic circuit elements rising with increasing temperature. The BASE resistivity should drop slightly over this temperature range. The BASE resistivity is not, therefore a major factor in the cell resistance seen here.

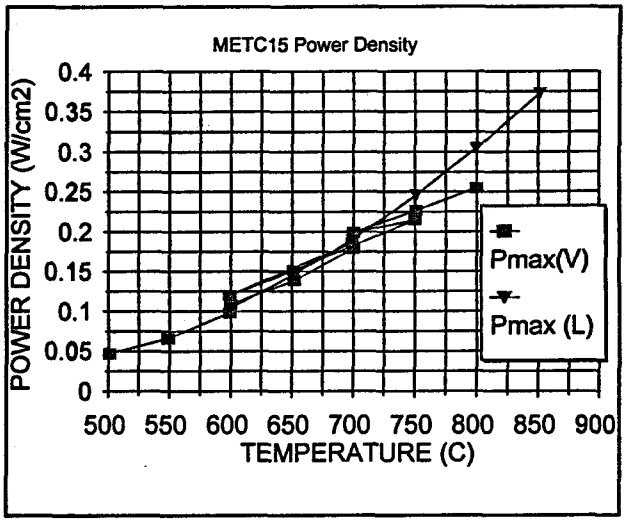

Figure 21 Power Density Data for METC-15 in both Liquid and Vapor Anode States.

Conclusions While the peak power for METC-13 is not as high as for #6, the denser ICC screen and revised internal connection of screen to crimp pin appears to have reduced the internal cell resistance differential between liquid and vapor anode runs.

METC-14 This cell was assembled with 60x60/inch molybdenum mesh with 0.004" Mo wire, for both inner and outer current collectors. This was the first cell to use this mesh screen for both ICC and OCC. Unfortunately, serious fill station problems prevented proper filling of the cell and it could not be run successfully. Cell # 15 was made in a similar way and was then run successfully. No significant conclusions could be drawn from the experience with #14.

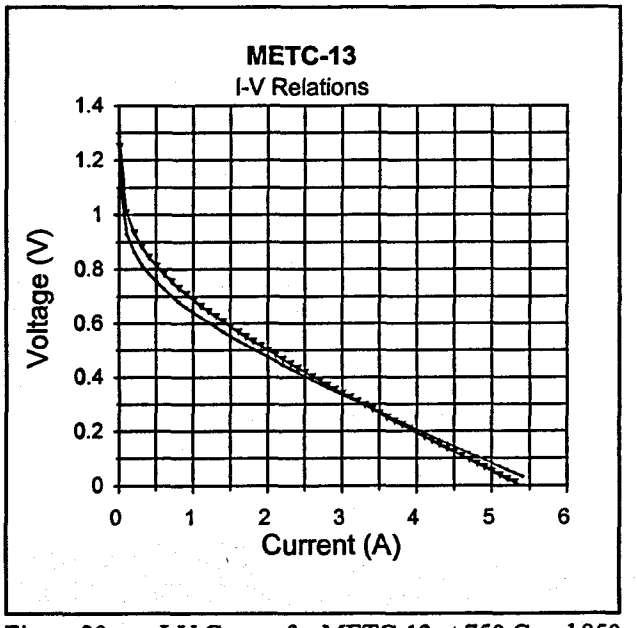

Figure 20 I-V Curves for METC-13 at 750 C and 850 C BASE Temperature, 700 C Reservoir Temperature

METC-15 This cell was constructed using the 24x24/cm Mo mesh with 0.010 cm diameter wire. The power vs. reservoir temperature data are shown in Figure 21. The power for this cell is somewhat improved over that for the previous all-Mo current collector cells but does not reach the levels achieved in METC-6 and METC-5 which had Cu inner current collectors. It appears that the difference in output power is mostly related to internal cell resistance level which, for this cell, remains higher than was the case for the earlier Cu collected cells. The cell resistance is shown in Figure 22.

METC-16 This cell was built to investigate the effect of using a high thermal expansion cage to press the inner current collector screen against the anode. A cage formed of Ni wire was built on the standard mandrel and used with the usual 24x24/cm Mo wire mesh. It was expected that this approach might produce a higher pressure contact through the initial warm up period to operating temperature, but that it probably would anneal at the operating temperature and on subsequent cooling and reheating would have a poorer response. Note that Ni has a higher resistivity than Mo and hence might not give as low an internal impedance overall. The results for METC-16 are summarized in Table 1. The total power was not particularly good and the

internal resistance was relatively high. The cell was run through the usual battery of I-V curves as a function of both BASE tube and reservoir temperatures. It was then cooled down, reheated and run again to allow identification of any electrical changes which might have been induced by the thermal cycling. The results following the thermal cycling runs were, within the limits of normal variability, identical to those measured on the first heating. Either, the cage annealed and did not apply strong pressure, even in the first warm up, or this contact was not the rate limiting stage of the AMTEC process in this cell.

Conclusions It appears that any additional pressure that can be easily applied to the inner current collector, to enhance its contact with the Weber process anode using a relatively soft metal such as Ni, is unlikely to be helpful. While thermal cycling did not appear to worsen the contact to the anode, the Ni approach can not be said to have helped either. Other approaches to reducing contact resistance are likely to be better candidates.

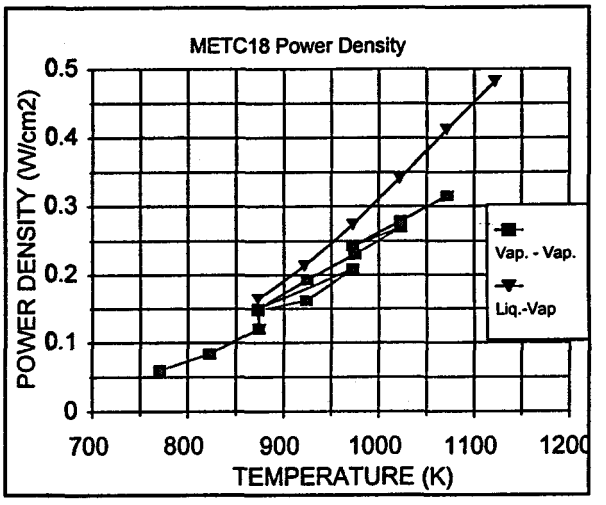

Figure 23 Power Density for METC-18.

METC-17 This cell was built with the standard 24x24/cm Mo mesh ICC and OCC. The distinction here is that the ICC Mo mesh was coated with a layer of TiN deposited by the Weber process. The intention was to attempt a reduction of interfacial impedance at the interface between the Mo mesh and the TiN anode coating. An earlier run, METC-12, attempted this trial using a sputter coated Mo mesh layer. That was not particularly successful as can be seen from its data in Table 1. However the Weber coating is much more robust and, with a rougher surface, may have a better chance to make low resistance contacts to the anode layer. The test run on this BASE tube assembly has been postponed in deference to more critical tests.

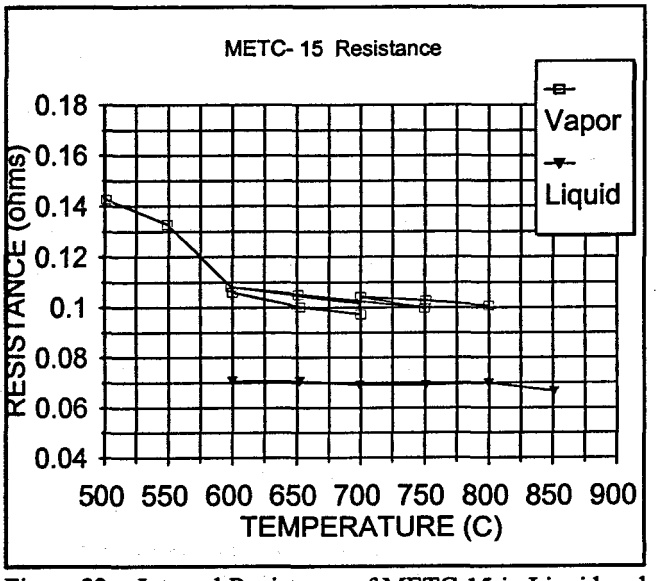

Figure 22 Internal Resistance of METC-15 in Liquid and Vapor Anode States.

METC-18 This cell uses all Mo current collector systems and has its anode produced by the lower temperature Weber process. This modified process produces a much more adherent TiN coating and the major point of interest in this experiment was to determine if that coating had adequate permeability for high power operation. The internal cage was made in the standard way and the internal Mo screen was the 24x24/cm using 0.010 cm Mo wire. Because the coating appears to be more dense and harder, it was believed useful to run a performance test to verify that these properties do not adversely affect the sodium permeability of anode prepared in this way. The power performance of this electrode as shown in Figure 23, is nearly as good as any seen previously with the exception of METC-5 and METC-6 which had only a slight edge.

Conclusions The peak power for these cells appears to be very closely correlated with the measured internal resistance of the cells. This cell, with an all Mo current collection network had a power output density extremely close to the best ever observed in large surface area electrodes. We conclude, that even without further enhancement, the electrode output is adequate for the space power missions.

METC-20 This cell test was intended to qualify the 'advanced beta" tube assembly for use in future members of the PX cell series. More specifically, this tube design uses a shorter alpha alumina ring for isolation with respect to ionic leakage currents between the cathode and the grounded metal braze joint at the base of the tube. It was deemed useful to verify that the change in dimensions of the alpha ring did not bring unintended consequences with it. The tests run on METC-20showed no problems with the BASE tube braze joints. The electrode and current collectors for this cell were identical with those of METC-18 with the exception of the wire gauge for the OCC. It was a 24x24/cm mesh as before, but the wire diameter was 0.016 cm instead of the 0.010 cm as has been the case in all such meshes used before. Power performance and internal cell resistance are plotted in Figures 24 and 25 respectively. The liquid-vapor mode power data were taken over a somewhat wider range of temperature and reached to virtually as high power as any cell tested here.

Conclusions The mechanical strength of the modified alpha ring and seal were verified as being adequate to deal with the stresses of the assembly and operation. The electrical properties were not expected to be affected by these changes, as measured in an METC type test. The performance was very close to that of the #18 cell, which was electrically similar in design and fabrication.

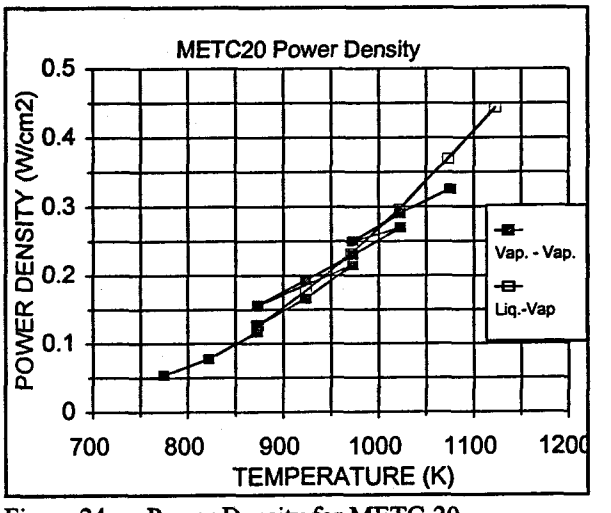

Figure 24 Power Density for METC-20.

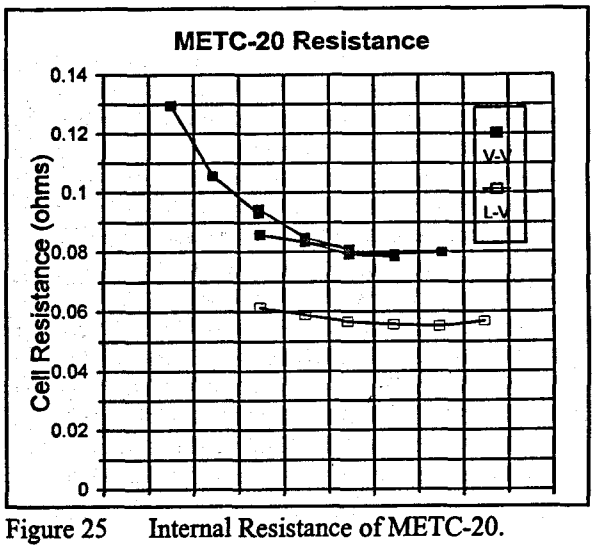

Figure 25 Internal Resistance of METC-20.

Table 1 METC Characteristics and Parameters

Cell	Inner CC	Outer CC	$P_{max}(T)_V$ (W/cm^2)	R_o $(ohms)_{vap}$ or	$P_{max}(T)_L$ (W/cm^2)	Summary Comments
METC-1	Cu screen	Cu screen	NA		0.09(1046)	Sputter First
METC-2	Cu screen	Cu screen	0.11(923)		0.24(1023)	"
METC-3	Cu screen	Cu screen	NA		0.39(1043)	Braze First
METC-4	Cu screen	Cu screen	0.32(1073)		0.45(1123)	"
METC-5	Cu screen	Cu screen	0.36(1113)	0.075 Ω	0.52(1153)	-
METC-6	Cu screen	Mo (12x12/cm)	0.356(1112)			Ta inner bus
METC-7	Cu screen	Cu screen	0.109(1114)	0.15 Ω	NA	Weber cathode
METC-8	Cu screen	Mo (12x12/cm)				Ta inner bus
METC-9	Mo (12x12/cm)	Mo (12x12/cm)	0.175(1073)	0.125 Ω	0.236(1082)	
METC-10	Mo (12x12/cm)	Mo (12x12/cm)	0.249(1074)	0.11 Ω		Ni pin, μ-wash
METC-11	Mo (12x12/cm)	Mo (12x12/cm)	0.153(1023)	0.112 Ω		H_2 baked Mo screen
METC-12	Mo (TiN coated)	Mo(24x24/cm)	0.243(1074)	0.100 Ω	0.255(1074)	Sputter coated ICC
METC-13	Mo(24x24 cm)	Mo(24x24/cm)	0.233(1073)	0.130 Ω	0.28(1123)	Std. ICC bus
METC-14	Mo(24x24 cm)	Mo(24x24 cm)	NA	NA	NA	Modified ICC bus
METC-15	Mo(24x24 cm)	Mo(24x24 cm)	0.255(1073)	0.100 Ω	0.373(1124)	Modified ICC bus
METC-16	Mo(24x24 cm)	Mo(24x24 cm)	0.223(1074)	0.117 Ω	0.310(1122)	Ni cage
METC-17	Mo(24x24 cm)	Mo(24x24 cm)				Weber coated Mo
METC-18	Mo(24x24 cm)	Mo(24x24 cm)	0.315(1073)	0.083	0.482(1122)	L.T. Weber anode
METC-19						
METC-20	Mo(24x24 cm)	Mo(24x24 cm)	0.326(1073)	0.080	0.444(1123)	Adv. Beta; 0.016 cm diam Mo
METC-21						
METC-22	Mo(24x24 cm)	Mo(24x24 cm)	0.129(1071)	0.069	0.198(1118)	Commercial TiN

Power vs. Internal Resistance - General Conclusions

Figure 26 is a plot, for most of the METC series cells, of the peak power at 800 C as a function of the measured internal impedance. For this case the internal impedance is obtained from a fit to the data of the expression

$$V = A - RT_2 / F \ln(i) - iR_o$$

where R_o is the internal resistance of the cell including all components, and A is the second fitted parameter for which no simple physical interpretation is presently available. The vertical line at ~14 milliohms

indicates the resistance of the beta"-alumina at the operating temperature. It can be seen that the peak power is nearly linearly related to the impedance. The open squares are points plotted for operation in the liquid anode mode while the solid points are for vapor-vapor operation. Noting that the liquid anode points fall on the same line as the vapor anode data suggests that the primary effect of the liquid sodium on the anode side is to reduce that impedance and not to change the exchange current in an important way. It is likely that the exchange current at the anode/BASE interface is not involved in the rate limiting step for these cells. To further reduce the cell impedance and increase the power output, the cathode is the place to attack.

METC-22 This cell uses the standard Weber anode but uses a TiN cathode sputtered by a commercial company, TI Coatings, Inc. The coating was deposited during the course of TI Coatings' standard processing operation. A sample coating was examined at 100X with a metallurgical microscope under dark field illumination. The Weber coating appeared to be approximately 30 -40 microns thick while at this magnification, the sputtered coating appears to be less than about 5 microns thick. A more accurate determination will require an SEM examination. the simple, point to point resistance measurement routinely taken on cathode films was made and the measurement gave ~ 1.5 ohms as compared to ~ 30 ohms for the standard AMPS/sputtered electrode films. With a cathode thus 3 to 5 times thicker than the AMPS sputtered electrodes, it should be expected that lower power will be seen due, in part, to the lower permeability of the thicker cathode. In previous tests it appeared that the cathode and OCC resistance was not a large contributor to the overall internal impedance of the METC cells. In addition it should be noted that following the sputtering operation at TI, the tube had a much larger vacuum leak rate than it had initially. The balance ring at the closed end of the tube had been cracked and lost during the process, whether by damage in sputtering or by handling is not known. Further, it may be expected that some additional air (possibly humid) exposure may have occurred during handling at TI.

The I-V curves were taken in the usual sequence. The apparent internal resistance in the vapor anode mode is substantially higher when determined in the simple manner used here. The liquid anode mode was then used to investigate the effect it leads to with respect to the anode and its current collector system. The peak power in the vapor anode case is at about 1/3 - ½ of that seen in the best electrode tests (such as METC-20). Such a result was anticipated even in the event that the TiN film morphology was proper for transmitting sodium since it is much thicker than the standard cathode films. The sequence of I-V runs in the liquid anode case, initially showed a very low open circuit voltage. The shape of the curves (curved, but very little upturn at low current) is consistent with an internal short circuit that resolved itself at the higher temperatures (or longer times). The curve taken at 845 C showed an essentially normal I-V curve and an internal impedance of ~0.069 Ω and a peak power of 0.198 watts/cm^2. This data point is plotted as the triangle in Figure 26. Whereas the liquid and vapor anode cases with the standard TiN sputtered coating appear quite consistently related to the internal impedance, this one is substantially lower. This confirms the consistency with the effect expected from a thick cathode having a large G factor.

METC-40

This cell was designed and the experiments carried out to test a new cell design known as the Internal Self-Heat Piping that had been invented under AMPS internal research and development funding. In this approach, the BASE tube is arranged so that the condensation of sodium within the BASE tube does not cause short circuit conditions but retains the isothermalization property needed to reduce or eliminate temperature gradients in and along the BASE tube. This cell is constructed quite differently in order to simulate the thermal gradients and stresses that occur in a typical PX series cell. The basic cell and tube configuration is shown in Figure 26. The BASE tube is heated from the bottom only in order to allow examination of the effects of a temperature gradient down the tube such as is generally the case for conventional PX series cells. Note that the BASE tube is supported open end up and the sodium reservoir is at the 'top' with a standpipe to prevent sodium from dripping down and filling the BASE tube. A shield

is in place to prevent any possible dripping from the upper region to impinging directly on the hot ceramic tube. The blue thick section tube support plate is made of nickel to improve its thermal conductivity, and a local heater is wound around the outside surface of this plate so that it can be heated independently from the reservoir and or lateral tube heater.

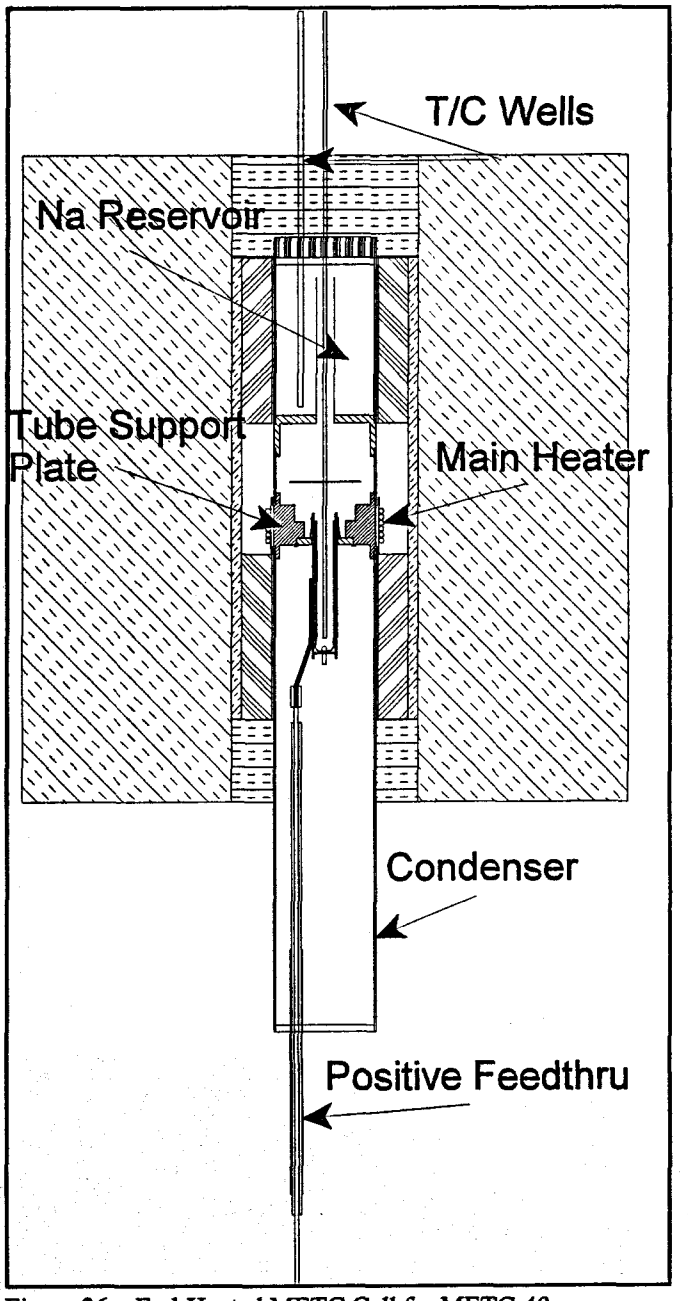

Figure 26 End-Heated METC Cell for METC-40

Results The cell was run first in the completely dry state, without sodium to set a baseline for the temperature gradients. The results of the dry test are shown in Figure 27. In this figure, the position is indicated on the X-axis. It is clear that the temperature profile through the BASE tube region is essentially linear and that this property does not change with changes in the reservoir temperature.

The cell was then loaded with sodium and run through a range of temperatures for the tube and the reservoir. Temperature profiles were measured at regular intervals and produced data shown in Figure 28. It can be seen that with the reservoir temperature above about 660 C, an isothermal region at very nearly the same temperature as the evaporator/reservoir develops in the BASE tube. The length of the region grows as the temperature increases until it encompasses the tube from end to end and a portion of the alpha insulator tube as well. Because the BASE tube is mounted open end up, there was a possible ambiguity as to whether it might have filled with Na and isothermalized using the Na thermal conduction. Another test was performed in which the tube was deliberately allowed to condense sodium to fill it by operating the reservoir hotter than the tube support plate. The temperature profile was then measured and a clear temperature gradient observed in distinct contrast to the isothermal lines shown in Figure 28. This result confirms that the heat piping approach is behaving as predicted. The current - voltage curve taken for this cell at a BASE tube temperature of 779 C is shown in Figure 29. The peak power level at 1.82 Watts corresponds to 0.307 W/cm^2. This is fairly close to the value for the best two previous electrodes #'s 18 and 20 at this temperature.

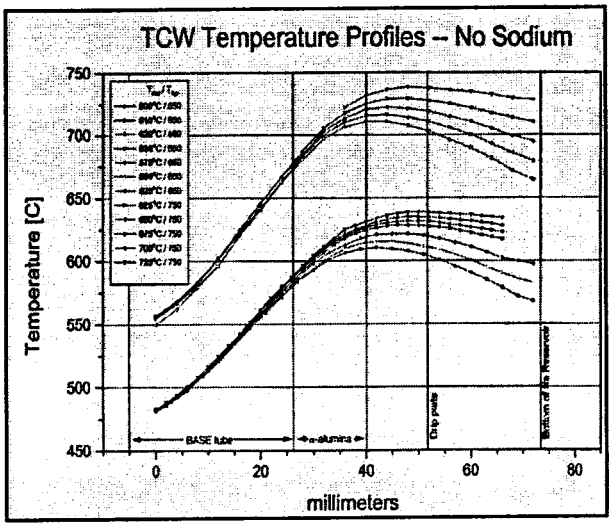

Figure 27 Temperature Profiles of METC40 Running Dry.

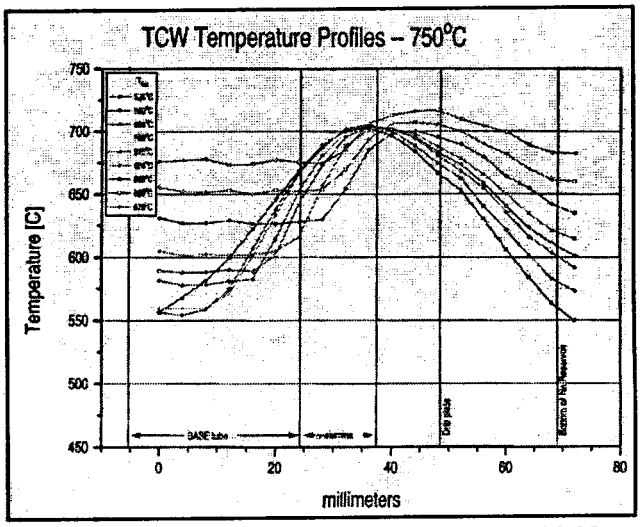

Figure 28 Temperature Profiles of METC40 With Na at 750C

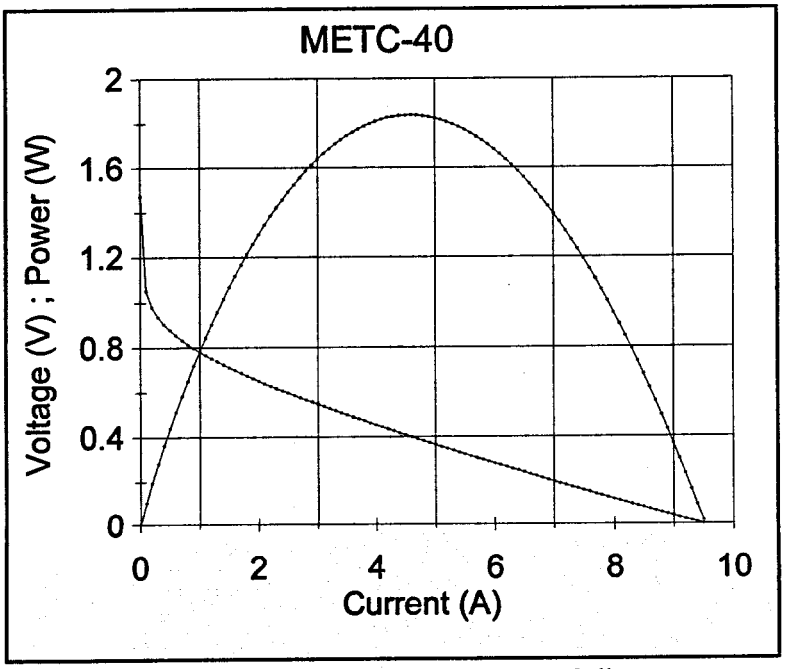

Figure 29 Current-Voltage Data at 779 C for ISHP Cell.

5. Component Development and Testing

5.1 K-BASE AMTEC Development

AMTEC cells that use potassium (K) instead of sodium may have important advantages for some specific applications and perhaps quite generally. Potassium has a significantly higher vapor pressure than sodium and for this reason, a cell using K should, all other aspects being equal and at the same temperature, have a higher voltage than a cell with sodium. If the ionic resistivity of K-BASE is not much worse than Na-BASE, a K-cell should be able to operate either with the same power at a lower hot side temperature, or at increased power at the same hot side temperature. It is also possible that all other things would not be equal and in particular that one might be able to make long term use of the enhanced molybdenum electrodes that perform, initially, so well in sodium cells. In sodium cells, the oxide on the surfaces of a moly electrode reacts, in the presence of sodium metal, to form sodium molybdate, Na_2MoO_4, and other non-stoichiometric compounds that serve to conduct both Na ions and electrons.[2] The extended interface this affords and the ready transport of Na ions through the cathode when these compounds are present at grain boundaries and on the surface of pores, has been shown to lead to nearly perfect electrode performance. Unfortunately the moly/Na/oxygen compounds evaporate readily at normal AMTEC operating temperatures of 800 C to 900 C and the excellent performance doesn't last.

It is anticipated that with potassium the high performance situation may be much longer lived. The potentially lower K-cell operating temperature should allow for longer life at a given performance level and there is reason to believe that the K/Mo/oxygen analogs will have a much lower vapor pressure than the sodium variety. Thus a K-cell with a molybdenum cathode may have both long life and high performance. The experiments described here have been chosen to investigate this possibility.

1. Exp. 1 In the first experiment with a potassium cell, we ran an METC (#76) with an Ionotec K-BASE tube and small load of K. The object was to see if performance is reasonably in accord with expectations based on K-BASE resistivity data published by R.M. Williams[3] and to verify that we could load and run a cell with this new material. To this end use a standard TiN electrode deposited in Blue Max[4]. Used a continuous Mo wire wrap for the outer current collector (OCC) without a Mo screen between the wire and the BASE. In this approach the Mo wire is wrapped tightly, with no space between turns, around the

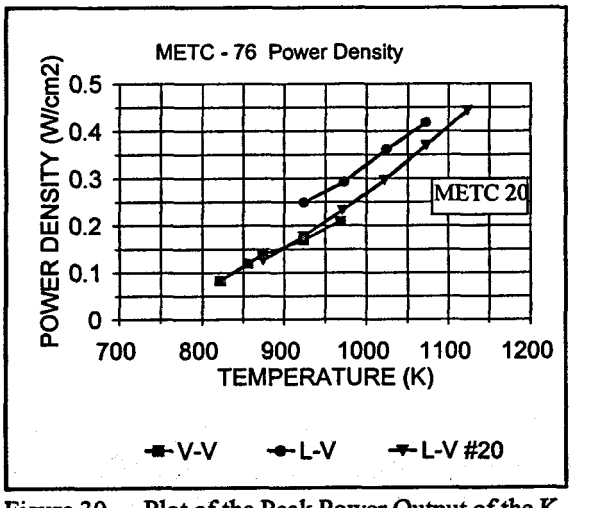

Figure 30 Plot of the Peak Power Output of the K-BASE Cell and Comparison with METC-20, the Best of the Na METC's.

---

[2] 'The Role of Oxygen in Porous Molybdenum Electrodes for the Alkali Metal Thermoelectric Converter', R.M. Williams, G. Nagasubramanian, S.K. Khanna, C.P. Bankston, A.P. Thakoor, and T. Cole, Journal of the Electrochemical Society, 133, 1587-1595, (1986).

[3] R.M. Williams, B. Jeffries-Nakamura, M.L. Underwood, M.A. Ryan, D. O'Connor and S. Kikkert, Solid State Ionics, 53-56, 806-810 (1992).

[4] A sputtering system obtained from Ford Motor Company and equipped for computer controlled reactive sputter deposition of thin films of titanium nitride.

entire length of the electrode. The power vs. temperature data for this cell are plotted in Figure 30. Shown also for comparison is curve of the data from METC 20, the best of the Na electrodes tested.

Results were very good as at 800 C in the liquid anode more, this cell produced the highest power level seen in any METC cell at that temperature. In general, the power output was that appropriate for the best Na METC cells tested thus far, but at about 50 C lower temperature. The cell resistance was low. In Figure 30 it can be seen that the liquid anode performance of the K-BASE cell is substantially higher at 800 C, than that of METC-20, which had the best Na -based METC performance we have seen. Based on the two curves shown, the K-BASE cell has the same performance at approximately 50 C lower operating temperature. This cell had a titanium nitride electrode of the usual type. The effective internal resistance of this cell was somewhat higher than that of METC-20 as shown in Figure 31. The improved performance, in spite of the higher internal resistance tends to confirm the increased vapor pressure as the major cause of the better performance. Nevertheless, the internal impedance is still very low suggesting that the ionic resistivity of the K-BASE may be nearly comparable to that of Na-BASE. Additional testing will be required to justify this conclusion.

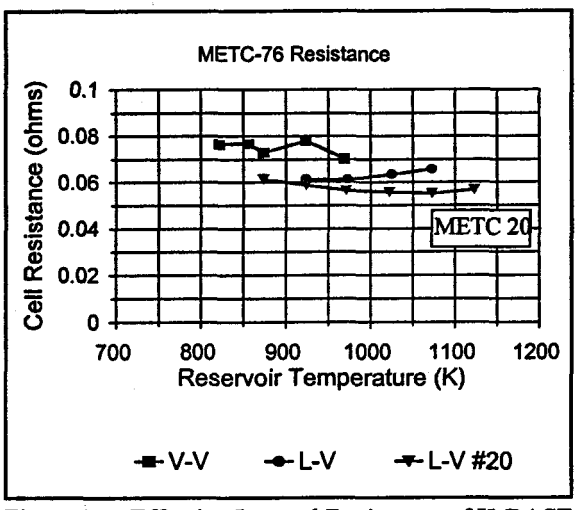

Figure 31 Effective Internal Resistance of K-BASE Cell & Comparison With High Performance METC-20.

5.2 High Temperature Wicks

For operation at high temperatures it is necessary to have an evaporator wick with rather fine pores in order that the capillary pressure can overcome the higher vapor pressure of the alkali metal at high temperatures. Wick properties as required for sodium-based cells are shown in Figure 32. For potassium based cells the pore size is shown as a function of temperature in Figure 33. On these charts we also show the effect on pore size of two specific pressure drops. These reflect the added pressure requirements due to the viscous pressure drop related to flow through an artery that is designed to feed sodium to the evaporator having the fine pores ultimately required to make up the vapor pressure difference across the BASE element. While we do not attempt to model the performance of a specific artery design here, the pressure drop selections shown are representative of the flow for a realistic range of cell currents.

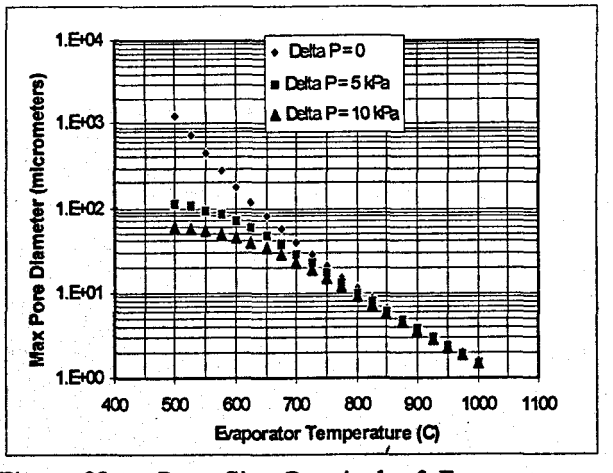

Figure 32 Pore Size Required of Evaporator vs. Temperature For Sodium.

The surface tension of potassium is significantly lower than that for sodium. Figure 33 indicates the differences in both surface free energy and viscosity for sodium and potassium. While the pore size required for operating a potassium cell is clearly smaller than for a sodium cell at the same temperature, it can be seen that this is somewhat compensated for by the lower viscosity of potassium which reduces the flow pressure drop in the artery. The relative values for these parameters can be seen from the plots in Figure 34. Nevertheless, for operation at a given high temperature,

the capillary pore size for effective flow of K in a K-BASE cell must be significantly smaller than for the sodium case.

The capillary structures for alkali metal return in AMTEC systems for transportation applications can be made of relatively inexpensive raw materials such as the stainless steels, iron or nickel and potentially of ceramic materials that can be readily wetted by liquid alkali metals. The experimental cells and systems built during this program used fine SS felt with a basic pore size of ~ 12 microns but compressed into a tight cylinder of much smaller effective pore diameter. By compressing thin disks of this felt, it has been possible to produce graded arteries such that the finest pores, which govern the ultimate pressure and hence limit the operating temperature of the cell, occur only over a limited length of the artery and thus produce a minimal pressure drop due to the returning AM flow. While this approach is expensive both in the felt source material and in the fabrication process, SS capillary structures with pore sizes at and/or below those used in current AMTEC converters are available as inexpensive commercial filters[5].

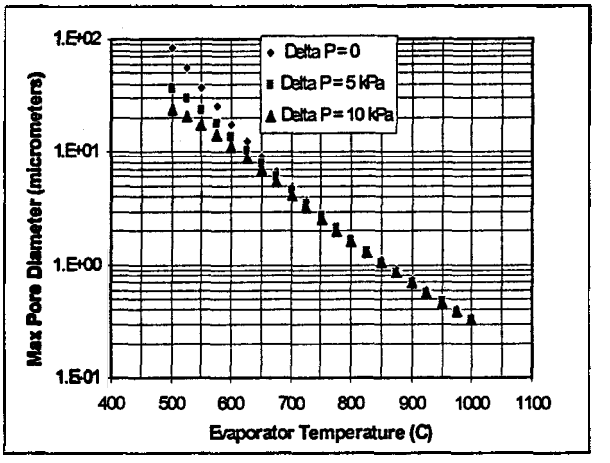

Figure 33 Pore Size Required of Evaporator vs. Temperature for Potassium.

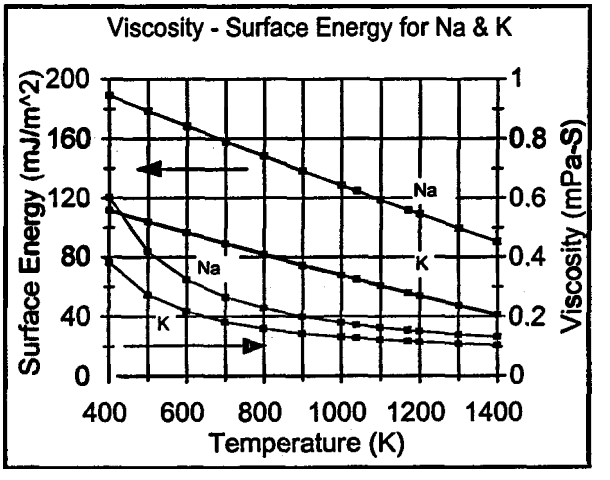

For high power systems, it may be more cost effective to avoid the wick return approach altogether in favor of an inexpensive electromagnetic pump return system. While previous programs have used EM pumps with permanent magnets, primarily for simplicity in testing, the cost of such magnets will almost certainly be prohibitive for automotive applications. The converter

[5] Purchased from Brunswick Technetics, 4116 Sorrento Valley Blvd. San Diego, CA 92121. Similar material can be obtained from Bekaert Fibre Technologies, 1395 S. Marietta Parkway Building 500, Suite 100 Marietta Georgia 30067

[6] 'A Five Volt AMTEC Multicell', M.L. Underwood, J.W. Suitor, R.M. Williams, M.A. Ryan, B. Jeffries-Nakamura and D. O'Connor, Proceedings of the 28th Intersociety Energy Conversion Engineering Conference, pp 1.855, (1993).

understand under what conditions such discharges can occur and 2) if they do, whether means exist to suppress them so that the advantages of high voltage series connection can be realized.

Under this task, we carried out a series of experiments in simulated AMTEC cell environments to identify the conditions under which such discharges will occur. We have reported the results of this investigation in the open literature and they are simply summarized here. The occurrence of DC electrical breakdown in a gas is dependent on many variables: electrode spacing, electrode shape, electrode material, electrode potential (breakdown occurs at V_b, the breakdown voltage), and gas pressure (or mean free path in the gas)[7]. Three of these variables are most strongly dependent on each other, namely the pressure, p, the electrode spacing, d, and V_b. The relationship between these three is often expressed in a Paschen curve similar to that shown in Figure 35 for argon.[8] It should be noted at the outset that while for many gases, electrical discharges occur only at initiating voltages above ~ 100 V to 200 V the presence of low pressure alkali metal vapor, however can reduce the work function of metal surfaces and might permit discharges to occur under unusually low voltage stress. Thermionic emission may initiate breakdown if the temperature of metallic surfaces is high enough. A schematic diagram of the test apparatus is shown in Figure 36 and the circuit used to carry out the measurements is shown in Figure 37. Measurements were also made of the breakdown voltage on a set of electrodes as influenced by the electrode temperature. The results of that test are shown in Figure 38. Similar data taken as a function of the sodium pressure at constant electrode temperature is shown in Figure 39.

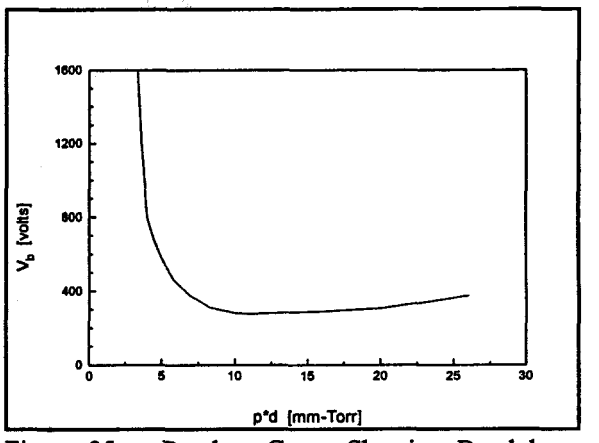

Figure 35 Paschen Curve Showing Breakdown Voltage As a Function of Pressure in Argon.

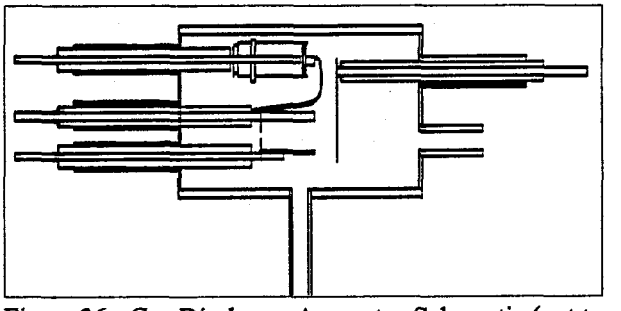

Figure 36 Gas Discharge Apparatus Schematic (not to scale).

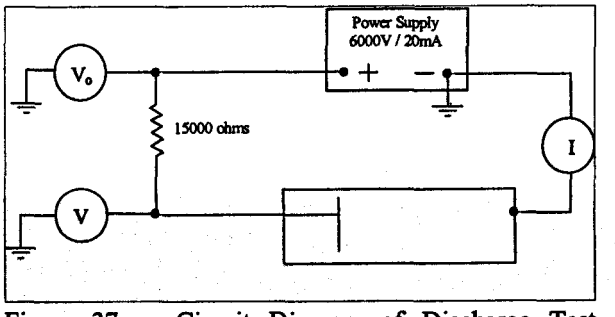

Figure 37 Circuit Diagram of Discharge Test Arrangement.

We conclude that under the simulated conditions in which we carried out these experiments, the discharge threshold in sodium vapor at pressures typical of the condenser space in AMTEC cells is well above 100 volts and should not lead to restrictions on series connection of cells to voltages below this value.

The experiments carried out at JPL that indicated a threshold voltage for discharge initiation were carried out with voltage applied between the cathodes on BASE tube sections and the surrounding metal vacuum chamber walls. As indicated above, the experiments done here were conducted with the test voltages applied

---

[7] 'Investigations of DC Electrical Discharges in Low-Pressure Sodium Vapor With Implications for AMTEC Converters', A. Barkan and T.K. Hunt, Proceedings of the 33rd Intersociety Energy Conversion Engineering Conference, Paper 350, (1998). This paper is attached as an appendix to this report.

[8] M. Knoll, F. Ollendorff, and R. Rompe, *Gasentladungstabellen*, p. 84, J. Springer-Verlag, Berlin, 1935.

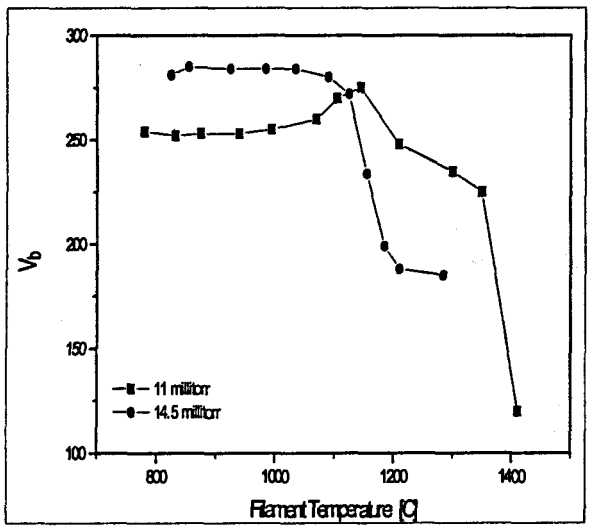

Figure 38 Breakdown Voltage as a Function of Electrode Temperature.

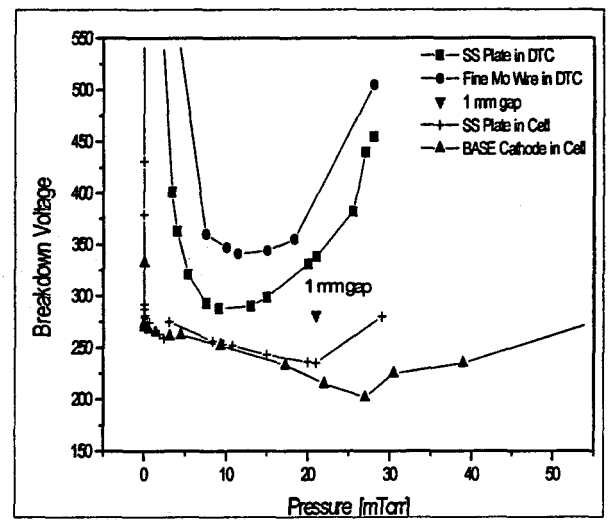

Figure 39 Plot of Discharge Threshold Data Taken on Series of Electrodes in Sodium Vapor at Pressure Shown.

between electrodes located completely in the interior of the test chamber. It appears that converters designed with separate feedthroughs for both anode and cathode leads so that the cell walls can float electrically, will not be susceptible to the limitations implied by the JPL results.

5.4 Low Cost BASE Production

At the outset of the program, it was expected that the commitment from Martin Marietta Specialty Components (MMSC) to work on low cost BASE production would yield useful results indicating the degree of cost reduction that could be expected from high volume production techniques. During the course of the program, MMSC was acquired, along with the rest of MM, by Lockheed Martin. While the initial letter of commitment indicates that MMSC/LMSC had expended the promised funds, and AMPS had supplied them with an initial supply of BASE precursor powder, no formal report of their progress was ever issued or provided to AMPS, and subsequent to their effort, LMSC appears to have been abandoned and closed down by the parent Lockheed Martin corporation.

Fortunately, several other programs have been funded which, taken together, appear to be accomplishing many of the tasks originally contemplated as being handled by LMSC. While the work has not been funded directly by this program, the accomplishments are relevant and we report here on some of the progress being made in those programs.

A NASA STTR program with AMPS and a group under Prof. R.M. Laine at the University of Michigan has addressed the problem of producing ultrafine BASE precursor powder at low cost. The powders are produced at the 'nano' scale with particle sizes in the range from 100's to 1000's of angstroms. At this size, if good compaction can be achieved by isostatic pressing, sintering should be possible at significantly lower temperatures than in either the conventional S4D or Zeta process powder cases. A major potential advantage of the nano-powder process[9] is that the chemical process involved in preparing the powders eliminates some of the impurities normally present in the low cost starting materials which one would prefer to be able to use. Initial experiments with sintering compacts from these nano-powder precursors were able to achieve only

[9] 'Synthesis of β"- Al_2O_3 Polymer Precursor and Its Pyrolysis to Ultrafine β"- Al_2O_3Powders', D.R. Treadwell, A.C. Sutorik, S.S. Neo, R.M. Laine, Proceedings of the 32nd Intersociety Energy Conversion Engineering Conference, p. 1214, (1997)

about 92 - 94 % density. Densities of order 93% or better are required to eliminate through the wall porosity which could compromise AMTEC cell performance by permitting excessive parasitic sodium leakage from the high pressure zone to the condenser space. While isostatic pressing such powders to adequate 'green' density may be difficult it may be possible to use electrophoretic deposition (EPD) in a proper suspension fluid to achieve higher densities. The current practitioner of EPD is Ionotec, Ltd.

Ionotec has recently provided a cost estimate for large scale production of BASE tubes by their conventional methods. The tubes were assumed to be 3.8 cm in diameter and 12.5 cm long or ~ 149 cm^2 in electrolyte area. At a power level of 0.4 W/cm^2 achieved in test converters designed with low condenser pressure drop such tubes are capable of ~ 60 watts output. Ionotec's estimated price at a production level of 400,000 tubes/year is $15 or ~$0.25/watt. NGK Insulators, Ltd. is currently the world's largest producer of sodium beta"-alumina - primarily for Na/S battery systems for load leveling applications. Their standard size BASE tube is 5.9 cm in OD and 48 cm long with a wall thickness of 0.7 mm, for a total area of ~800 cm^2. They estimate a high volume production cost of $15 for these tubes, produced in the automated plant they have in current operation. This corresponds to ~ $0.019/$cm^2$ or ~$0.047/watt at the presumed 0.4W/cm^2.

A program led by TDA Research[10] of Wheat Ridge, CO is developing a different nano-powder process with similar aims. TDA is also carrying out a program, currently in a second phase, with AMPS as a subcontractor for testing product, to develop a cermet electrode for AMTEC. The cermet is a mixture of BASE and TiB_2, such that it maintains both ionic and electronic conductivity. If successfully implemented, such electrodes could provide a dramatically enhanced electrode/BASE interface 'area', reduce internal cell impedance and increase electrode specific power density and efficiency. TDA has shown that it is possible to process BASE and TiB_2 into a ceramic form and this suggests that when perfected, it may be possible to produce BASE electrolyte bodies with integral cathodes and anodes in a single manufacturing sintering step. The resultant process saving would be important since cost is likely to be the rate limiting factor in commercialization for large scale terrestrial applications. The advantage of a mixed conductor electrode is in the reduction of the interfacial impedance between the cathode and the BASE. In current cell construction methods, this impedance is, in general, a more important factor than the thickness of the BASE. Figure 40 shows schematically the way in which ion/electron recombination can occur in 3 dimensions in a mixed conductor electrode thus dramatically enhancing the effective interfacial 'area' and reducing the corresponding impedance.

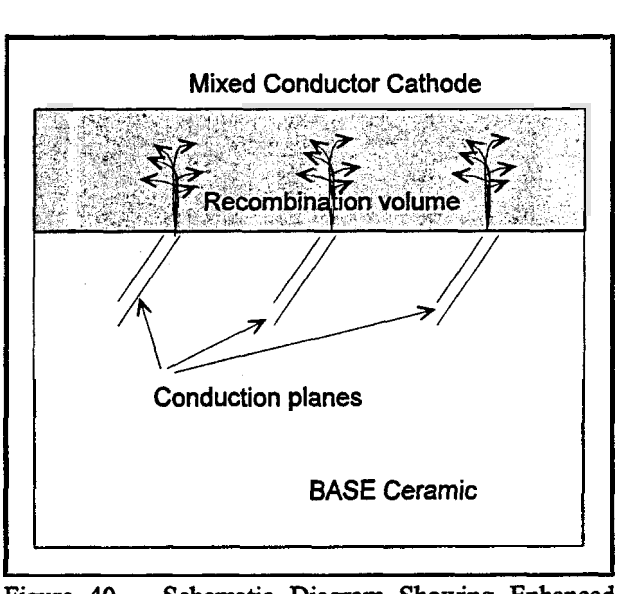

Figure 40 Schematic Diagram Showing Enhanced Opportunities for Ion/Electron Recombination in a 3-D, Mixed Conductor AMTEC Cathode.

A very different approach to forming BASE has been invented by a small company in Salt Lake City. A Phase 1 SBIR program at Materials and Systems Research, Inc.,(MSRI) has carried out the initial steps of a program which has shown that it is possible to create 'alpha' alumina components and subsequently

[10] TDA Research, Inc. 12345 West 52nd Ave., Wheat Ridge, Colorado 80033

convert them to beta"-alumina.[11] Because low cost methods for production of alpha alumina are well developed and inexpensive, and because the novel method can be carried out as a batch conversion process at temperatures of only ~ 1450 C, there is reason to believe that the cost of the BASE can be dramatically reduced- perhaps to levels that will keep it from remaining a strong influence on overall AMTEC production costs. The MSRI research and development has been supported in part by a Phase I SBIR from NASA. In addition to the low cost feature expected to be afforded by successful completion of the MSRI development, several technical gains appear to be possible when BASE is fabricated by this new method. Among these advantages are: 1) the resulting BASE has a strongly anisotropic ionic conductivity (5/1 higher conductivity through the tube wall compared to conductivity along the wall); 2) essentially no susceptibility to moisture due to the virtually complete absence of sodium aluminate at the grain boundaries; 3) tolerance of lower purity initial alpha alumina powder since processing temperatures do not reach the level at which silica forms a damaging glass phase; 4) the anisotropic ionic conductivity may obviate the need for an alpha insulator to help isolate series connected cells within a converter; 5) if the anisotropy is not sufficient to provide the needed ionic conduction isolation, by proper preparation of the initial alpha alumina body, it should be possible to produce monolithic tubes with a BASE section and an insulating 'alpha' section or sections. Such a monolithic tube would eliminate one difficult seal and save a significant cost.

Each of these approaches holds promise for a very significant reduction in cost. The MSRI process appears also to offer a method for low cost production of potassium beta"-alumina. All K-BASE produced so far has been made by high temperature ion exchange of Na-BASE with the vapor of one or another potassium salts. Early work on K-BASE was conducted at Ford by Crosbie and Tennenhouse. Further work along these lines was carried out at JPL by Williams et al who achieved higher conductivity material and measured the conductivity over a wider range of temperatures. Lowering the cost of K-BASE is important as its use offers the potential of a 3 - 5% improvement in total efficiency relative to Na-BASE cells of similar design operated at the same temperature.

It is of particular interest that the patented process that MSRI has developed has been shown to work for the formation of potassium BASE directly from the same ceramic precursor that serves for sodium BASE. Testing of the conductivity of the K-BASE produced in this way has not yet been conducted at the operating temperatures considered most probably interesting for AMTEC applications.

5.5 Fabrication Methods

Wire Wrap Outer Current Collector The use of a woven metal screen as the principal outer current collector (OCC) contact with the cathode of AMTEC cells has been the standard. Copper mesh screens were used until January 1998 at which time a switch to molybdenum mesh was made for all subsequent BASE tube assemblies. Assembling the OCC using the relatively stiff, woven Mo screen is time consuming and hence expensive and may not provide the best contact. We have investigated the approach in which the exterior of the tube is simply closely wrapped with Mo wire and a bus wire lead trapped under the Mo coils to extract the current.

It was anticipated that having many turns of relatively fine Mo wire would make more frequent contact with the cathode film surface and reduce contact resistance at that interface and that it would be quicker, simpler and hence less expensive to assemble. The principal concern was that since Mo has a lower coefficient of thermal expansion (CTE) than BASE, a tight wrapped Mo coil, expanding less than the BASE on which it was wrapped, might undergo plastic deformation under the mechanical loads during heat up to full AMTEC operating temperatures. If this occurs, the wrapped wire might then become loose at all lower temperatures and thereafter make poor contact with the cathode. Thermal cycling would thus cause

[11] A.V. Virkar, J-F. Jue, K-Z Fung (2000) "Alkali-Metal- Beta and Beta"- Alumina and Gallate Polycrystalline Ceramics and Fabrication by a Vapor Phase Method", U.S. Patent No. 6,117,807.

problems. Thermal cycling tests of performance of tubes prepared in this way should provide a reasonable test of the approach's effectiveness.

METC 69 was prepared with a Na-BASE tube and a closely wrapped (with each turn touching its neighbor) Mo wire of diameter 0.0125 cm with a wrapping tension supplied by a 400 - 450 gram weight and single pulley system. This tension weight is approximately half that used routinely in wrapping the same diameter Mo wire to hold the normal Mo screen tight to the cathode surface. The METC was then assembled in the usual way, loaded with Na and run at a range of temperatures up to 850 C. A series of ten runs were made with the cell cooled down to room temperature between each pair of runs. Figure 41 shows the peak power from this cell as it was recorded at various temperatures during each thermal cycle. Figure 42 shows the power at a current of 2.0 A over the 10 thermal cycles with the operating temperature as the parameter for the different curves. The 2 A operating point is reasonably reflective of the conditions under which a single tube of the ~ 6 cm^2 type tested here runs at highest efficiency. These tests were done in the vapor anode mode.

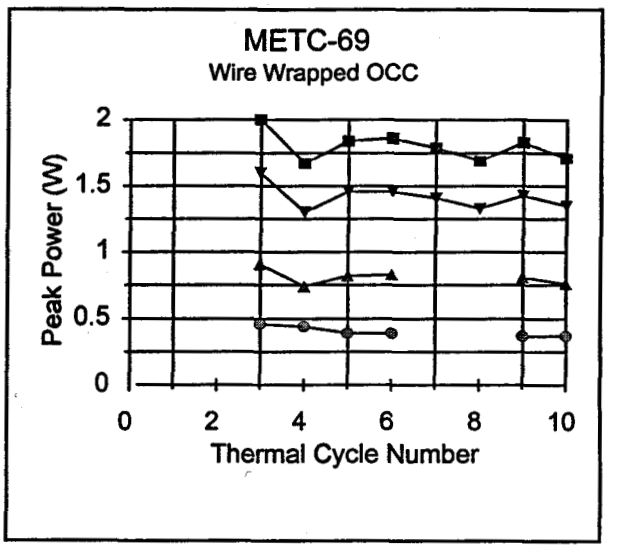

Figure 41 Peak Power of Wire (only) Wrapped METC.

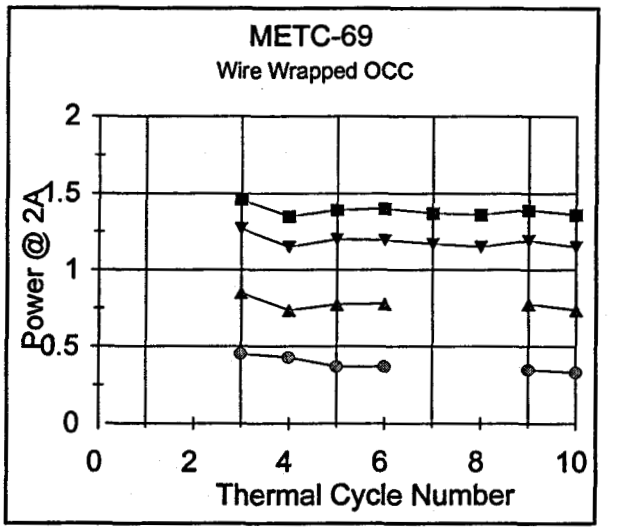

Figure 42 Power at 2 Amperes ~ Normal Operation Pt.

It can be seen from these two plots that a modest decrease in output occurred over the first 3 cycles but that the performance was quite stable from the 4th cycle onward. While this might be expected to occur for the highest temperature reached during the cycles, it appears to be nearly true for the lower temperature data curves as well, indicating that plastic stretching of the Mo wire is not very serious over this temperature range and number of cycles. The absolute value of the peak power puts this cell in the top 5 or 6 sodium METCs run thus far. The cell was run and tested after each thermal cycle to 500 C. The test temperatures were 600 C, 700 C, 800 C and 850 C and the plots show minimal change after the initial cycle, indicating that any "ratcheting" of the Mo wire ceased to cause changes in output after the first run. This appears to have been true even at the lower 600 C test temperature for which loosened Mo wrap might have been expected to make the most difference.

A second cell, METC-81, with a wire wrapped OCC was run initially to examine the performance of a closed end tube and its Weber anode. Following the initial run it was stored at room temperature for several weeks, then revived and run again for its 3rd thermal cycle. The initial, baseline, 2.0 A power level at 850 C in vapor mode was 1.35 watts or .226 W/cm^2. In the rerun it reached 1.46 Watts or 0.245 W/cm^2 at the same temperature conditions. Further cycle tests were not possible as the cell became shorted after failure of one of the external test system heaters.

Conclusions

The use of a wire wrap only outer current collector does not appear to adversely affect the power output of the small (7.6 mm O.D.) BASE tubes. The tests on tubes prepared in this way seem to indicate that they

perform near the upper end of the usual range. Thermal cycling of the tubes appears to cause a small initial decrease in power output that, for the highest temperatures reached, stabilizes after a few cycles. Some decrease in output at lower temperatures appears to persist with increasing cycles, at least up to the 10th.

Because the fabrication of the OCC is substantially simpler without the Mo screen, use of the wire wrap appears to be justified for those tests, such as the METC type, which are intended to examine other cell properties. With sufficient further testing of the wire wrap only OCC, it should be possible to move this process into the 'standard' category.

5.6 Burner Testing and Hydrogen Infiltration

The major terrestrial applications and in particular any vehicle applications envisioned for AMTEC are expected to rely primarily on the combustion of hydrocarbon fuels as the source of heat. It is probable that even for solar heated terrestrial AMTEC power systems, it will be desirable to incorporate a backup combustion heat source to provide continuity during extended periods of low insolation. The ability to operate with a variety of heat source types is an important advantage for AMTEC relative to both fuel cells and I.C. engines. Failing truly complete combustion of hydrocarbon fuels, however, the exhaust stream generally contains free hydrogen and most metals suitable for use in the hot zone of AMTEC cells have a significant permeability for hydrogen at AMTEC operating temperatures. Infiltration of hydrogen or other gases into the low pressure condenser space of an AMTEC cell can produce there a pressure level that will tend to suppress the alkali metal vapor flow from cathode to condenser and thus reduce the output of the cell. Further, if hydrogen becomes trapped within the high pressure zone of the BASE electrolyte system, it may buffer the arrival of additional alkali metal vapor and tend to starve the anode.

It is expected that cell performance should begin to be affected when the pressure of a non-condensible gas in the condenser space reaches a level for which the mean free path of sodium atoms leaving the cathode film outer surface becomes shorter than the spacing between the cathode and the interior walls of the cell. Two direct approaches to the hydrogen infiltration problem were considered: 1) the use of specialized coatings with low hydrogen permeability on the exterior surface of the hot zone cell wall; 2) incorporation of active getter material into the condenser space of the cell to sequester the hydrogen that does pass through the cell wall. In practice, a combination of the two approaches may be optimum. The properties and capacities of commercial getter materials[12] are well characterized so it is expected to be sufficient to measure the infiltration rate as a function of temperature and hydrogen concentration in the combustion exhaust to allow a determination of the probable effectiveness and useful lifetime of a getter supply of a given mass incorporated into the cell.

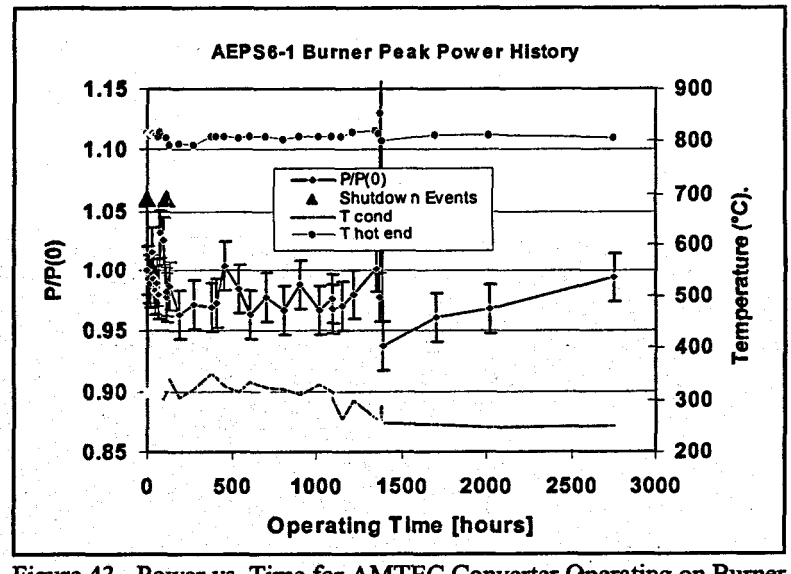

Figure 43 Power vs. Time for AMTEC Converter Operating on Burner at 800 C.

Care must be taken not to place the getter in physical contact with

[12] SAES Getters is a leading supplier of these materials. The usual components include Fe, V and Zr.

active areas of the BASE tube since zirconium is capable of capturing the oxygen from the sodium oxide in the conduction planes of the BASE and thereby denaturing the BASE and destroying its ionic conductivity.

Experiments Our initial tests of cells on propane burners confirmed that the problem can occur rapidly at normally desired hot side operating temperatures. A dummy test cell apparatus was designed, built and run to examine the efficacy of conventional coatings and the capability of commercial getters to sequester hydrogen that does pass through the hot zone cell wall. The details of this experiment are incorporated in the paper published in the IECEC proceedings in 1999[13]. This paper is included in this report as appendix C. More recent experiments in a burner system provided to AMPS by Teledyne Brown Engineering on another program have shown that the hydrogen problem has at least one solution. Figure 43 shows a normalized plot of power vs time for a simple, small AMTEC cell operating on a burner at 800 C. This cell has a Haynes alloy heat input surface and contains a small amount of SAES ST707 getter. The power from this cell, which appears to fluctuate primarily due to burner heat distribution inconsistencies, is essentially unchanged after nearly 2500 hours of operation.

3. Cell Design and Modeling

Several converter module designs have been considered during the Phase II period. The key consideration was that a useful module should be capable of being 'stacked' or bundled in a way that allows a straight forward transition to higher power complete systems. The radial converter shown schematically in Figure 44, heats individual cells from a central channel and allows for stacking of these converters around

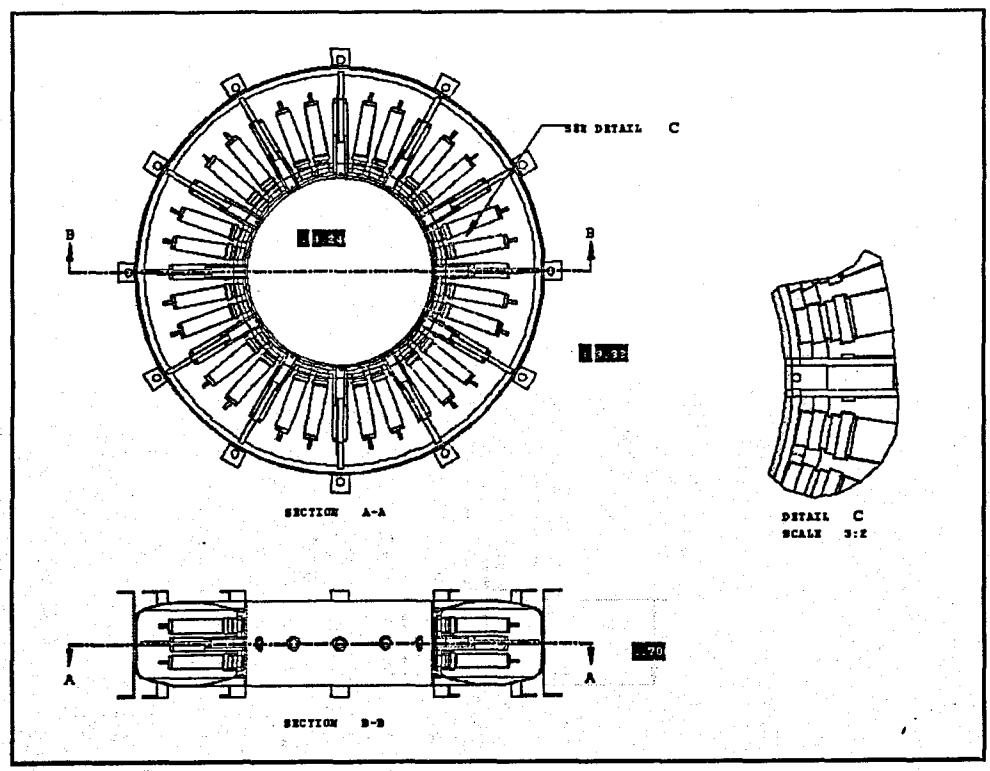

Figure 44 Donut Cell Configuration for 200 Watt AMTEC.

[13] 'Hydrogen Permeation Issue for Gas Fired AMTEC Systems', R. Metal., D.A. Butkiewicz, K.F. Childs, D.D. Hayes, R.C. Svedberg and T.K. Hunt, Proceedings of the 34th Intersociety Energy Conversion Engineering Conference, # 2557, (1999).

a central combustion source whose length determines the number of converters and thus the overall output of the system. The analysis and experimental data on the radial converter are described in detail in Appendix B. The general considerations of burner design and in particular the design of radiant coupled burners capable of operation in relatively narrow heater wells is discussed in detail in Section 6.

A second converter design for testing larger output scaled up system in an end-heated configuration, has made use of a 'chimney' design in which the vapor transport path from the hot zone with the BASE tubes to the condenser is constricted to a narrow cylinder. This design concept creates a substantial radiation shielding effect with only minor increases in the condenser AM back pressure that reduces the output voltage. The initial 35 We converters built and tested in this design are simply scaled up versions of spacecraft converter designs. The design, indicated schematically in Figure 45 uses eight 15 mm diameter BASE tubes connected in series to increase the output voltage and avoid extremely high currents. Figure 46 shows a photograph of this cell taken prior to initial testing. This converter is a simple scale-up from the type of converters produced for spacecraft and is only representative of this direction.

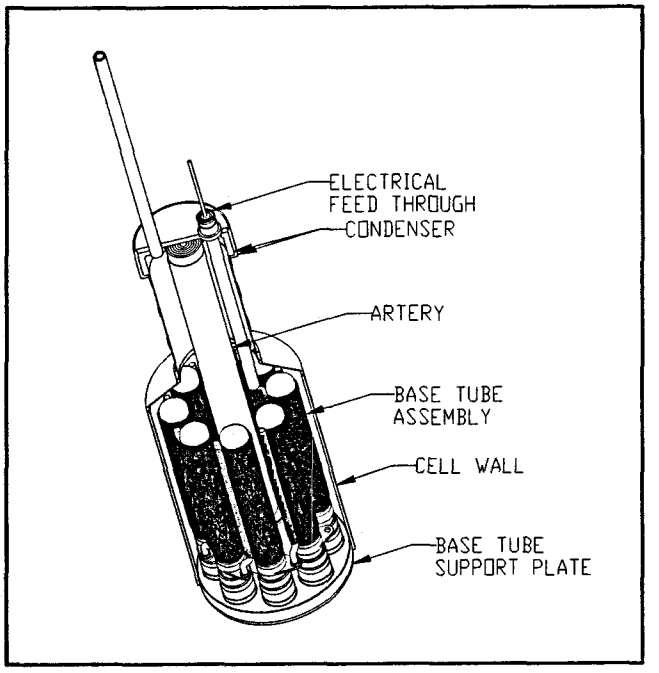

Figure 45 GF1 Schematic View.

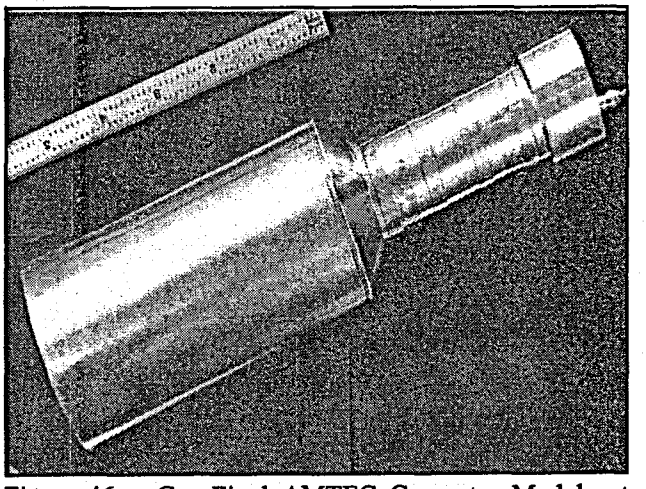

Figure 46 Gas Fired AMTEC Converter Module at Nominal 35 Watt Output.

6. Burner System Investigations

The system work carried out in this program also included a significant effort related to coupling combustion products to surfaces of the type required for input to AMTEC converter modules. This section reports on that effort which was carried out by Dr. Rahul Mital and was an extension of his previous work.

Since high system efficiency is based not only on an efficient converter, but also on a high efficiency fuel combustor, extensive research was carried out to identify the right burner which could provide the required heat flux with minimal pollutant emission. It was established that a radiant burner with high radiation efficiency which when complemented by convective heat transfer would be ideal to provide the required heat from the burner assembly to the AMTEC cells. Various conceptual designs of burners were fabricated and tested. Some commercial burner materials were also tested to compare the burners available in the market to the innovative burner designs developed at AMPS, Inc. Besides high radiation efficiency, two other crucial requirements of these burners were, a high turn down ratio and low pollutant emission. Models were also developed for these burners to understand their behavior in terms of radiation efficiency, turn down ratio and flame location at various firing rates.

Radiant burners are of interest for the hybrid electric vehicle application due to their desirable characteristics of high radiant heating rates and minimal pollutant emission. During combustion, due to the high surface area to volume ratio in the porous burners, heat is exchanged convectively between the gas and the solid. This reduces the burnt gas temperature and hence lowers the NO_X emission. The porous medium gets hot and emits thermal radiation which is absorbed, scattered and emitted in both upstream and downstream directions. The downstream radiation heats the load, while the radiative feedback upstream, along with solid matrix thermal conduction, preheats the incoming fuel air mixture. This increases the flame speed and the lean flammability of the mixture. Description of the various burners that were investigated, testing procedures, results of the tests conducted and comparison of the results with the model are discussed in the following.

Experimental Arrangement: The experimental apparatus consisted of a burner and associated flow and pressure monitoring instruments (Fig. 45). Experiments were conducted on various industrial burners and several innovative reticulated ceramic burners. Industrial radiant burners involving metal fiber, ported metal with screen, ported metal fiber with screen, ported ceramic with screen, and ported metal fiber burners were tested (Table 1). Equivalence ratio, ϕ, is defined as the fuel/air ratio divided by the stoichiometric fuel/air ratio. For fuel-rich systems, there is more than the stoichiometric amount of fuel and $\phi > 1$. For the reticulated ceramic burners, a circular burner with a 7.5 cm diameter was studied with various types of reticulated ceramic tiles (Table 2). A schematic diagram of this 7.5 cm diameter burner is shown in Fig. 45. A sintered steel plate provided a uniform flow distribution and prevented flashback into regions upstream of it. The flame motion could be observed through the quartz window allowing the establishment of a stable operating range. The reticulated ceramic tiles were made of Cordierite with a silicon carbide based coating (LS-2) on the flame support layer and were manufactured by Hi-Tech Ceramics, Inc. Commercial grade methane (99.5 % purity) and air were mixed upstream of the burner to obtain a homogeneous mixture. The flow rates were measured using rotameters and choked flow orifices. The flow meters were calibrated using a dry test meter and the calibrations were verified using gas chromatography (Shimadzu GC-8AIT).

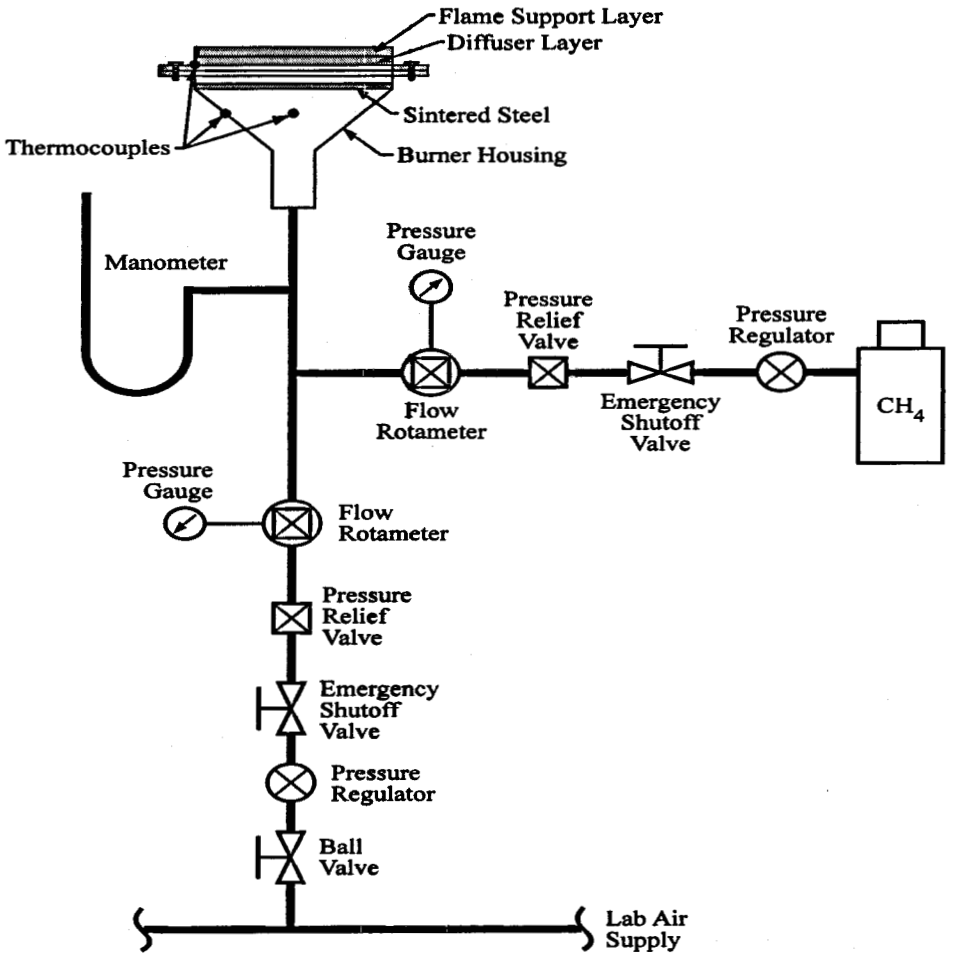

Figure 45 Schematic of the Experimental Arrangement

Table 1 Details of the commercial burners investigated.

No.	Type	Description	Equivalence Ratio	Firing Rate Range (kW/ m^2)
1	Metal Fiber	FeCrAlY, 3.5 mm, Coarse fiber (50 micron), Fine fiber (20 micron)	0.6 - 1.0	236-315
2	Metal Fiber	FeCrAlY, 3.0 mm, Coarse fiber (20 micron), Fine fiber (20 micron)	0.6 - 1.0	236-315
3	Ported Metal Fiber with Screen	Burner area (4"x 16"), Screen 1" from burner surface	0.9	236-315
4	Ported Metal with Screen	Burner area (6"x8"), Screen 5/4" from burner surface	0.9	95-236
5	Ported Ceramic with Screen	Burner area (6"x8"), Screen 1" from burner surface	0.9	158-315

Experimental Conditions: A number of commercial and novel reticulated ceramic burners were investigated. The idea was to improve the current understanding of these radiant burners enough to

identify the best burner for the Hybrid Electric Vehicle application. The burner descriptions for each of them are listed in Tables 1 and 2. To accomplish this objective, the performance characteristics of these burners was measured in terms of radiation efficiency, pollutant emission indices and stability range. The flame support layer material for all the ceramic burners was cordierite coated with a silicon carbide based coating (LS-2), and the diffuser layer was made of cordierite. For the bi-layered samples, the thickness for the top layer ranged from 3 mm to 10 mm. The samples were either 10 pores per inch (ppi) (4 ppc) or 20 ppi (8 ppc). The bottom layer (diffuser layer) was 65 ppi or 26 ppc and 19 mm thick for all cases. The tri-layered samples had an additional layer in the middle which was a 3 mm thick , 80 ppi or 32 ppc layer.

Table 2 Details of Reticulated Ceramic Burners

Burner No.	Size (cm^2)	Flame Support Layer		Diffuser Layer	
		PPC	Thickness (mm)	PPC	Thickness (mm)
1	45	4	3.2	26	19
2	45	4	6.5	26	19
3	45	4	9.6	26	19
4	45	8	3.2	26	19
5	225	4	3.2	26	19
6	225	4	3.2	32/20	3.2/16.0

For the commercial burners, the operating conditions are listed in Table 1. For the reticulated ceramic burners measurements were made for a wide range of operating conditions, and these are listed in Table 3.

Table 3 Reticulated Ceramic Burner Measurements Conditions

Burner No.	Firing Rate (kW/m^2)	Equivalence Ratio
1	150-650	0.6-1.0
2	150-650	0.6-1.0
3	300-650	0.65-0.8
4	225-475	0.9
5	300-650	0.6 - 1.0
6	300-650	0.6 -1.0

Detailed study of the reticulated ceramic burners was carried out since they proved to be the most promising out of all the burners tested. Evaluation of the stability range for the different burners was carried out to determine the stable operating conditions. This helped to identify the range where the burners were in the radiant mode, i.e., the flame was within the support layer and the burner had an orange glow. The stability limits were bound on the two ends by either lift off (lifting of the flame from the rim of the burner) or flashback (traveling of the flame upstream to the diffuser layer). A flame was considered stable if the burner could be fired at the specified operating condition for several hours without either flashback or lift off.

Experimental Procedures

As mentioned earlier, the performance characteristics of these burners was measured in terms of radiation efficiency, pollutant emission indices and stability range. The following is a description of the experimental procedures used to make these measurements.

Radiation Efficiency: The first step was to identify the burners which have the highest radiation efficiency. Interestingly, wide range of radiation efficiencies (varying from 15% to 50%) have been reported in the literature for similar commercial burners operating under similar conditions. The wide range is believed to be due to the non-availability of a standard radiation efficiency measurement procedure. Industrial brochures claiming radiation efficiencies in excess of 50% for the current gas infra-red emitters can be commonly found. However, a first law analysis, assuming no heat losses from the side walls of the burner and complete combustion, reveals, that these numbers may be unrealistically high. Under ideal conditions of surface emissivity equal to unity and equilibrium between gas and solid temperature (infinite value of volumetric heat transfer coefficient), the maximum radiation efficiency for a firing rate of 315 kW/m^2 and an equivalence ratio of 1.0 can be no more than 53%. Another cause of discrepancy is that most researchers resort to single point measurement under the diffuse surface assumption. The procedure is practical and convenient but introduces high uncertainties if the burner surface is nonuniform and also if the real surface deviates considerably from the diffuse surface assumption.

For an unambiguous comparison of the thermal performance of different radiant burners standardized multi-point radiation efficiency measurement methods which give more accurate results for both diffuse and directional burner surfaces were developed. These methods essentially focus at capturing the total hemispherical radiation enclosing the burner surface. In another approach, black and silver coated water calorimeters were used to obtain the total, radiative plus convective, and only convective heat transfer rates from the burner, respectively. The radiative efficiency is obtained from the difference of these two reading and is used to qualify the results obtained by the standardized multi-point approach.

Standardized Radiation Efficiency Measurement Procedure The total radiative output of the flame was obtained by measuring the heat flux distribution incident on the surface of an imaginary cylinder enclosing the burner and integrating with respect to the appropriate differential area element on the surface. Two different burner sizes were investigated in the present work. One was a (0.15 m X 0.15 m) square industry size burner and the other was a circular (0.075 m diameter) laboratory size burner. Figure 46 shows schematically the arrangement for the measurement of radiative flux around the radiant burner. The radiative flux was measured using a 150° view angle radiometer with a sapphire window (Medtherm Corporation, Model 64P-1-22). The transducer provided a self-generated 10 millivolt output at the design heat flux level. The transducer output is linearly proportional to the net heat transfer rate absorbed by the sensor. The radiometer was connected to a digital heat flux meter (Medtherm Corporation, Model H-201) which amplified the signals by a factor of 100 times and the output was processed by an A/D converter and stored in a computer.

The total radiant power emitted by the burner was calculated as:

$$Q_{rad} = 2\pi \int_0^R q_b r dr + 2\pi R \int_0^H q_s dx \qquad (1)$$

where q_b is the heat flux incident on a differential area element ($2\pi rdr$) at the base of the cylinder and q_S is the heat flux incident on a differential area $2\pi Rdx$ on the side of the cylinder. The radius of measurement R was selected to ensure that the entire burner surface was in the field of view of the detector at all positions, and the height H of the cylinder was selected such that the heat flux at this height was close to the background value.

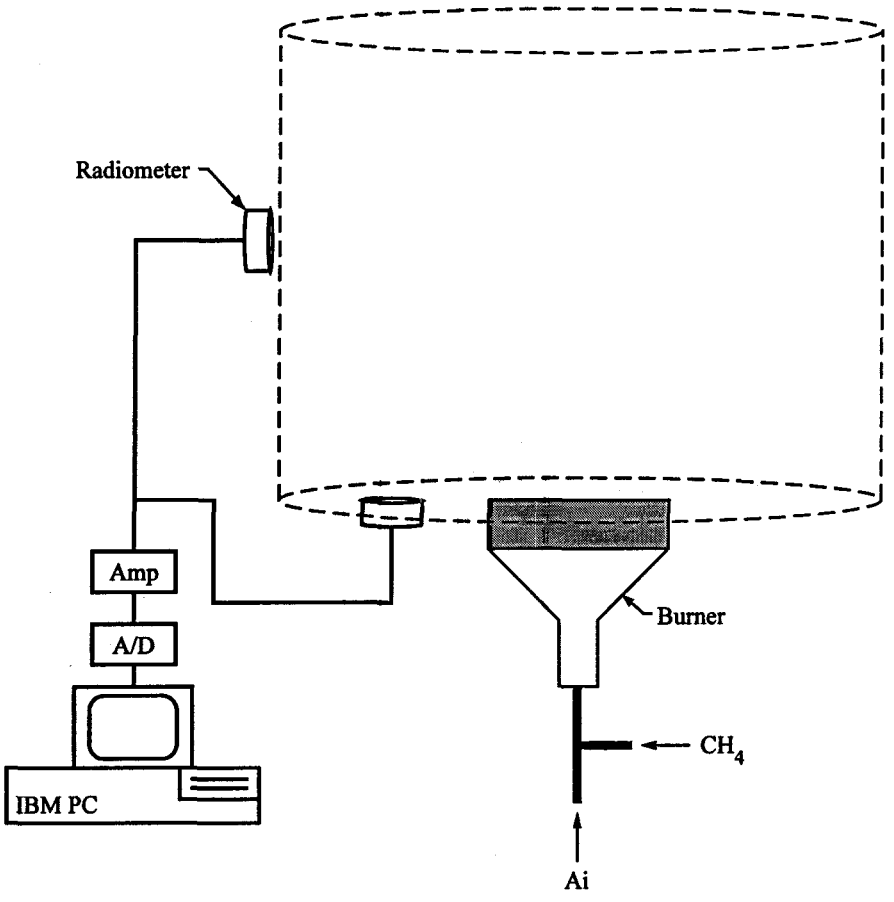

Figure 46 Schematic of the Arrangement for Radiation Efficiency Measurements

The radiation efficiency was calculated by taking a ratio of the total radiative power emitted by the burner to the surroundings (Q_{rad}) to the energy release rate in ideal combustion at standard state (Q_{chem}):

$$X_R = Q_{rad} / Q_{chem} = Q_{rad} / m_F (LHV) \qquad (2)$$

where m_F is the fuel mass flow rate and LHV is the lower heating value of the fuel.

Calorimetric Approach to Determine Radiation Efficiency: The data of the standardized radiation efficiency measurement method were qualified using black and silver coated water calorimeter results. To obtain a measure of combined radiative and convective heat transfer efficiencies, a 30 cm diameter water calorimeter was placed directly above the burner (Fig. 47). It was coated black so that the surface absorptivity was close to unity (0.96). Water was circulated through the calorimeter and the burner transferred energy by convection and radiation to the water through the calorimeter plate. Some water condensation from the exhaust gases was observed on the calorimeter plate. This was avoided by installing a hot water bath in the line and keeping the calorimeter temperature above the dew point. The heat transfer efficiency of the burner decreases as the gap between the burner surface and the calorimeter plate increases. This is understandable since the external air entrainment increases with increase in gap. This entrainment reduces the gas phase temperature and carries away part of the energy with it, both factors contributing to a decrease in the convective efficiency. Below a gap of approximately 2.5 cm, the heat transfer efficiency tends to become constant. To delineate the convective and radiative efficiencies, a measure of convective heat transfer efficiency alone was obtained using a silver coated water calorimeter. Since the surface reflectivity of the calorimeter

plate is close to 0.95, all radiation is reflected and heat transfer between the burner and the calorimeter takes place by convection only. The difference between the readings of the two calorimeters yields the radiation efficiency of the foam ceramic burner.

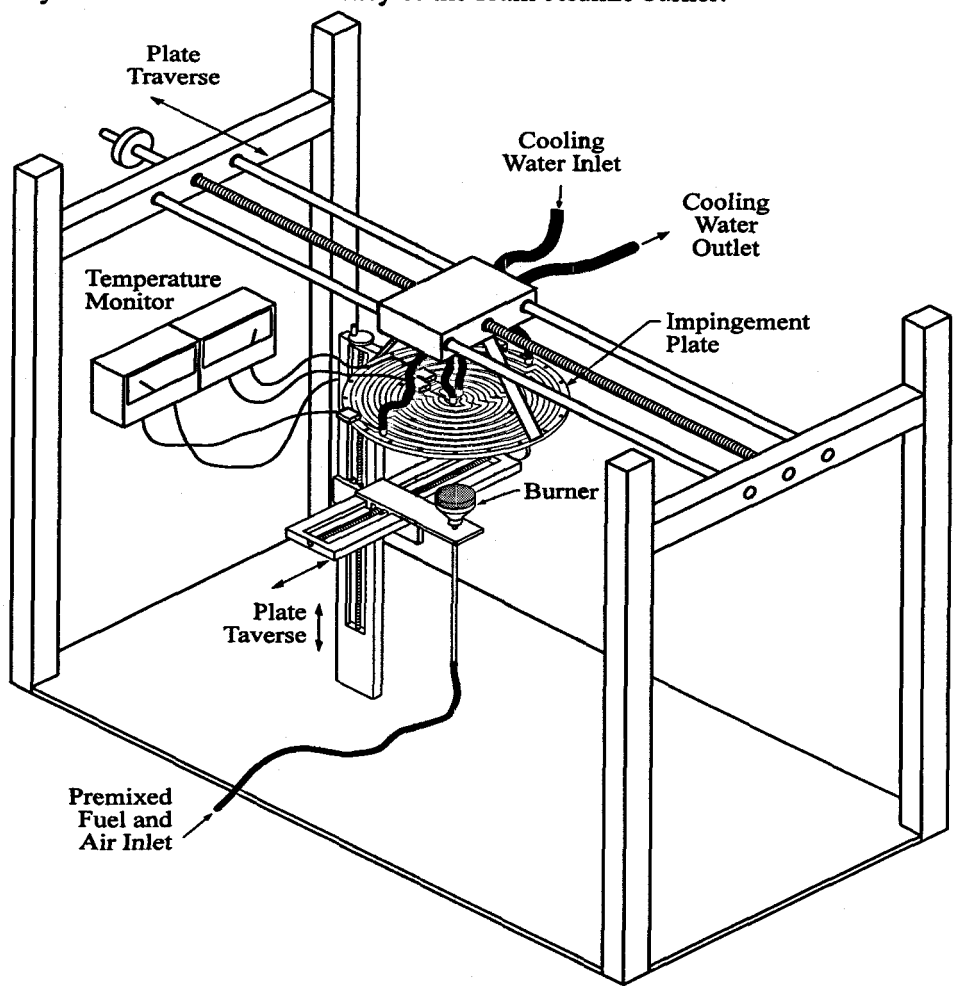

Figure 47 Schematic of Calorimetric Determination of Radiation Efficiency

For the standardized radiation efficiency measurement procedure, the maximum standard deviation obtained from repeated measurements was ±1.5. Generally, however, it was less than ±1.0. For the calorimetric efficiency, uncertainty in water mass flow rates is estimated to be ±3 %, while the uncertainty in water inlet and outlet temperature difference is around ±4 %, giving a net uncertainty of ±5 % in the heat transfer measurements.

Pollutants Emission Measurement: Emissions of CO, HC (CH_4 equivalent) and NO_X from the burners were measured for various operating conditions. A schematic of the experimental arrangement is shown in Fig. 48. The measurements were made in the exhaust stream using a chimney to obtain the average pollutant emission for the burner after quenching of the reactions. The measurement location was about 1.5 meters from the burner surface to ensure uniform mixing.

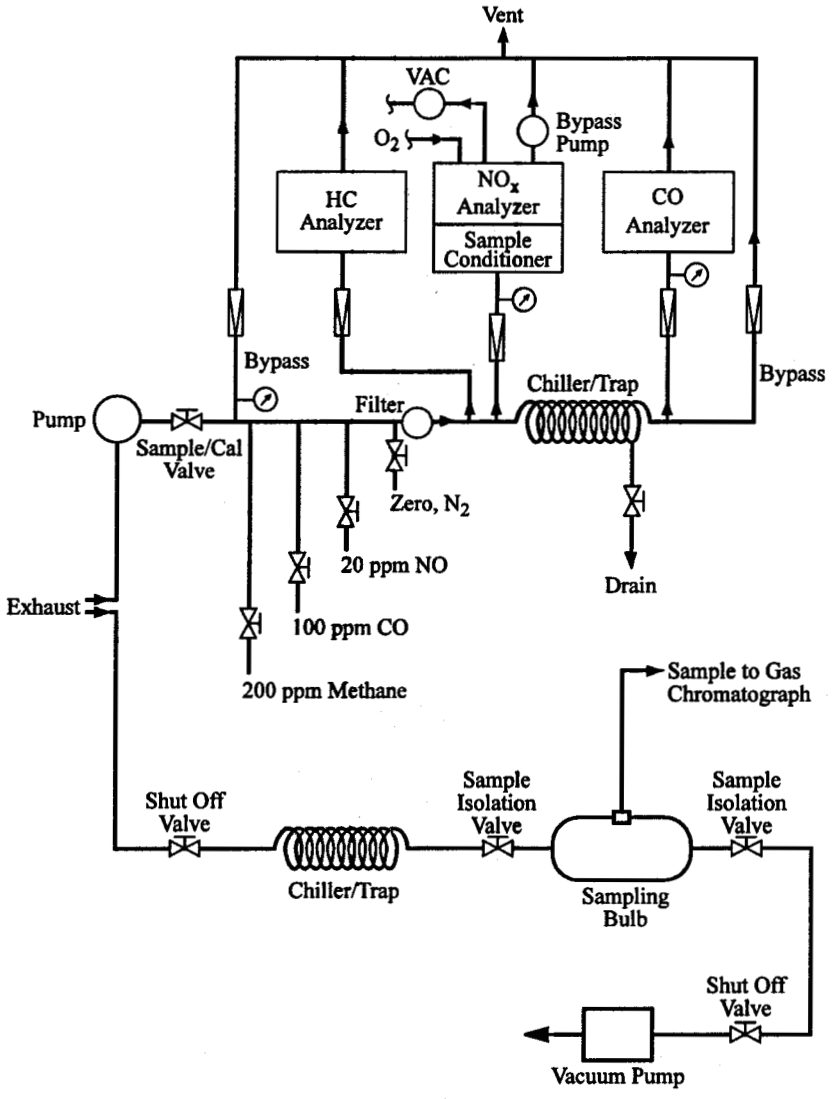

Figure 48 Schematic of the Exhaust Gas Analysis System

A sample profile across the duct diameter showed a change of less than 5% hence centerline mole fraction data were treated as the average values. The sample was drawn from the exhaust and passed through a chiller to remove water vapor before directing it to a gas filter correlation based CO emission analyzer. A flame ionization detector based HC analyzer with a temperature controlled heated zone to eliminate condensation problems was utilized. A sample conditioner was utilized for the chemiluminescence based NO_X analyzer as well. The CO_2 concentrations in the exhaust sample were measured using a non-dispersive infra-red analyzer (Model 880 from Rosemont Inc.) and a gas chromatograph (Shimadzu, GC-8AIT). The CO analyzer (Model 48), HC analyzer (Model 51) and NO_X analyzer (Model 42) and the sample conditioner (Model 800) were all procured from Thermo-Environmental Instruments. The sample flow rates through each of the analyzers were maintained in the recommended range by using flow control valves and bypass lines. The zero and span readings of all the analyzers in the appropriate range were calibrated before and after each test. The mole fractions measured by the analyzers were converted to mass fractions of each pollutant species using its molecular weight. The emission index for the individual species was calculated by dividing this measured mass fraction of pollutant in the product stream by the mass fraction of methane in the

unreacted incoming stream based on the operating equivalence ratio. The emission index for NO_x was calculated by adding those of NO and NO_2. Thus the eventual conversion of NO to NO_2 was not considered. The ambient air readings for NO_x were in the range of 0.2-0.5 PPM, for HC they were typically in the 2-6 PPM range and for CO they varied between 0.3-0.8 PPM. The NO_x and CO data have an uncertainty of 15% and HC data have an uncertainty of 25% mainly due to the variations in the burners from sample to sample, degradation of the tile with increasing operating hours, and also due to variations in the calibration gas and limited number of samples. The data were repeatable within 10% for NO/NO_x and CO and within 20% for HC with a relatively new burner and with a single set of calibrations for the instrument zero and span readings.

Stability Range: The stability range is defined as the maximum and minimum equivalence ratio at a fixed firing rate for which a stable radiant flame could be obtained over the entire surface of the flame support layer. Initially, a flame was stabilized by varying the air flow rate for a fixed fuel flow rate. The air flow rate was then incremented in small steps and the flame was allowed to reach a steady state after every increment. This process was continued until the flame started to lift from the edge of the burner. This condition was defined as the blow off limit of the burner. After reaching the blow off limit, the air flow rate was further increased in small increments until the whole flame lifted off the burner surface and finally extinguished. This was defined as the lean limit of the flame where no combustion was possible. The flame was then ignited again at an air flow rate below the blow off limit and allowed to stabilize. The air flow rate was then decreased in small steps. Flame was allowed to reach a steady state after each air flow adjustment. As the air flow rate was reduced towards stoichiometric, a condition at which the flame moved into the diffuser layer was reached. This was defined as the flashback condition for the burner. Once the flame moved into the diffuser layer, it progressively kept moving upstream and a stable flame could not be obtained. A gas chromatograph was used to verify the equivalence ratio for flashback and blowoff limits.

A high turn-down ratio for the radiant burners is highly desirable. This allows operation of a burner for a wide range of radiant outputs to accommodate power levels varying from 15 to 60 kWe for the hybrid electric vehicle. The turn-down ratio of the present burners was measured at an equivalence ratio of 0.9. The upper limit on firing rate may be provided by the flashback condition or by thermal degradation of the burner material while the lower limit on firing rate may be provided by flow nonuniformity or by quenching of flame due to heat loss to the burner tile.

Spectral Intensity Measurements: Spectral radiation intensity measurements are of interest for evaluating the performance of burners utilizing wavelength selective emitters and absorbers. The radiant heat transfer can be enhanced by matching the spectral emission of the burner with the absorption characteristics of the object to be heated, which in the present case would be the AMTEC cells. However, the spectral measurements are useful for other future applications as well. A typical application being the Thermophotovoltaics. For this application the key requirement is a high temperature emitter that emits radiation selectively at wavelengths near the band-gap of silicon PV cells.

In the present work, measurements were made to identify the wavelength dependence of radiation intensity to assist in effective transfer to the load. For example, in drying and heating applications the radiation transmission of the paperweb is almost zero for approximately 2.7 - 4.0 μm wavelength range. Most of the radiation below 2μm is transmitted. Therefore, for effective drying of paper it would be advantageous to have an infra-red radiator which emits bulk of its radiation in the longer wavelength (> 2μm) range. Similarly if the hot end of the AMTEC cells can be coated with a surface whose absorption characteristics match with the emission characteristics of the burner, the radiant heat transfer efficiency is expected to increase considerably.

The experimental arrangement for the spectral radiation intensity measurements is shown in Fig. 49. It included a PbSe detector, a monochromator (Oriel model 77250), three monochromator gratings to cover the wavelength range of interest, an order sorting filter, a 6 blade optical chopper and a collection probe. The chopper was necessary because the PbSe detector responds only to a modulated signal. The order sorting filter was used to eliminate monochromator order artifacts from the data. The PbSe detector was provided with a bias voltage of 50 V and a preamplifier DC bias voltage of ±15 V and operated in the wavelength range of 1 to 5 μm. All optics were mounted on a precision optical slide to facilitate alignment.

The system was aligned using a He-Ne (632 nm) laser and then calibrated using a blackbody at 1272 K. The signal was chopped by a rotating wheel optical chopper at 250 Hz and input into a high-pass filter set at 125 Hz. The output of the high-pass filter was fed into a lock-in amplifier, and the output of the lock-in amplifier was passed through a low-pass filter set at 100 Hz, before being read into a data acquisition program and simultaneously being observed on an oscilloscope. The calibration constant was obtained by dividing the output voltage with the blackbody intensity at that particular wavelength and 1272 K temperature,

$$C_\lambda = V_\lambda / I_{b\lambda} \tag{3}$$

where the subscript λ represents the wavelength of measurement, C is the calibration constant, V is the voltage, and $I_{b\lambda}$ is the blackbody intensity calculated using Planck's function. The calibration constant varied with wavelength because of non-linearities in detector, grating and filter response.

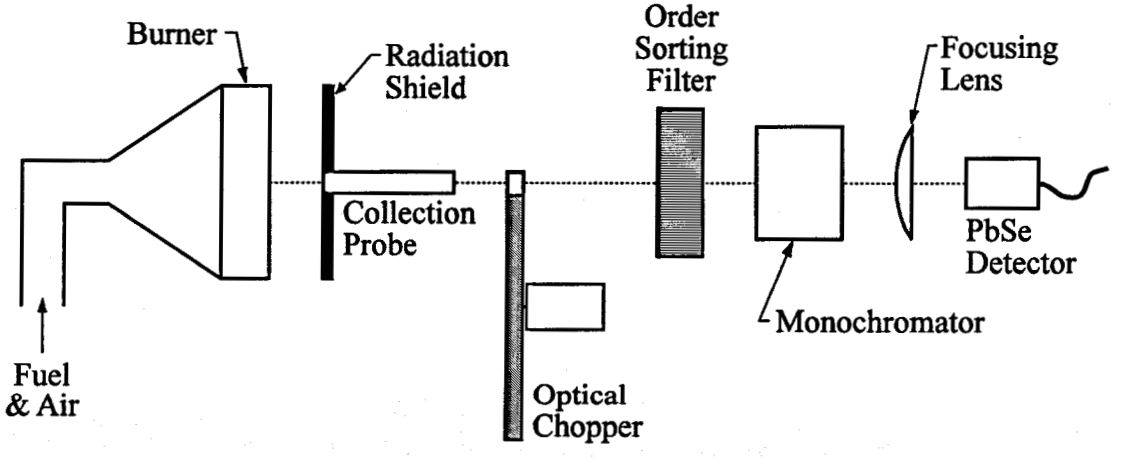

Figure 49 Schematic of the Spectral Intensity Measurement Apparatus

The spectral radiation intensity measurements for reticulated ceramic burners were made by replacing the blackbody with a reticulated ceramic burner. The burner was fired at various firing rates. For these firing rates, the voltage signal from the burner was collected in the wavelength range of 1 to 5 μm. Using the calibration constant, the voltage was then converted into intensities:

$$I_\lambda = V_\lambda / C_\lambda \tag{4}$$

Results and Discussion: Figure 50a is a plot of radiation efficiency versus the firing rate for the different ceramic and commercial burners at a fixed equivalence ratio of 0.9. For the metal and ceramic fiber burners, the flames stabilize very near the solid surface at low firing rates and transfer energy by convection to the solid which in turn radiates. The closer the flame (location of highest temperature) is to the solid surface, the higher the convective energy transfer due to a steeper temperature gradient at the surface. As the firing rate is increased, the flame must move away from

the surface to operate with lower heat transfer which leads to higher laminar burning velocity. This is based on the assumption that the level of preheat does not change with changes in firing rate. The above discussion applies since the flame never sinks into the porous surface of the material due to the large heat loss that will be encountered simultaneously with the initiation of such a movement. If the firing rates are increased beyond 300 kW/m^2, the adiabatic laminar flame speed is less than the mixture velocity and the flame can not be stabilized for the fiber burners.

For the reticulated ceramic burners, the flames stabilize inside the flame support layer. This results in a more efficient energy transfer by convection to the solid as compared to the energy transfer for a surface flame. This energy is in turn radiated by the solid resulting in higher radiant efficiencies for reticulated ceramic burners. The level of preheat of the mixture does not remain the same with firing rate in these burners. The preheat increases with firing rate which increases the laminar burning velocity and the flame can be stabilized for much higher firing rates. Firing rates above 630 kW/m^2 at an equivalence ratio of 0.9 for reticulated ceramic burners result in flashback unless the mixture velocity is increased by making the flame lean or the preheating is prevented by water cooling.

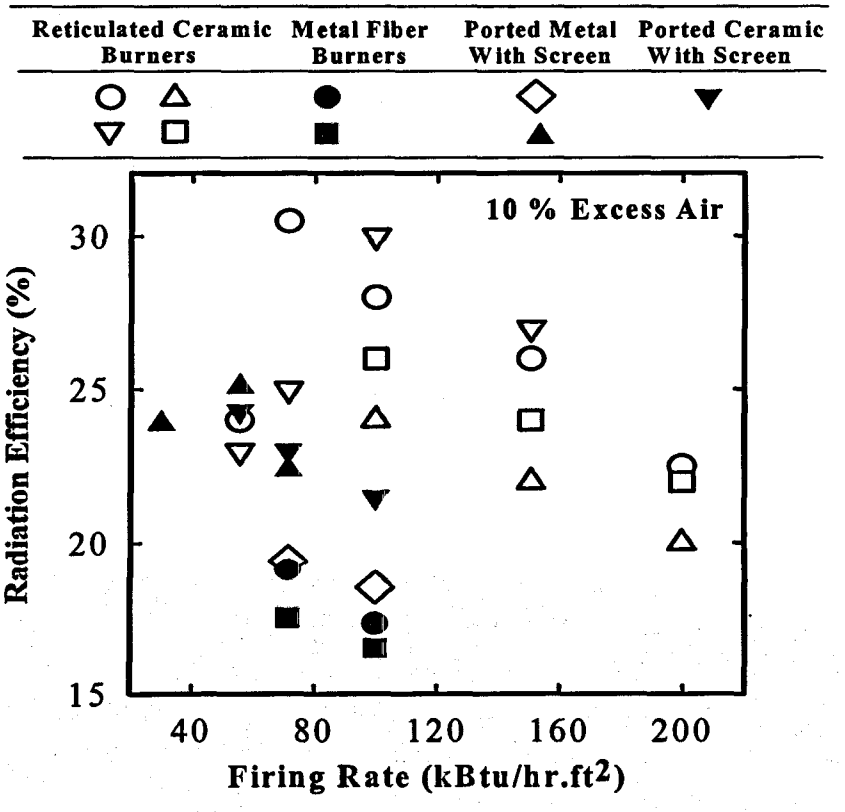

Figure 50a Radiation Efficiency vs. Firing Rate for Ceramic and Commercial Burners

Radiation efficiency results were qualified using the water calorimeter as mentioned earlier. Measurements of convective plus radiative efficiency and convective efficiency alone for a reticulated ceramic burner are shown Fig. 50b. The convective and radiative efficiencies are a function of the distance between the burner and the calorimeter due to air entrainment effects and view factors, respectively. The convective plus radiative efficiency of the cellular (reticulated) ceramic burners is around 65% for 236 kW/m^2 and 58% for 315 kW/m^2 firing rate at 2.5 cm distance.

These efficiencies are approximately 10% higher than those for the commercial burners for corresponding operating conditions. Below a gap of 2.5 cm, the heat transfer efficiency tends to become constant. The convective efficiency at 2.5 cm for 236 kW/m^2 and 315 kW/m^2 firing rates is 43% and 39% respectively. This gives uncorrected radiative efficiencies of 22% and 19% for the two firing rates. Estimates of corrections to the radiation efficiency measurements were obtained in the following manner: (1) The "black" calorimeter absorptivity is approximately 0.96. Correction for this value increases the convective plus radiative efficiency for the 315 kW/m^2 firing rate from 58% to 60%. (2) The reflection of radiation from the silver calorimeter back to the burner causes preheating of the incoming mixture and the exhaust gas temperatures increase by as much as 50 K (measured by Pt-Pt 13% Rh thermocouples) for the 315 kW/m^2 firing rate. This effect leads to a correction factor of approximately 1.05, which implies the convective efficiency is actually 37% instead of 39% for the 315 kW/m^2 firing rate. Taking into account these two effects, the radiation efficiency for the 315 kW/m^2 flame is 23%. (3) Reflectivity of silver for the present calorimeter is approximately 0.95. (4) The view factor between the burner and the calorimeter is 0.99 and hence it introduces only a small error in the radiative efficiency. Combining these two effects the corrected radiative efficiency is 24.5% for the 315 kW/m^2 firing rate. (5) The flame movement causes some uncertainty which is difficult to ascertain. However, it is clear that the calorimetric method qualifies the standardized imaginary cylindrical enclosure method results.

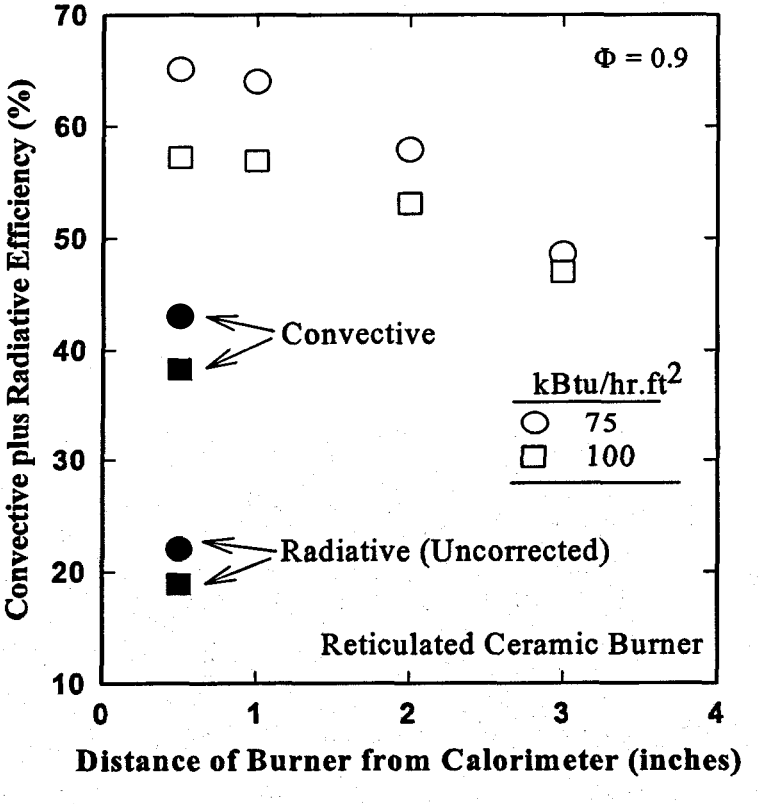

Figure 50b Radiative plus Convective Efficiency Results using Calorimeter

Important conclusions that may be drawn from Fig.506a are: a) The radiation efficiencies of the novel reticulated ceramic burners designed and investigated at AMPS, Inc. are 20 to 40 % higher than the efficiencies of all other present industrial burners; b) The firing rates of the present

industrial burners are limited to 300 kW/m^2 while the reticulated ceramic burners can be fired up to 600 kW/m^2 if operated within the stable range; and c) With a reliable design and characterization, the reticulated ceramic burners have the potential to be used for the Hybrid Electric Vehicle application.

Pollutant Emission: The pollutant emission results of representative industrial burner and reticulated ceramic burner are presented in Figs 51 through 54. The CO_2 emissions were measured to ensure that there was no entrainment of outside air in the chimney and to check the equivalence ratio of the mixture. It is clear from Fig. 51 that the HC emissions for the reticulated ceramic burner are much less than those for the metal fiber burner. However, from Figs. 42 and 43 it is obvious that the CO and NO_X emissions are generally less for the metal fiber and ported metal burners, compared to reticulated ceramic burner. Higher surface temperatures of ceramic burners yield higher radiation efficiency. However, the increased residence time in the high temperature zone of the flame support layer is also responsible for increased NO_X. Reticulated ceramic burners operate with a high level of preheat leading to more efficient HC consumption reactions. Those reactions may also be enhancing the prompt NO contributions leading to higher NO_X emission indices. The heat extraction from the products of the primary flame zone in a region where CO is normally oxidized leads to quenching of CO oxidation steps and higher CO emission indices. An interesting phenomenon is shown in Fig. 54, at lower firing rates (less than 300 kW/m^2), the CO emissions are higher for reticulated ceramic burners, but as the firing rate is increased CO emissions become comparable or even lower than those of the metal fiber burners. This decrease in CO and HC emissions at the higher firing rates for reticulated burners could be due to the increase in preheat resulting in higher gas phase temperatures and efficient combustion. Both CO and HC emissions decrease with decrease in equivalence ratio. NO_X emissions increase with increase in firing rate as well as with increase in equivalence ratio for both type of burners. At higher firing rates more energy is released per unit area resulting in higher gas temperatures leading to relatively higher NO_X emissions. The crucial point to note from these results is that these emissions are lower than the emission standards set by the EPA for the ULEV in the year 2004.

Stability Range: In the range of firing rates investigated (150 - 475 kW/m^2), the blowoff limit was generally between an equivalence ratio of 0.6 - 0.7. The lean limit was between 0.5 - 0.6 equivalence ratio. There was no flashback below 300 kW/m^2 for any of the ceramic burners; however, above this limit, the burners with thicker flame support layer showed flash back conditions. For burner 1 (Table 2), the flame did not flashback for any operating range and for higher equivalence ratios ($\phi > 1$) the flame came out of the burner and burnt as a rich flame. Metal fiber burner flames which are surface flames do not suffer from flashback problems. However, their upper range of firing rate is limited to 300 kW/m^2 due to material degradation.

Burner 1 (Table 2) was tested for its turn down ratio. This burner could operate in a stable radiant mode at $\phi = 0.9$ up to 473 kW/m^2; however, the practical upper firing rate of the burner is limited to 394 kW/m^2 due to material degradation problems. At 157 kW/m^2 the burner looks brightly radiant with non-uniformities that are characteristic of the flow distribution achieved by the commercial housing and the reticulated material. The radiation efficiency at this operating condition is 22.5%. At 126 kW/m^2, the nonuniformity increases a little and a dark cold spot starts to appear in a corner. At a firing rate of 79 kW/m^2 the burner becomes quite non-uniform and the radiation efficiency decreases to 18.5%. The lowest stable firing rate possible was 63 kW/m^2. Below this firing rate only a fluctuating blue flame could be obtained.

So effectively this burner has a 6:1 turn down ratio. It was also clear that nonuniform flow distribution determines the turn down ratio for the present designs. Nevertheless, it can be seen that the novel ceramic burners designed at AMPS, Inc. are capable of more than 4:1 turn down ratio required for the Hybrid Electric Vehicles.

Spectral Intensity: The results of the spectral intensity measurements are shown in Fig. 55 at an equivalence ratio of 0.9 (circles joined by dotted lines) for the firing rate of 393 kW/m^2. The two peaks around 2.7 μm and 4.3 μm are due to the H_2O and CO_2 emission bands, respectively. Using an effective emissivity of cordierite-LS2 as 0.65 and assuming gray body, Planck's distribution at a temperature is matched as closely as possible with the measured intensity data. The emissions due to the H_2O and CO_2 bands were omitted for this purpose and the data were joined by a smooth curve. This temperature is the effective surface temperature of the ceramic since part of the measured intensity is coming from inside the burner as well.

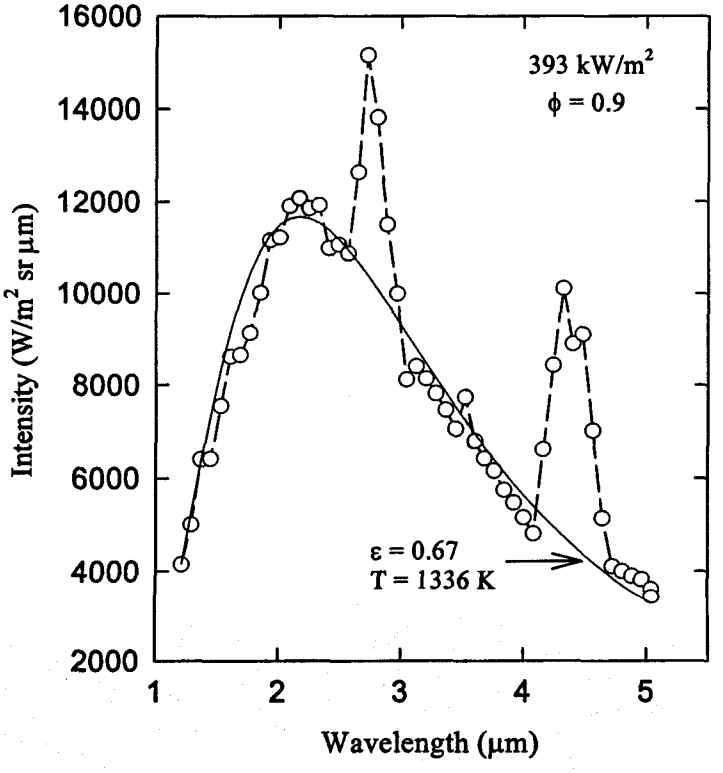

Figure 55 Variation of Spectral Intensity with Wavelength for the 4 ppc Ceramic Burner

The results obtained using the Planck distribution are tabulated in Table 4. These are compared to the surface temperature data obtained using thermocouples pasted to ceramic surface. The quantitative values of the surface temperatures should be interpreted with caution because of the unknown contact resistance between the bead and the surface. The experimental radiation efficiency is listed next along with the quantity ($\varepsilon\sigma T^4/Q$).

Table 4 Comparison of Spectral and Thermocouple Temperature Results

No.	Firing Rate Q (kW/m^2)	Surface Temperature, K (Spectral data)	Surface Temperature, K (Thermocouple)	Measured Radiation Efficiency (%)	$\varepsilon\sigma T^4/Q$ (%)
1	236	1255	1243	30	40
2	315	1289	1277	28	34
3	394	1336	1305	27	31

The surface temperatures by the two methods are consistent. The difference could be due to the fact that while the thermocouple measures the temperature at the point of attachment, the spectral data gives an effective surface temperature. These measurements also provide convincing evidence that the burner surface is hot enough to provide the required hot end AMTEC temperature of 800 °C. The quantity $\varepsilon\sigma T^4/Q$ is higher than the measured radiation efficiency because the burner surface nonuniformity (lower surface temperature near edges) is not taken into account in this expression.

Modeling of Reticulated Ceramic Burners

The high radiation efficiency, low pollutant emissions and 6:1 turn-down ratio of the reticulated ceramic burners was quite encouraging. It was decided to mathematically model these burners so that their design could be optimized for use with AMTEC cells specifically for the Hybrid Electric Vehicle application.

Combustion is stabilized inside the porous ceramic medium by adjusting the mass flow rate of the fuel-air mixture so that flashback or blow-off is prevented. The porous medium emits, absorbs and scatters thermal radiation to the surroundings. The radiative feedback upstream from the reaction zone to the unburned gas can increase the laminar flame speed creating high volumetric heat release rates and a high effective flame speed. On the other hand, due to heat transfer from the flame to the high surface area ceramic, the flame may loose more heat than it gains in the preheat region. The result then would be a lower flame temperature than the adiabatic flame temperature and lower flame speed than the free flame speed. The final state of the ceramic stabilized flame depends on the net balance between the heat gained in the preheat region and that lost in the flame zone.

Model Formulation: Ceramic stabilized flames can be mathematically modeled using separate gas and solid phase equations. Input mass flux, which determines the flame speed under steady state conditions is an input parameter while the flame location is an output of the model. The principal assumptions used in the mathematical model are as follows:

1. The physicochemical processes are one-dimensional (including radiative transfer), in the axial direction only.
2. The Dufour and Soret effects, viscous heat dissipation, bulk viscosity and body forces are negligible.
3. The burner operation is adiabatic, except for the radiant output.
4. The porous medium emits, absorbs and scatters thermal radiation as a gray homogeneous medium, but gaseous radiation is considered to be negligible in comparison with the solid radiation.
5. Potential catalytic effects of the high temperature solid are neglected.
6. The gas phase and the solid phase energy equations are coupled through a volumetric heat transfer coefficient.
7. The flame is one-dimensional and neither stretch nor turbulence are induced by the flow through the porous inert media.
8. The thermophysical properties of the gas and the solid matrix are functions of temperature.
9. The local gas and solid temperatures are not equal.

The energy equations for the gas and solid phases are :

$$\frac{\partial}{\partial t^*}\left(\rho_g^* c_p^* T_g^*\right)+\frac{\partial}{\partial x^*}\left(\rho_g^* u^* c_p^* T_g^*\right)=\frac{\partial}{\partial x^*}\left(\lambda_g^* \frac{\partial T_g^*}{\partial x^*}\right)-\alpha^*\left(T_g^*-T_s^*\right)+\Delta H_c^* S_{fg}^* \tag{5}$$

$$\frac{\partial}{\partial t^*}\left(\rho_s^* c_s^* T_s^*\right)=\frac{\partial}{\partial x^*}\left(\lambda_s^* \frac{\partial T_s^*}{\partial x^*}\right)+\alpha^*\left(T_g^*-T_s^*\right)-\frac{\partial q_r^*}{\partial x^*} \tag{6}$$

The conservation equation for the mass fraction of fuel is

$$\frac{\partial}{\partial t^*}\left(\rho_g^* m_f\right)+\frac{\partial}{\partial x^*}\left(\rho_g^* u^* m_f\right)=\frac{\partial}{\partial x^*}\left(D_{AB}^* \rho_g^* \frac{\partial m_f}{\partial x^*}\right)-S_{fg}^* \tag{7}$$

where

$$S_{fg}^* = ff^* \rho_g^{*2} m_f m_{o2} \exp\left(-E^* / R^* T_g^*\right).$$

The two-flux radiative transfer approximation needed to define the radiative heat flux divergence $\frac{dq_r^*}{dx^*}$ are

$$\frac{dq^{*+}}{dx^*} = -2(1-f\omega)\sigma_e^* q^{*+} + 2\omega b\sigma_e^* q^{*-} + 2n^2\sigma_e^*(1-\omega)\sigma T_s^{*4} \tag{8}$$

$$\frac{dq^{*-}}{dx^*} = 2(1-f\omega)\sigma_e^* q^{*-} - 2\omega b\sigma_e^* q^{*+} - 2n^2\sigma_e^*(1-\omega)\sigma T_s^{*4} \tag{9}$$

where the radiative heat flux is defined as

$$q_r^* = q^{*+} - q^{*-} \tag{10}$$

Using large activation energy asymptotic methods an analytical solution was derived for the gas and solid temperature profiles within the ceramic burner. A third order differential equation is obtained in such a case which is solved using the appropriate mathematical tools. Following assumptions, additional to those presented above, have been made in order to obtain an analytical solution:

1. Steady state conditions.
2. Internal radiation in the solid phase equation is neglected.
3. Solid matrix radiates at the downstream face only.
4. The thermophysical properties of the gas and the solid matrix are constant.

Under these assumptions, the three main governing equations, gas, solid and lean species (Equations 5, 6 and 7) may be non dimensionalized using adiabatic values of flame temperature and inlet velocity. Non dimensionalization of these equations identifies those parameters which characterize the operation of the burner. Using the following dimensionless quantities (without star (*) above them):

$$T_g = \frac{T_g^*}{T_{ad}^*}, \qquad u = \frac{u_{01}^*}{u_{ad}^*}, \qquad T_s = \frac{T_s^*}{T_{ad}^*},$$

$$x = x^* \frac{\left(\rho^* u_{ad}^* c_p^*\right)}{\lambda_o^*}, \qquad \alpha = \frac{\alpha^* \lambda_o^*}{c_p^{*2}\left(\rho^* u_{ad}^*\right)^2}, \qquad F = \frac{\lambda_o^*}{\lambda_s^*}$$

the dimensionless equations for gas, species and solid for premixed combustion in reticulated ceramic burners become:

$$u\frac{dT_g}{dx} - \frac{d^2T_g}{dx^2} + \alpha\left(T_g - T_s\right) = \Delta H_c S_{fg} \tag{11}$$

$$u\frac{dm_f}{dx} - \frac{d^2m_f}{dx^2} = -S_{fg} \tag{12}$$

$$\frac{d^2T_s}{dx^2} + \alpha F\left(T_g - T_s\right) = 0 \tag{13}$$

The asymptotic analysis essentially reduces the problem to finding the solution of three pairs of second-order coupled differential equations.

Results and Discussion: Equations 11, 12 and 13 are solved subject to the appropriate boundary conditions. To obtain an analytical solution the gas and solid properties are assumed constant; however, the values chosen are representative values for reticulated ceramic burners. The model requires the following set of parameters as input; activation energy, upstream temperature, porous solid width, conductivity ratio, heat transfer coefficient, emissivity, and surrounding temperature T_∞. The model then predicts the flame location for a given input mixture velocity. From a knowledge of the solid surface temperature, the radiant output is calculated using the emissivity and the Stefan Boltzmann law. This divided by the heat input gives the radiation efficiency. The following is a typical set of input parameters used to model the reticulated ceramic burners:

Activation Energy $\theta = \frac{E}{RT}\ \frac{175000}{8.314 \text{x} 2100} = 10$

Upstream Temperature $T_{01} = \frac{T_{01}^*}{T_{ad}^*} = \frac{850}{2100} = 0.4$

Porous Solid Width $w = w^* \frac{\left(\rho^* u_{ad}^* c_p^*\right)}{\lambda_o^*} = 0.003 \frac{\left(1.1 x 0.33 x 1248\right)}{0.106} = 12.8$

Based on data obtained from Hi-tech Ceramics, Inc. the Conductivity Ratio

$$F = \frac{\lambda_o^*}{\lambda_s^*} = \frac{0.106}{0.9} = 0.117$$

The model assumes constant thermal conductivities and internal radiation in the solid has not been considered.

Heat Transfer coefficient $\alpha = \frac{\alpha^* \lambda_o^*}{(c_p^*)^2 \left(\rho^* u_{ad}^*\right)^2} =$

$$\alpha = \frac{90{,}000 x 0.106}{(1248)^2 x \left(1.1 x 0.33\right)^2} = 0.046$$

Radiation coefficient $S_{ad} = \frac{\sigma^* \varepsilon T_{ad}^{*\,3}}{\rho^* u_{ad}^* c_p^*}, = \frac{5.67 \text{x} 10^{-8} \text{x} 0.65 \text{x} 2100^3}{1.1 \text{x} 0.33 \text{x} 1248} = 0.75$, where the effective emissivity, $\varepsilon = 0.65$

Surroundings Temperature $T_\infty = 0.2$

The predictions of the model are examined in the following. Figure 56 is a comparison of the predicted and the measured flame location for the 3 mm thick flame support layer burner for an equivalence ratio of 0.9. In the experiment, the lower firing rate limit is determined by lift off. This

is because, as the firing rate decreases, the heat loss fraction (ratio of heat transferred from the gas to the ceramic divided by heat input) increases. Hence, combustion cannot be sustained inside the ceramic and takes place more and more outside the surface until lift off occurs. With increase in firing rate the heat loss fraction decreases and flame moves upstream until due to high preheat effect the flame is no longer in the flame support layer and flashback is said to occur. There is a region in-between where the increase in convective velocity takes over the preheat effect and the flame moves downstream with increase in firing rate. The model predicts a similar trend of initial upstream motion followed by downstream motion and finally upstream motion of the flame with increase in firing rate resulting in flashback. The lower firing rate limit predicted by the model is 90 kW/m^2 while in the experiment it is 80 kW/m^2. Similarly, the higher firing rate limit predicted by the model is close to 630 kW/m^2 which is flashback limited. In the experiment the firing rate was limited to 630 kW/m^2 due to material degradation problems. Overall, the model shows reasonable accuracy in predicting the flame location.

Figure 57 is a comparison of measured and predicted radiation efficiencies for an equivalence ratio of 0.9. Qualitatively the trend is captured well by the model but quantitatively the efficiencies are over predicted by around 25%. The radiation efficiency results, however, match well with the values obtained using spectral intensity measurements. The difference between the model and the multipoint measurement could be attributed to burner nonuniformity and heat loss in the actual experiment.

Conclusions

After the extensive research with various flame support layer materials, it was concluded that the reticulated ceramic burners might be the most promising infrared burners for the Hybrid Electric Vehicles. The radiation efficiency results show that the reticulated ceramic burners can provide higher radiant output than the existing industrial burners and hence increase production in the manufacturing industry. This is possible due to the 20 - 40 % higher radiation efficiency of the reticulated ceramic burners at the lower firing rates and due to their capability to operate at higher firing rates with the same efficiency obtained in the existing industrial burners. Even with high heat transfer to the solid, the combustion in radiant burners is quite efficient. The HC emissions of the reticulated ceramic burners are lower while the CO emissions are comparable to the metal fiber burner emissions. The NO_X emissions are higher for the reticulated ceramic burners which may be attributed to a high contribution from the prompt NO mechanism. The emissions are still low enough for the burners to be environmentally safe. The HC and CO emissions decrease for the reticulated ceramic burners and increase for the metal fiber burners while the NO_X emissions increase for both burners with increase in firing rate. All emissions decrease with decrease in equivalence ratio.

The analytical model was successfully used in modeling the burner performance. It will prove to be a useful tool in determining the turn-down ratio, radiation efficiency and other parameters while optimizing the burner design for the Hybrid Electric Vehicle program.

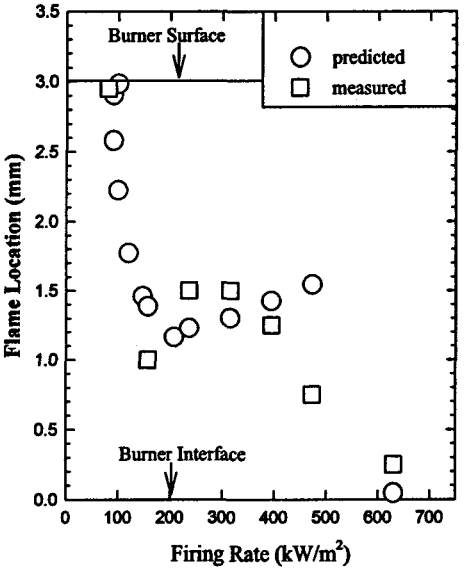

Figure 56 Measured vs. Predicted Flame Location

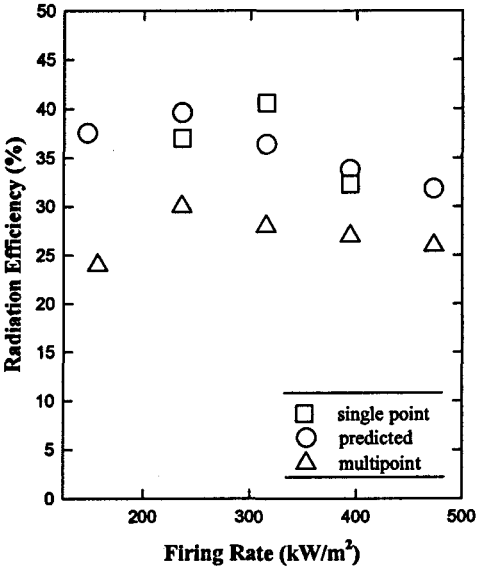

Figure 57 Measured vs. Predicted Radiation Efficiency

Recuperator System

The conceptual design of an "air to air" recuperator was carried out under this task. An analysis of plausible flow path configurations was made and a model was formulated to allow variations of the design to be investigated without requiring multiple hardware builds. The recuperator is a key element in this system. The thermal effectiveness must be high to minimize fuel consumption, and the pressure drop must be low to minimize the size of the air blower needed to circulate air through the unit. For the present proposal a recuperator core with optimal heat transfer and pressure drop performance was designed with the help of the models.

Various heat exchanger configurations and combinations thereof, such as, parallel flow, counter flow, tube in tube and shell and tube were modeled. The aim was to design a high effectiveness, low pressure drop and light weight recuperator. The overall heat transfer coefficient was determined in all cases and the design was checked using both the log mean temperature difference analysis and the effectiveness - NTU method. In the following results are presented of the heat exchanger analysis using the NTU method. The effectiveness, ε, is the ratio of the actual heat transfer rate for a heat exchanger to the maximum possible heat transfer rate.

$$\varepsilon = \frac{q}{q_{max}} \tag{14}$$

For any heat exchanger it can be shown that

$$\varepsilon = f\left(NTU, \frac{C_{min}}{C_{max}}\right) \tag{15}$$

where C_{min}/C_{max} is equal to C_c/C_h or C_h/C_c, depending on the relative magnitudes of the hot and cold fluid heat capacity rates. The number of transfer units (NTU) is a dimensionless parameter that is widely used for heat exchanger analysis and is defined as

$$NTU = \frac{UA}{C_{min}} \tag{16}$$

The system flow rates were based on a 4:1 turndown ratio. The breadboard is expected to be a 25 We power system. This implies exhaust flow rates varying between 0.054 g/s and 0.215 g/s for the lower and upper firing rate limits, respectively. Calculations for the present system for the required length of the heat exchanger for tube in tube configuration (parallel and counterflow) and shell and tube configuration were done using the model.

Shell and tube presents an attractive choice due to its effectiveness, manufacturing ease and low pressure drop on the shell side. Any desired effectiveness, limited only by heat loss, can be attained by the shell and tube arrangement by having a longer tube in the shell. Calculations for a counterflow shell and tube heat exchanger were also carried out using the models developed at AMPS. One design finally optimized using the model is as follows. The shell is 6 cm in diameter and the tube is 3.1 mm ($1/8^{th}$ inch) in diameter and is made of stainless steel. A one meter length of the tube in the form of a 4 cm diameter coil is inside the shell. There are eight rings in this coil and these are supported on baffles inside the shell. The baffles also serve to increase the convective heat transfer coefficient on the shell side of the heat exchanger. There coil is approximately 8 cm in length so the shell is around 10 cm long. The inlet and exit ports of the shell are 2 cm each to keep the pressure drop on the shell side low.

When heat capacity ratios of the cold and hot fluids are greater than zero and the number of transfer units is greater than 0.25, counterflow heat exchanger is most effective. Calculations based on a modest effectiveness of 0.5 showed that the fluid flowing through the required length of the tubing to bring about the heat exchange will encounter 0.1 psi pressure drop. After combustion the exhaust is close to atmospheric pressure and is basically a buoyancy driven flow. For the breadboard it was decided to use a counterflow heat exchanger whose design was optimized using the mathematical model and a code written using TK Solver software.

An alternate heat exchanger is also being considered for this program which is being investigated by Creare Inc. under a different program for AMPS. The details of this heat exchanger are given in the following.

Description of the Recuperator: Figure 58 shows a sketch of the proposed recuperator and two diagrams that illustrate the internal construction. The recuperator is a counterflow, parallel plate heat exchanger in which the intake air for the combustor warms by absorbing heat from the combustion exhaust gases. As shown in the figure, ambient air at a temperature of 150°C enters through header slots on the left-hand end of the heat exchanger. The air stream flows through alternate, parallel plate channels to the right, absorbs heat from the counter-flowing hot gases, and leaves directly from the right hand end of the recuperator. Hot combustion gases enter header slots on the right-hand end of the recuperator. The combustion gases flow to the left through the alternate set of flow channels and leave directly from the left-hand end of the heat exchanger.

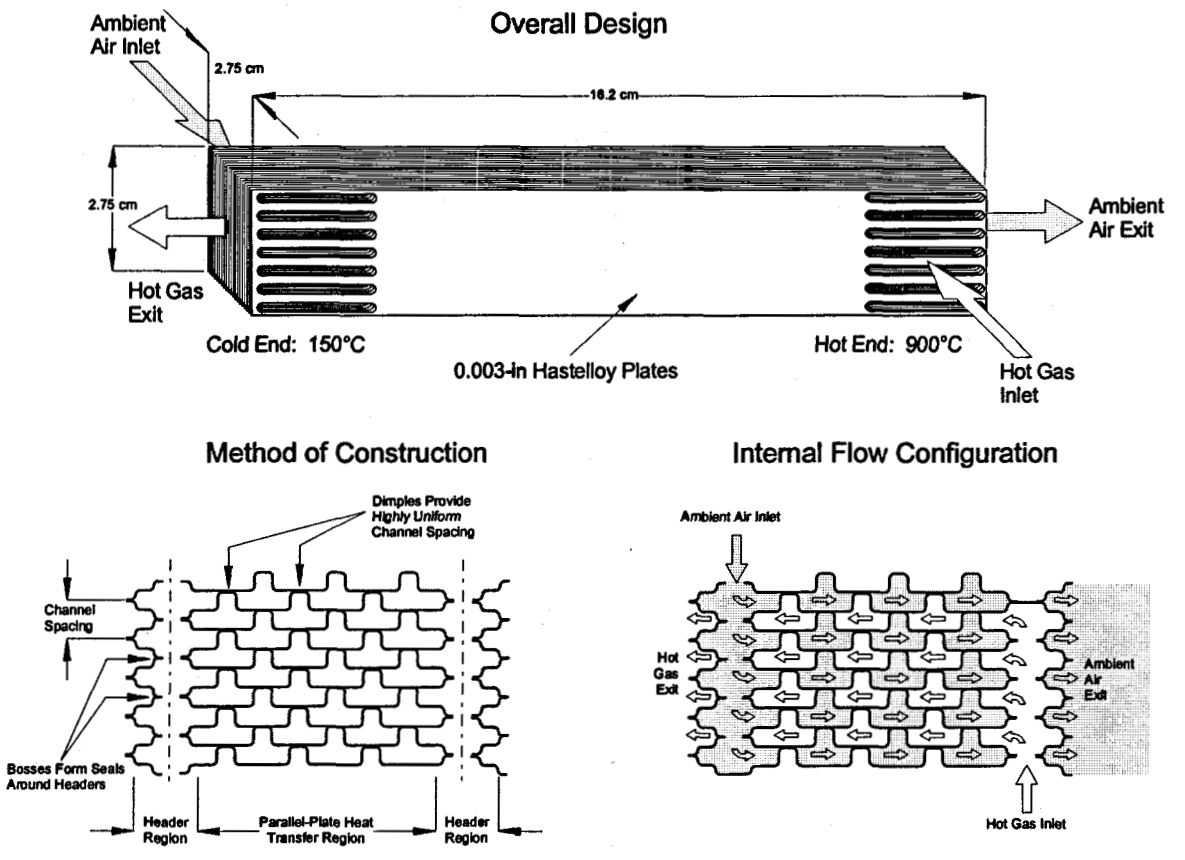

Figure 58. Parallel Plate, Laminar Flow Recuperator

The lower two sketches in Figure 14 show schematically how the recuperator is constructed. The left-hand sketch shows the basic design concept. Thin Hastelloy plates are stamped with an array of dimples and bosses. The dimples provide extremely uniform channel spacing (variation less than 0.5%), which is vital for achieving uniform flow and high thermal effectiveness. The bosses define the inlet headers for the two streams once the plates are stacked. The right-hand sketch shows the gas flow paths through the recuperator. Each gas stream enters through one of the headers formed by the bosses stamped in the plates. From the headers, the gas turns ninety degrees to flow through the counterflow parallel channels. Each stream exits by flowing around the other stream's inlet headers, then directly out the end of the recuperator.

Figure 59 is a photograph that illustrates precision-stamped Hastelloy plates that have been developed for heat exchangers used for thermal management on advanced fighter aircraft. The photograph illustrates the array of dimples used to maintain channel spacing as well as the bosses used to define the headers. Once stacked, the plates can be bonded and sealed by pressure, brazing, or electron-beam welding. For hybrid electric vehicle power system, the entire stack can easily be brazed together to provide adequate sealing performance. The heat exchanger is a primary surface design (no fins), because laminar flow between parallel plates provides the optimal ratio of heat transfer to pressure drop. The plate spacing and overall core dimensions can be selected to minimize the core mass within the following constraints:

- Pressure drop on each side is less than or equal to 100 Pa (0.40 inches of water),
- Total heat transfer area is sufficient to result in the desired thermal performance, and

- Minimal effectiveness penalty due to axial heat conduction.

Lower pressure drops are simple to obtain by increasing the flow area through the heat exchanger; the trade-off is that the mass of the core increases. Depending on how the blower size scales with the pressure loss, the heat exchanger design that is truly optimal for the system may call for a heavier heat exchanger with lower pressure losses.

The heat exchanger should have an overall thermal effectiveness of about 87%, resulting in a total heat transfer of nearly 90 Watts. Overall dimensions are roughly one inch wide, one inch deep, and four inches long. The heat exchanger core is very light-weight, with a mass of only 0.061 kg (0.13 lb_m).

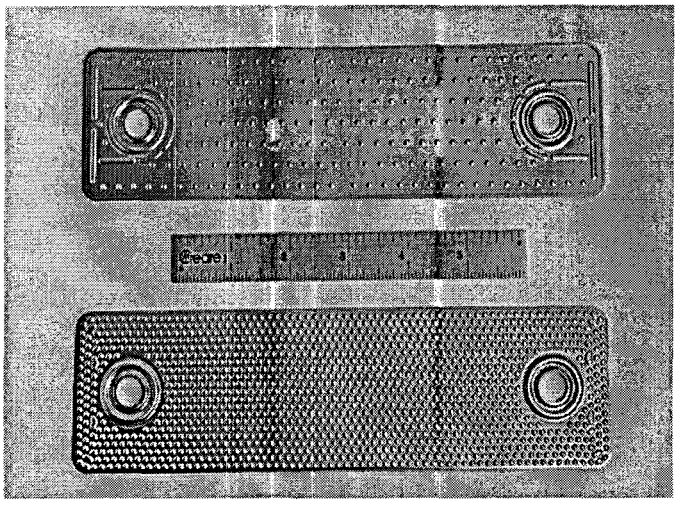

Figure 59a. Precision-Stamped Hastelloy Plates

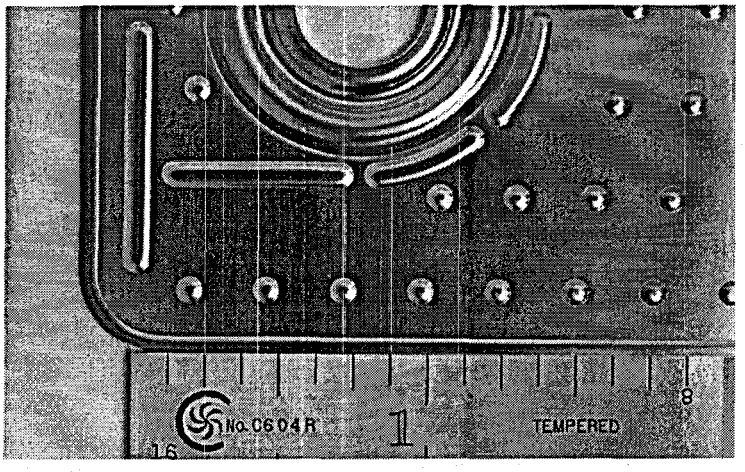

Figure 59b. Precision-Stamped Hastelloy Plates

Some sample calculations using the models developed at AMPS for the counterflow tube-in-tube heat exchanger are shown in figures 60 through 62. Figure 60 shows that as the effectiveness increases, the exit air temperature from the heat exchanger also increases linearly with it. For an effectiveness of 0.7 and a inner tube diameter of 3.1 mm the exit air temperature would be approximately 650 K. From the plot it is clear that auto ignition or flashback would not be a problem for this design even with 0.9 effectiveness of the heat exchanger. At 0.9 effectiveness, the exit air temperature is around

815 K. Figure 17 shows the penalty of high effectiveness in terms of increased pressure drop. For an effectiveness of 0.9 at a constant tube diameter of 3.1 mm the pressure drop is approximately 15 kPa.

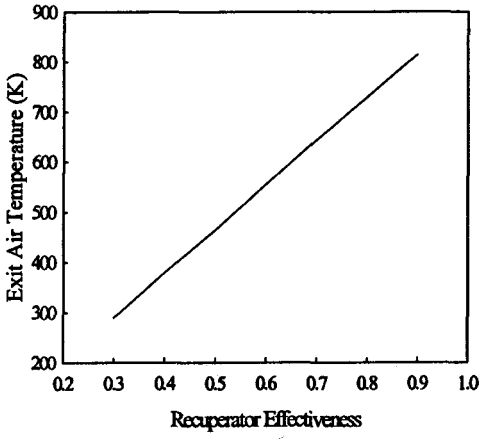

Figure 60 Exit Air Temperature vs. Recuperator Effectiveness

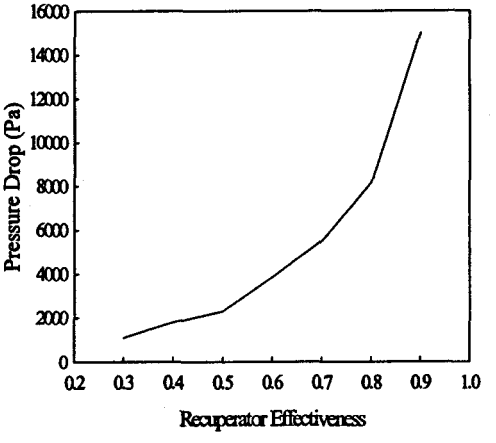

Figure 61 Pressure Drop vs. Recuperator Effectiveness

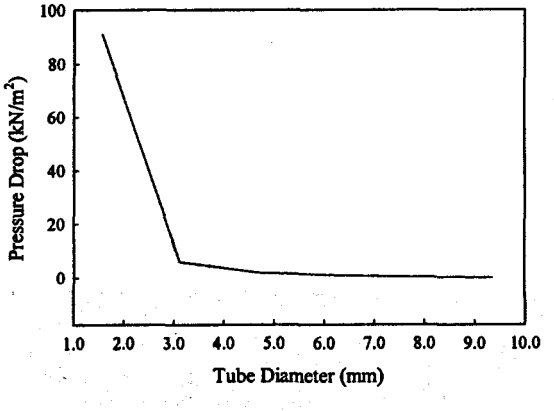

Figure 62 Pressure Drop vs. Heat Exchanger Tube Diameter

The increase in pressure drop with increased effectiveness is essentially due to an increase in the length of the heat exchanger tubes. Figure 18 shows decrease in pressure drop as the diameter of the inner heat exchanger tube is increased, this decrease however, comes at the cost of increased mass. Table 5 below lists some of the design parameters of the optimized heat exchanger having high effectiveness and low pressure drop.

Table 5. Design for Laminar Counterflow Recuperator

Specifications	
Flow rate of air (g/s)	0.20
Air Inlet temperature (°C)	150
Inlet temperature, hot gases (°C)	800
Design	
Material of construction	Stainless Steel
Configuration	Counterflow, tube-in-tube
Heat exchanger width (m)	0.250
Heat exchanger depth (m)	0.150
Number of coils	11
Predicted Performance	
Total heat transfer (W)	90
Overall thermal effectiveness (%)	0.85
Cold side exit temperature (°C)	795
Hot side exit temperature (°C)	200
Pressure drop (Pa)	500

Advantages of the Recuperator: The tube-in-tube counterflow recuperator offers major advantages for the hybrid electric vehicle systems:

- High thermal effectiveness: High thermal effectiveness in the recuperator minimizes the specific fuel consumption by efficiently utilizing the waste heat in the combustion gases.
- Low pressure drop: Low pressure losses minimize the size and power consumption needed for the system's air blower.
- Compact: The recuperator is simple to integrate with the burner and AMTEC cells.
- Low cost: Due to the simple design, the recuperators will be very inexpensive to manufacture.

Thus the recuperator will play a key role in proving the feasibility and boosting the performance of the breadboard test developed for the hybrid electric vehicle program. However, if further decrease in weight and size can be accomplished, from the other heat exchanger design under investigation, without loosing on performance in terms of effectiveness and pressure drop, the increase in overall system efficiency will make this

7. System Cost Issues and Estimates

Any realistic evaluation of a technology for automotive applications must place heavy effort on cost. We have carried out a cost analysis based on modular converters sized for power applications in the multi-kilowatt range. The BASE is the principal material cost element based on current manufacturing processes. The lowest and best full cost estimate published for sodium beta"-alumina ceramic was prepared by a group at Ceramatec some years ago[14]. The price arrived at in high volume production using isostatic pressing for green body formation and conventional sintering methods was approximately $0.03/cm^2. At a relatively high power density of 0.4 W/cm^2, this leads to a cost of $.075/watt or ~ $56/hp for this AMTEC converter cost element alone. Discussions with NGK Insulators Ltd. gave cost estimates of similar magnitude. NGK is currently the largest manufacturer of Na-BASE in the world, most of which they use in sodium sulfur batteries. In private discussions, they have told us that their current costs are approximately $40/tube for BASE tubes 5.9 cm OD x 48 cm long. This corresponds to a cost of $0.05/cm^2 and they have said they expect shortly to reach $15/tube of the same size which corresponds to ~ $0.02 w/cm^2. While these numbers are quite low for an electrochemical system, it is clear, that in the absence of very substantial improvements in the fabrication of BASE, AMTEC cannot compete on straight cost with conventional IC engines at equivalent peak power levels. For consideration as an element in a hybrid electric vehicle system, an extension of the cost analysis to full converter and system level is required. Such a complete analysis will require a specific and detailed system design which was beyond the scope of this program. Two independent system cost assessments have now been made by non-AMPS organizations. While the methods used differed somewhat, the result in each case was that complete fuel-fired AMTEC power systems could be built at a cost of ~ $1/ peak watt or ~ $746/hp using extensions of conventional AMTEC fabrication methods.

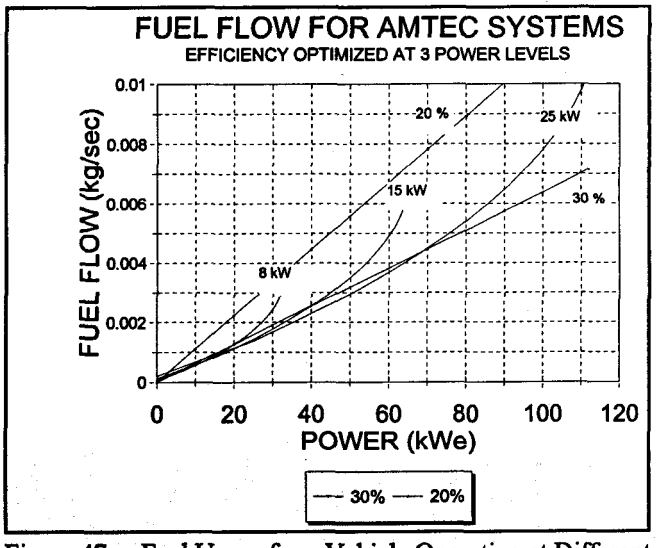

Figure 47 Fuel Usage for a Vehicle Operating at Different Power Levels Using AMTEC Systems of Different Rated Output.

Because of the high part load efficiency of AMTEC systems, a hybrid battery/AMTEC system can function with a substantially lower average power capability than could an IC engine with the same peak power capability. An AMTEC system of 15 kWe can provide the cruise capability for a mid-size vehicle at legal highway speeds. The large range of power deliverable by an AMTEC system at near peak efficiency is an important characteristic for a hybrid electric vehicle power system. The curves in Figure 47 are representative of a crude model of a simplified AMTEC system design each power level using 50 converter modules. The curves show the rate at which fuel flow increases as you take an AMTEC system beyond its power level as rated for maximum efficiency. At $1/watt[15], the initial cost of ~ $60K for the system rated for maximum efficiency

[14] " Production Economics - The Driving Force Behind the Development of Beta"-Alumina Ceramic Electrolytes" Miller, G.R., McEntire, B.J. .and Gordon, R.S., Proceedings of Conference on Processing of Metal and Ceramic Powders, AIME, Ed. R. M. German and K.W. Lay, (1981).

[15] Note that $1/watt, which is much higher than for typical vehicle engines, is an extremely aggressive goal for non-IC engine, small power systems as large (gigawatt) coal fired utility power systems are built at a comparable cost/watt.

at 15 kW is likely to be prohibitive except for very specific environments requiring the low emission, low noise, and the omni-fuel properties which AMTEC can provide. Note that the best of IC engines rated at 60 kW peak power and operating at partial loads of approximately 20 kW or less as in cruise mode, would operate at efficiencies of order 15%, substantially less than half that of the similarly peak power rated AMTEC unit. Coupled with the inherently low emission (particularly $_{Nox}$ and CO) capability of the external combustion driving the AMTEC this property would make a very environmentally power system.

Ford Analysis Not Completed

At the outset of the Phase II program, the leader of the Ford Research Staff hybrid electric vehicle program expressed interest in carrying out an analysis of the performance of the AMTEC system design that was the anticipated output of this program. The Ford HEV program utilizes a vehicle performance simulation computer program that uses the power system characteristics to predict the emission and fuel economy performance of a vehicle operating through the Federally mandated driving cycles using the specific power system. Unfortunately, the AMTEC design did not mature fully during the course of this program and the projected data could not be provided to Ford in time before the situation at Ford changed, due in part to retirements. As a result it did not prove possible to get a formal run of the AMTEC projected performance over the driving cycles.

8. Follow on Programs - Phase 3 Approach

The work carried out on this program has led not only to further government sponsored development efforts, primarily for lower power converters in the 20 We to 500 We power range, but to present commercial interest in power systems in the 3 kWe to 10 kWe size. AMPS has recently reached a license agreement for use of AMTEC as part of a complete system for a large (~ $10B annual) domestic market. This commercial, non-government, investment is funding development of methods for production of AMTEC systems at much lower cost than has been possible previously. Among the several cost reduction targets now under investigation are:

- Enhanced surface area BASE to reduce interfacial impedance and increase power density
- The MSRI process for K-BASE to enable higher power density at lower temperatures.
- A novel cathode deposition process that avoids high vacuum sputtering techniques but offers the possibility of higher power density and longer life at high performance because it is a mixed conductor (of both AM ions and electrons).
- Novel methods for producing purely mechanical seals between the BASE elements and metal converter components thereby eliminating a vacuum or inert atmosphere brazing process and several parts.

9. Conclusions

The research program whose results are described in this report has shown that there are significant advantages which can be achieved if AMTEC systems can be made cost effective for vehicle applications. Notable among these advantages are: 1) the ability to operate with external combustion so as to readily minimize emissions of nitrogen oxides; 2) the large turn down ratio that combustion heated AMTEC generator systems can provide, thereby enabling hybrid vehicle operation with minimal battery storage complement (batteries sized to handle regenerative braking only); 3) the ability to operate on a wide range of fuels using appropriate burner system technologies. The primary issues remaining to be demonstrated are compact scaled up generator systems including burner/recuperator systems operable with liquid fuels and the cost reductions that will be required for acceptance by customers. Lifetime issues which are paramount for spacecraft and many other terrestrial applications are much less critical for vehicle applications for which maintenance-free operating lifetimes of 20,000 hours are often sufficient. Earlier generation AMTEC cells have operated for nearly this long and current generation cells on test have already shown lifetimes greater

than 14,000 hours. There is a strong expectation that these as well as improved converter designs will exceed vehicle life requirements by a substantial margin.

General Approach The majority of the overall funding for AMTEC has been associated with aerospace applications for NASA and the Air Force for which device cost tolerance is high. As a result cost reduction developments have not been considered critical and have not been funded by these agencies. Commercial applications, quite generally, require much lower cost for viability and in the automotive field cost is a primary consideration. As indicated in previous sections of this report, cost reduction developments are now underway, with the work primarily financed by commercial interests. The current cost of space qualified AMTEC systems is approaching $1,000/watt while costs less than $1/watt will be required for large non-vehicular terrestrial markets and costs below $0.25/watt will probably be required for vehicular markets.

Development of AMTEC technologies for space, terrestrial military and commercial applications is proceeding at AMPS and at several other organizations. A major result of the technical progress of the work conducted under this program is the increasing commercial interest in AMTEC technology evidenced, in part by the sale of a market specified commercial license to a domestic corporation and in part by a growing interest in AMTEC for residential cogeneration markets by companies based in the Netherlands and in Sweden. The current interest in these areas would not have occurred without the advances made during this program.

10. Appendix A Potassium BASE Experiment Paper

Potassium AMTEC Cell Performance

A. Barkan, T.K. Hunt and B. Thomas
Advanced Modular Power Systems, Inc.
4370 Varsity Drive, Ann Arbor, MI 48108

ABSTRACT

AMTEC systems have historically been operated with sodium as the working fluid, in large part because fabrication of beta"-alumina solid electrolyte (BASE) membranes has been substantially easier with sodium than with potassium or other alkali metals[16]. It has been anticipated that because potassium has a substantially higher vapor pressure for a given temperature, and because the best K-BASE conductivity falls only marginally below that for Na-BASE, potassium AMTEC cells could produce higher power at a given temperature or comparable power at a lower temperature than similar sodium cells. Operation at lower temperatures can reduce materials lifetime or compatibility problems, and for severely heat input constrained systems it could enhance efficiency by reducing parasitic thermal conduction losses. Recently K-BASE tubes have become available as a commercial product[17] and conventional experiments to evaluate the performance of complete K-AMTEC cells have become much more feasible. Previous experiments on K-BASE have focused primarily on measurements in non-power producing cell environments. One AMTEC cell experiment was carried out at low temperature.[18] We report here initial experiments on the power output performance of K-BASE with a conventional TiN cathode in a standardized single-pass AMTEC test cell. The performance data are compared to tests of Na-BASE cells under similar conditions and with similar electrodes. Peak power for a 6 cm^2 TiN electrode on a K-BASE cell was substantially higher than has been observed for the best, comparable Na-BASE cells. The power improvement corresponded to that for a temperature increase of ~ 60 K for the Na-BASE cell.

INTRODUCTION

Alkali Metal Thermal to Electric Converter (AMTEC) cells operate as thermally regenerative concentration cells using heat to drive alkali metal ions through an ionically conducting electrolyte membrane, typically a sodium beta"-alumina solid electrolyte (Na-BASE) using sodium as the working fluid. The open circuit voltage generated in such a cell can be described in its simplest form by the well known Nernst equation:

---

[16] 'Lithium AMTEC with Gas-Diffusion Cathode', G.P. Lysenko, Proceedings of the 31st Intersociety Energy Conversion Engineering Conference, p 890, (1996). 'High Temperature Conductivity of Potassium Beta"-Alumina," R.M. Williams, B. Jeffries-Nakamura, M.L. Underwood, M.A. Ryan, D. O'Connor and S. Kikkert, Solid State Ionics, 53-56, 806-810 (1992).

[17] K-BASE electrolytes can be purchased from Ionotec, Ltd. 14 Berkeley Court, Manor Park, Runcorn, Cheshire WA71TQ, England

[18] 'Potassium β"-Alumina/Potassium/Molybdenum Electrochemical Cells', R.M. Williams, A. Kisor, M.A. Ryan, B. Jeffries-Nakamura, S. Kikkert and D.E. O'Connor, Proceedings of the 29th Intersociety Energy Conversion Engineering Conference, pp 888-893, (1994).

'Time Dependence of the High Temperature Conductivity of Sodium and Potassium β"-Alumina Ceramics in Alkali Metal Vapor', R.M. Williams, A. Kisor and M.A. Ryan, J. Electrochem. Soc. **142**, 4257 (1995).

$$V = R(T / F)\ln[\frac{Pv(Th)}{Pv(Tc)}]$$

where R is the gas constant, F is Faraday's constant, and $P_v(T)$ is the vapor pressure of the working fluid at the hot side or cold side temperature.

The parasitic heat losses in AMTEC systems are strongly dependent on the difference between the hot and cold side temperatures. Operation at lower hot side temperatures can reduce both thermal conduction and radiation transfer losses and if power levels can be maintained at the lower temperatures, efficiency can be improved. Use of potassium with its higher vapor pressure can provide a higher voltage and power level for a given temperature heat source relative to a sodium-based system. In the normal operating temperature range for AMTEC cells, the vapor pressure of potassium is equivalent to that of sodium at a temperature approximately 120 K lower. This offers the designer the opportunity to operate a K-BASE AMTEC system at lower temperatures for the same voltage output or to get higher voltages at a given temperature than would be possible with a sodium based system.

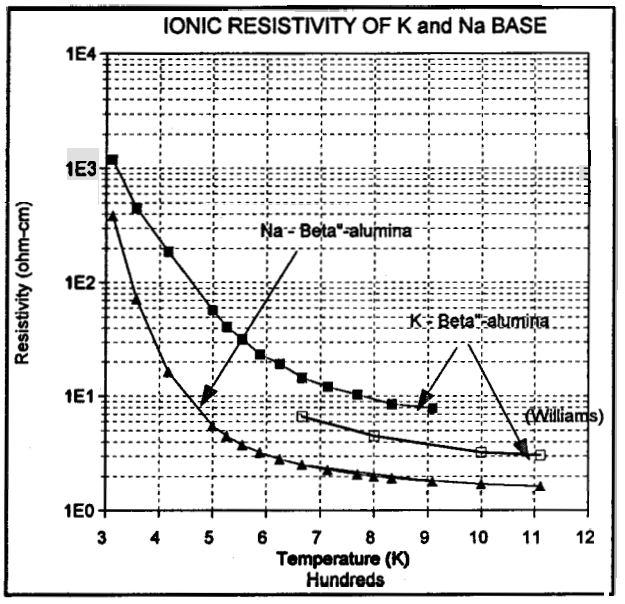

Resistivities

Sodium

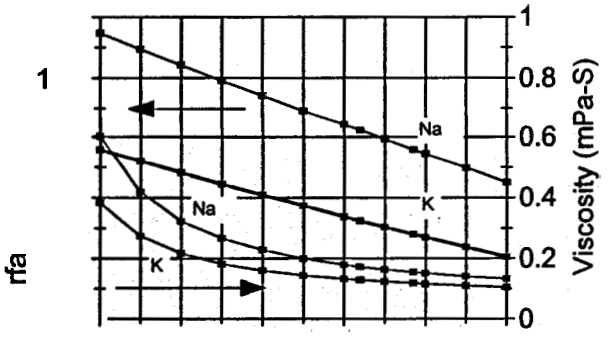

We expect that cells designed for high performance with potassium will require additional care with the working fluid return components.

K-BASE ceramic fabrication has generally been carried out by exchanging potassium ions for the sodium in standard Na-BASE material. Direct fabrication of potassium beta"-alumina ceramic via the normal sintering process used for Na-BASE is made extremely difficult because of the high vapor pressure of K_2O at sintering temperatures. Ion exchange of potassium for sodium in Na-BASE is feasible, but for polycrystalline material, it is necessary to carry out the exchange at temperatures high enough to permit annealing of the lattice to accommodate the C-axis expansion without causing fracturing as crystallites expanding along one axis impinge on crystallites expanding in other directions. This property was used to determine the ultimate strength of beta"-alumina ceramics by introducing known amounts of potassium at low temperatures and observing the fractional exchange required to trigger the onset of fracturing[21]. Early K-BASE samples were prepared by Crosbie and Tennenhouse[22] using KCl vapor at about 1413 K. Recent work by Williams et al at the Jet Propulsion Laboratory has produced K-BASE material with both better strength and ionic conductivity and included the first test of an AMTEC cell using potassium as the working fluid at a temperature of ~ 450 C. The present work uses K-BASE material that has recently become commercially available and the experiments were carried out over a typical range of AMTEC operating temperatures from 820K to 1073 K.

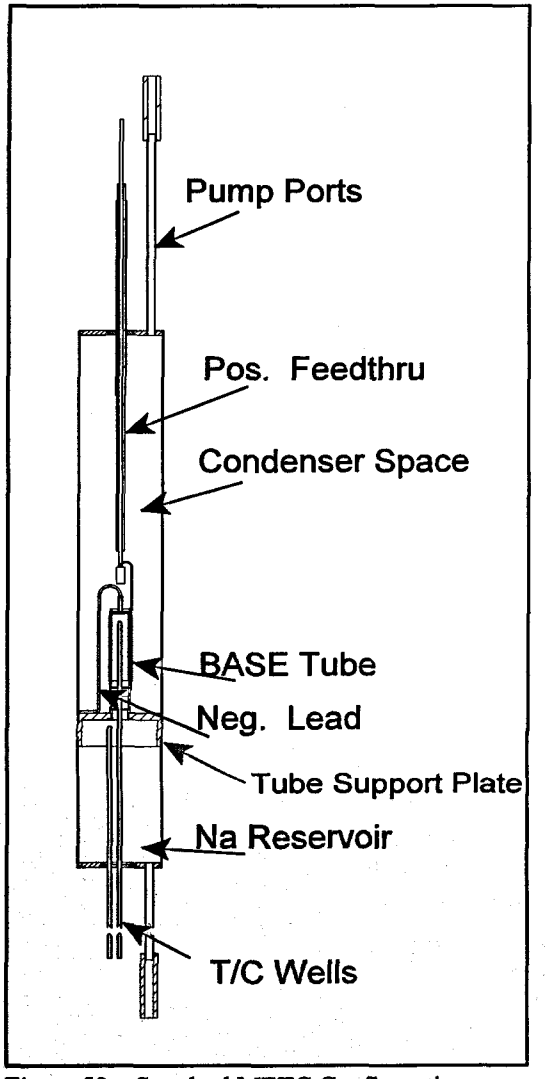

Figure 50 Standard METC Configuration.

EXPERIMENTAL APPROACH

Over the past 2 years we have fabricated and operated over 85 mini-electrode test cells (METC's)[23] investigating a variety of electrodes and current collector configurations. METC's are single pass, non-recirculated AMTEC cells which can be operated either in a vapor anode mode with the evaporator temperature (and hence hot side vapor pressure) controlled independently of the electrolyte temperature or in liquid anode conditions over a wide temperature range. The general arrangement for these cells is shown in Figure 3.

In a typical experiment, a single BASE tube, complete with electrodes, standard current collector and bus systems, and the alkali metal reservoir are heated independently and as the temperatures of reservoir and BASE are raised while maintaining the BASE at a high enough temperature to prevent alkali metal condensation, current-voltage curves are traced rapidly from open circuit to short circuit conditions. A series of runs at escalating temperatures are recorded using a digital data acquisition system based on LabView™ software, and the cell is then inverted, filling the BASE

[21] Unpublished work carried out by J.T. Kummer, communicated to the authors, 1992.

[22] G. Crosbie and G. Tennenhouse, J. Amer. Ceram. Soc., 65, 187, (1982).

[23] 'Electrode Testing in Simple Vapor-Vapor AMTEC Cells', T.K. Hunt, C.A. Borkowski, K.F. Childs , R.K. Sievers, Proceedings of the 32nd Intersociety Energy Conversion Engineering Conference, p. 1196, (1997).

tube with the liquid alkali metal for a series of liquid anode runs over a similar temperature range. At any set of conditions, it is also possible to carry through a suite of A.C. impedance measurements to elucidate the various contributions to the internal impedance of the cell. These measurements are carried out at AMPS using an E,G &G Potentiostat Model 263A system with a Model 1025 frequency response detector.

K-BASE AMTEC DEVELOPMENT

AMTEC cells that use potassium (K) instead of sodium may have important advantages for some specific applications, and perhaps quite generally. With potassium's higher vapor pressure, a cell using K should, all other aspects being equal and at the same temperature, have a higher voltage than a cell using sodium. If the ionic resistivity of K-BASE is only moderately higher than Na-BASE and/or the ionic resistivity is not a major limiting factor for a given cell design, a K-cell should be able to operate either with the same power at a lower hot side temperature, or at increased power at the same hot side temperature. It is also possible that one may be able to make long term use of the enhanced molybdenum electrodes that perform, initially, so well in sodium cells. It has been shown that in sodium cells, oxides on the surfaces of a sputtered molybdenum electrode react, in the presence of sodium metal during cell operation, to form sodium molybdate, Na_2MoO_4, and other non-stoichiometric compounds that serve to conduct both Na^+ ions and electrons[24]. The extended electrode/electrolyte interface this affords and the ready transport of Na ions through the cathode when these compounds are present has been shown to lead to nearly perfect electrode performance. Unfortunately the Mo/Na/oxygen compounds evaporate readily at normal AMTEC operating temperatures of 1000 K to1200 K and the excellent performance doesn't last.

It is anticipated that with potassium the situation may be much longer lived. The potentially lower K-cell operating temperature should allow for longer life at a given performance level and there is reason to believe that the analogous K/Mo/oxygen compounds will have much lower vapor pressures than those of the sodium variety. Thus a K-cell with molybdenum cathodes may have both high performance and adequately long life for many applications. The experiments described here were chosen to begin the investigation of this possibility.

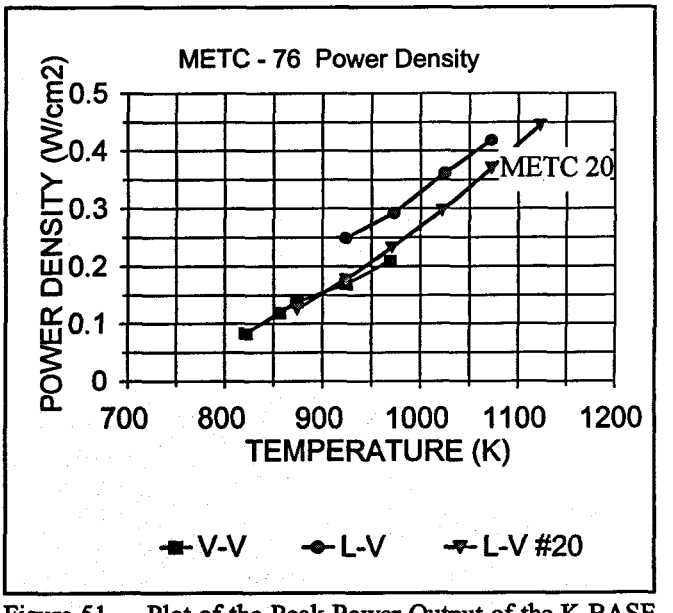

Figure 51 Plot of the Peak Power Output of the K-BASE Cell and Comparison with METC-20, the Highest Power of the Na METC's.

An METC (#76) with an Ionotec K-BASE tube and a 4 gram load of potassium was run through a range of temperatures in both liquid and vapor anode conditions to see if its performance would be reasonably in accord with expectations based on K-BASE data from Williams et al[3] and to verify that we could successfully load and operate a cell with this new material. To this end we used a standard TiN electrode deposited under standard conditions in AMPS' reactive sputtering apparatus onto the outer surface of a 7.6 mm O.D. x 3 cm long x 0.5 mm wall thickness, K-BASE tube supplied by Ionotec.

[24] 'The Role of Oxygen in Porous Molybdenum Electrodes for the Alkali Metal Thermoelectric Converter', R.M. Williams, G. Nagasubramanian, S.K. Khanna, C.P. Bankston, A.P. Thakoor, and T. Cole, Journal of the Electrochemical Society, 133, 1587-1595, (1986). Schmatz, D.J., (1989) 'Molybdenum Oxide Electrodes for Thermoelectric Generators', U.S. Patent 4,847,171 assigned to the Ford Motor Company, Dearborn, MI.

A continuous wrap of 0.0125cm diameter Mo wire is used for the outer current collector (OCC) without an interposing Mo wire mesh screen between the wire and the BASE. In this approach the Mo wire is wrapped tightly, with no space between turns, around and along the entire length of the electrode. This appears to provide an adequate contact density while reducing fabrication time, effort, and cost compared to conventional processing which uses a screen wrapped on with a secondary wrap to capture the main current bus. A conventional titanium nitride 'Weber'[25] electrode was used for the anode.

THE EXPERIMENTS

The experimental results were very good as can be seen in Figure 4. At 1073 K, in the liquid anode mode, this potassium cell produced the highest power level seen in any of the eighty plus Na based METC cells tested at that temperature. In general, the power output was that appropriate for the best Na METC cells tested thus far, but the power was achieved for the potassium cell at a temperature about 50 K lower than for the sodium cells. In Figure 4 it can be seen that the liquid anode performance of the K-BASE cell is substantially higher at 1073 K, than that of METC-20, which had the best Na-based METC performance we have seen to date. The K-BASE cell resistance was also quite low indicating that for these cells, the ionic resistance of the K-BASE is not the critical factor limiting output power. The effective internal resistance of this cell, as measured by the slope of the I-V curve at high current, was somewhat higher than that of METC-20 as shown in Figure 5. The improved performance, in spite of the higher internal resistance tends to confirm that the increased vapor pressure is the major cause of the better performance.

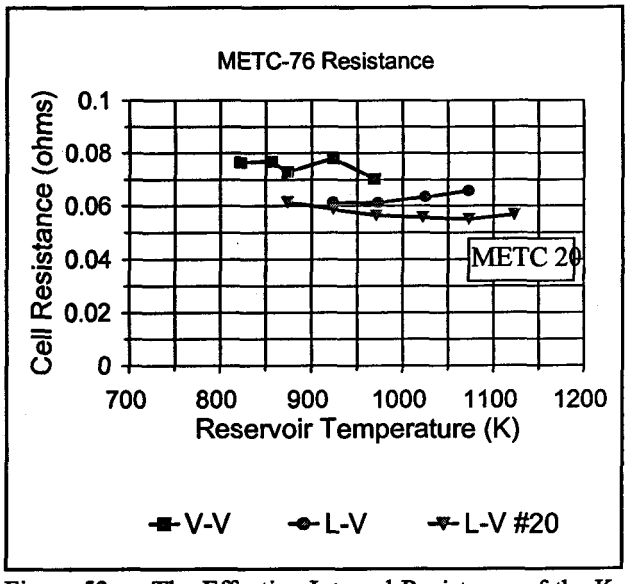

Figure 52 The Effective Internal Resistance of the K-BASE Cell and a Comparison with a Very Good Na-BASE Cell.

Note that the internal impedance of this cell is still very low suggesting that the ionic resistivity of the K-BASE used here may be nearly comparable to that of Na-BASE. Additional testing will be required to justify this conclusion.

Based on the simple D.C. current-voltage data collection, the initial high temperature K-BASE AMTEC cell experiment appears to confirm the expectations for improved power output and the ability to operate at lower temperatures using standard titanium nitride electrodes and BASE tube assembly techniques. As discussed above, preliminary experiments were also carried out on

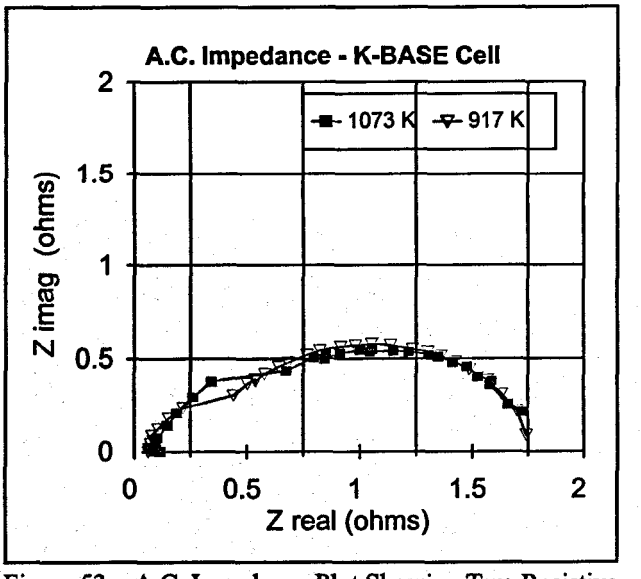

Figure 53 A.C. Impedance Plot Showing Two Resistive Elements, Tentatively the Intrinsic and Contact Resistances.

[25] Weber, N., (1993) "Method of Making Nitride and Oxide Electrodes on a Solid Electrolyte", U.S. Patent # 5,209,945, assigned to Beta Power, Inc. Salt Lake City, Utah. E1

this cell using the E,G&G, A.C. impedance apparatus to collect data on interfacial polarization, contact resistance etc. The measured real and imaginary impedance components at 917 K and 1073 K for this cell are shown in Figure 6. The separation of the two semi-circles at the two temperatures shown in this plot does not appear to be unique, but the intercepts do appear to be consistent with the D.C. results.

Additional experiments to examine the performance of K-BASE cells with sputtered molybdenum cathodes are underway. These will involve two other METC experiments, the first with Na-BASE will serve as a check of the sputtered electrode properties using current processes and will establish a baseline power level to be expected with the Mo electrode. The second, which will incorporate a K-BASE tube with the same electrode parameters, may be expected to show power output exceeding both the Na-BASE and the K-BASE cell with the TiN electrode described here. While potassium molybdate will be a solid at normal AMTEC operating temperatures up to ~ 1185 K, it is expected that the mixed ionic/electronic conductivity of this compound will provide enhanced electrode performance for K-BASE cells as the analogous compound has been shown to do, in the liquid state, above ~ 925 K, for Na-BASE cells.

ACKNOWLEDGMENTS

The authors wish to thank K. Childs, K. Yeum and AMPS' cell fabrication team for their work to prepare these experiments. The work was supported with internal AMPS funding.

'Hydrogen Permeation Issue for Gas Fired AMTEC Systems', R. Mital, D.A. Butkiewicz, K.F. Childs, D.D. Hayes, R.C. Svedberg and T.K. Hunt, Proceedings of the 34th Intersociety Energy Conversion Engineering Conference, # 2557, (1999).

Hydrogen Permeation Issue for Gas Fired AMTEC Systems

R. Mital, D.A. Butkiewicz, K.F. Childs, D.D. Hayes, R.C. Svedberg, and T.K. Hunt
Advanced Modular Power Systems, Inc.

ABSTRACT

Diffusion of hydrogen in solids is an intriguing intellectual problem. Permeation of hydrogen generated in combustion into gas fired Alkali Metal Thermal to Electric Converter (AMTEC) systems can be detrimental to AMTEC performance for various reasons. Potential effects include depriming of the AMTEC cell arteries, blockage of the condenser and hydride formation. Numerous papers and reports have been published concerning hydrogen diffusion in solids (Birnbaum and Wert, 1972; Garber, 1975; Strehlow and Savage, 1974). Many of these papers concern the embrittling effects of hydrogen and many concern the diffusion process itself. Hydrogen permeation and permeation resisting strategies have been examined extensively in connection with other energy conversion technologies such as Stirling engines (Alger, 1988; Khalili et al., 1989) and high temperature heat pipes (Anderson et al., 1995; North and Anderson, 1997).

Due to the different boundary conditions and materials involved, it was necessary to conduct experiments specifically designed for AMTEC to evaluate hydrogen permeation rates into AMTEC cells, to understand the effect of this permeation on AMTEC performance and finally, if hydrogen permeation turns out to be a cause for concern, to identify strategies to reduce permeation, and to design an AMTEC cell which will perform with adequate lifetime.

This paper describes experiments and their results for AMTEC cells operated in a partial pressure of hydrogen. Experiments in which the hydrogen permeation rate across different thickness cell walls were measured with and without barrier coatings are also described. Due to greater sensitivity, the change in pressure on the vacuum side of the specimen was observed as hydrogen permeated the metal.

Depending on the operating conditions and the operating life requirements of specific AMTEC systems, hydrogen permeation barriers may need to be included in the cell design. Some of the solution approaches that were implemented and their effectiveness in minimizing AMTEC degradation are also elucidated.

INTRODUCTION

AMTEC technology has come a long way in the last 3-4 years. The cells, which are the building blocks of power systems, have gone from 2% efficiency (heat input to electric power output) to 20% efficiency and with the improvements that are in process are expected to exceed 25% efficiency. AMPS Inc. has developed a way to put this elegant, and highly efficient process into small modular packages that operate independently, without the need for peripheral devices to support the conversion process.

TECHNOLOGY DESCRIPTION

The Alkali Metal Thermal to Electric Converter (AMTEC) cell has a very simple energy conversion process (Weber, 1974). AMTEC is a thermally regenerative concentration cell utilizing sodium as the working fluid and sodium beta"-alumina solid electrolyte (BASE) as the ion selective membrane through which a nearly isothermal expansion of sodium can generate high current/low voltage power at high efficiency. The general principles of AMTEC operation can be illustrated using Figure 1 which shows two chambers separated by a BASE "membrane". Beginning in the heated, high pressure zone to the right side of the BASE, the alkali metal (AM) (sodium in the figure) ionizes, enters, and passes through the BASE.

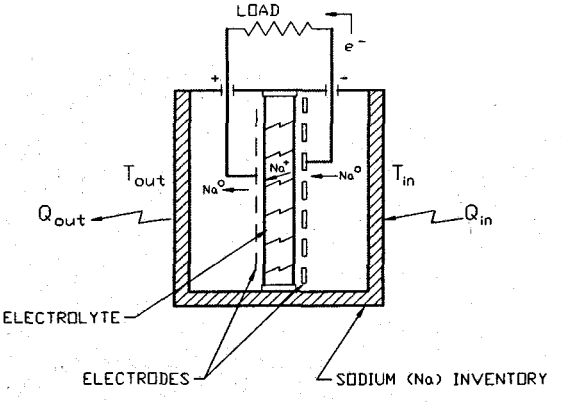

Figure 1. Operational Schematic of the Cell

The freed electrons pass from the anode (high pressure electrode) out to the electrical load and back to the cathode (on the low pressure side) where they recombine with the ions emerging at the BASE surface. The neutral AM then evaporates into the low pressure zone, condenses on the cooled inner surface of the chamber and is returned to the hot zone by a capillary structure (shown as a hashed layer) to complete the

cycle. Evaporator and condenser temperatures ranging from 900 - 1100 K and 500 - 650 K, respectively, are typical.

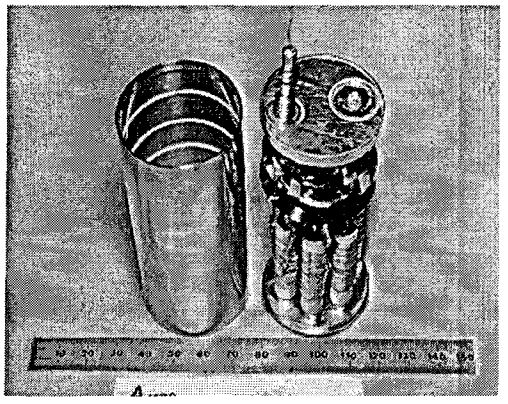

Figure 2. Multi-tube AMTEC Cell

TECHNOLOGY STATUS

Since AMTEC is inherently a high current, low voltage device, AMPS' designs connect BASE tubes in series to obtain voltages which match the intended application. This approach also packs more electrolyte surface area in the same volume, improving power density and efficiency. A typical small multi-tube AMTEC cell (Series II) is shown in Figure 2. When heat at 800°C is applied to the bottom end and the cell cooled at the top end, this cell is capable of producing 6 - 7 We. Recent advances in AMTEC cell design have led to greatly simplified assembly and operating procedures and enhanced durability (Sievers et al., 1997). Presently, gas-fired AMTEC power systems are being built in the range of 20 - 1000 W. Estimates have also been made for multi-kilowatt AMTEC systems. However, hydrogen permeation into the AMTEC cells through the cell walls has proved to be a deterrent to making long lasting efficient gas fired AMTEC systems.

PROBLEM DESCRIPTION

Hydrogen permeation may be a cause of concern for the AMTEC cells. Hydrogen permeation rates through thin (0.10" – 0.028") stainless steel were calculated using a pressure gradient corresponding to the partial pressure of hydrogen in the flame and correlations from different authors (Strehlow and Savage, 1974; Birnbaum and Wert, 1972). In all cases the rates were high enough to cause problems to a Series II AMTEC cell in the long run. The hydrogen molecule does not diffuse in metals directly; hydrogen diffuses in as monatomic atoms. Since there is monatomic hydrogen also available from reaction mechanism of flame, this compounds the problem.

The possible mechanisms in which hydrogen can harm the cell are:

- Hydrogen may form gas bubbles, and deprime the return artery.
- Hydrogen permeating into the cell can block a large portion of the condenser.
- Hydrides may form in the cell wick.
- Hydrogen permeation can increase the pressure on the low pressure side of the cell.

As a first step, it was necessary to quantify the extent of hydrogen diffusion for AMTEC cells. Existing data on hydrogen permeation, though useful as a guideline, is not directly applicable since most of the research effort on this topic is an outcome of nuclear systems or heat pipes or Stirling engines (North and Anderson, 1997; Anderson et al., 1995; Khalili et al., 1989; Alger et al., 1988). All of these applications required hydrogen containment at high pressures (orders of MPa). In our case the partial pressure of hydrogen in the flame is not expected to be more than 400 Pa.

EXPERIMENT DESCRIPTION

Three experiments were conducted in the present study, Experiment (A) was to measure hydrogen permeation through SS under AMTEC test conditions, Experiment (B) was to evaluate AMTEC degradation (if any) in a hydrogen environment and Experiment (C) was to test effect of wall thickness, coatings and getters on permeation rate.

EXPERIMENT (A)

A mock cell of the same dimensions as an average series II AMTEC cell (4" long, 1.5" diameter and 0.028" wall) was used for the testing. The cell was connected to a turbo pump and a Quadrupole mass spectrometer gas analyzer as shown in Figure 3. Thermocouples are installed on the cell wall, support plate and the cold end. The mass spectrometer ionizes, separates and detects the ions to provide intensities associated with different mass numbers. The derivation of quantitative data from this data requires calibration. The system is calibrated using a calibrated helium leak. The Amperes of current measured by the RGA at the mass unit corresponding to helium are equated to the flow rate of helium in atm-cc/s. Then, using the sensitivity ratio of hydrogen and helium, the Channeltron reading of mass spectrometer for hydrogen in Amperes is converted to permeation rate of hydrogen in atm-cc/s.

The equation used is as follows:

$$\frac{AmpsHe}{He(cc/s)} = f\frac{(AmpsH_2)}{H_2(cc/s)} \qquad (1)$$

where f is the sensitivity ratio and is equal to (1/2.03). Using this equation, the measured $AmpsH_2$ can be converted to permeation rate of H_2 in *cc/s*.

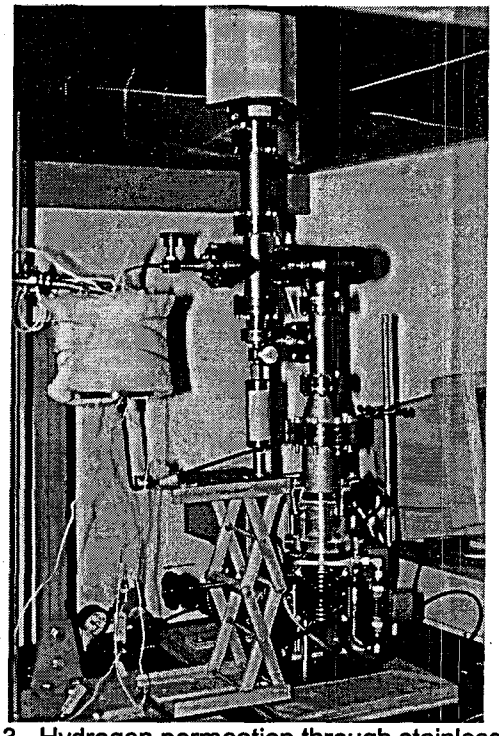

Figure 3. Hydrogen permeation through stainless steel

Test Procedure

Prior to the hydrogen testing, the test cell was heated to a cell wall temperature of 750°C in a 10^{-6} torr scale vacuum for more than a week. The ionic intensities of all the residual gases were monitored until each was less than 10^{-7} Amps. This bake out basically ensured that the hydrogen ion intensity with zero pressure gradient did not increase over time and hence the residual gas generation within the test volume will have no effect on the hydrogen permeability measurements.

The mock cell was then exposed to a propane flame with different amounts of excess air. The steady state temperatures of the cell wall, support plate and the cold end were recorded in each case. The mass spectrometer data was collected using Quadstar software. Peak intensity associated with hydrogen mass number was also recorded in each case. After completing the flame exposure test, the test cell was heated again electrically to the same cell wall temperature as obtained in the burner experiment to obtain the background hydrogen intensity value. Subtraction of the background value eliminates the effect of residual gas generation from the hydrogen permeability results.

To obtain the partial pressure of H and H_2 in the flame, use was made of the STANJAN code. STANJAN finds the equilibrium state for a system consisting of one or more phases. The gas phase is treated as a mixture of ideal gases, and condensed phases are treated as ideal solutions. Specific heats are temperature-dependent. The method of element potentials is used to find the state of minimum Gibbs function for the system, subject to the atom population constraints, treating the phases as either ideal gas or ideal solutions.

EXPERIMENT (B)

There was some speculation as to the accuracy of Experiment (A) since the calibration was done using a Helium leak and the predicted degradation times after data analysis seemed faster than had been actually observed in gas fired AMTEC systems. So an experiment was designed to measure AMTEC degradation in a controlled hydrogen environment.

Test Procedure

A Series II AMTEC cell was placed inside an enclosure. Using feedthroughs the cell performance was monitored continuously with and without a partial pressure of hydrogen inside the enclosure. The hot end temperature was 750°C, cell wall was 650°C and the condenser was about 300°C. The hydrogen flow was impinging on the insulation of the cell wall about 1 inch below the hot end. This was to simulate the hydrogen environment with a flame heated cell as realistically as possible.

Based on the flow rates, under steady state conditions, the hydrogen partial pressure inside the enclosure was 400 Pa. This represents the worst case scenario for flame heated cells (0% excess air and adiabatic flame temperature) so the degradation rates that may be observed in this experiment would be faster than those that would be observed in an actual test.

EXPERIMENT (C)

The objective of experiment (C) was to evaluate the effect of thickness, coatings and getter on hydrogen permeation rate.

Test Procedure

Mock cells with coatings and getters were tested in a hydrogen environment and the pressure rise over time was monitored for the different cells.

Three mock cells, as shown in Figure 4, were placed in a sealed SS chamber and hooked up to the ion gauge and turbo pump. Two sets of experiments were conducted. In the first experiment three stainless steel mock cells with 0.028" wall thickness were used. One of the cells was Nitrided (inside and outside), the second cell had five St 707 (SAES Inc., Colorado Springs, CO) pellets of about 0.5 grams each and the third cell was for baseline data. The getter pellets were sandwiched between two strips of SS shim stock which were tack welded together to prevent the pellets from falling out. This pellet "belt" was rolled to the inside diameter of the cell and tacked to the inside surface of the cell wall towards the cold end.

In the second experiment three stainless steel mock cells were used. The first had 0.028" thick cell wall and

the second cell had 0.065" thick cell wall. These cells were for baseline data. The third cell had 0.065" thick cell wall with aluminide coating (outside only).

For both experiments the system was baked out first. The pressure rise over time was monitored without hydrogen flow to obtain background pressure rise. The pressure rise over time was monitored with hydrogen flow. The background pressure rise was subtracted from the total pressure rise to obtain the net pressure rise due to hydrogen permeation.

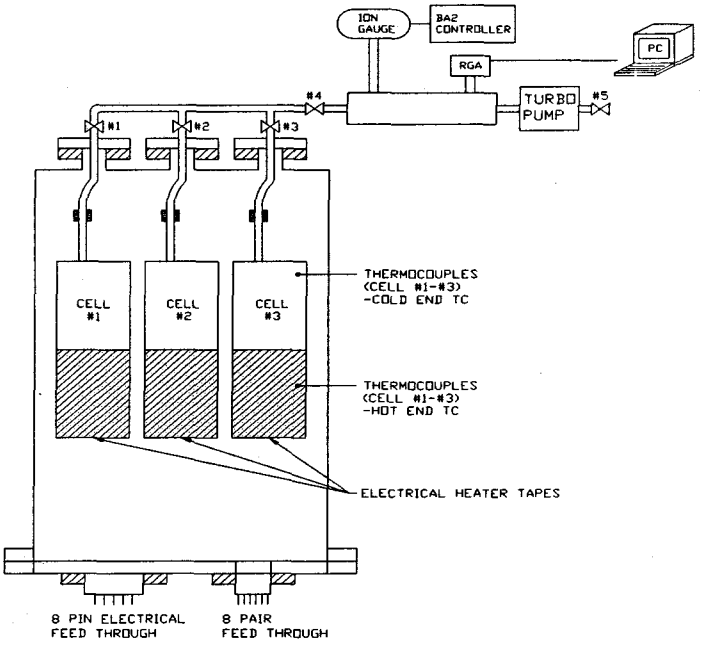

Figure 4. Experimental Arrangement to Evaluate Effectiveness of Coatings and Getters

RESULTS AND DISCUSSION

EXPERIMENT (A)

The results of STANJAN are given in Table 1. For a given excess air, the third column gives the flame temperature. The equilibrium mole fractions of H and H_2 are listed in the second to last column and the last column gives the partial pressure of hydrogen outside the mock AMTEC cell. Under equilibrium conditions the partial pressure of hydrogen on the low pressure side cannot be higher than this value.

Table 2 lists the temperature of the thermocouples installed on the mock cell for different excess air conditions and the permeation rate calculated based on Equation (1). The background value of H_2 intensity ($8.45*10^{-8}$ Amps) has been subtracted when doing this calculation. It is hard to compare these results with data available in the literature due to the differences in the experimental arrangement and test conditions. The closest data given in Table 3 was found in the paper by Strehlow and Savage, 1974. In the present mock cell the surface area though which hydrogen may permeate is 144 cm^2 and assuming the partial pressure of hydrogen outside the AMTEC cell is 1.0 torr (133 Pa, which is the partial pressure at 10% excess air, Table 1), the correlations in Table 3 gives the permeation rate as $1.8 * 10^{-5}$ cc/s. This result is an order of magnitude lower than the results obtained in the present experiment (Table 2) which could be partly due to the difference in sample thickness. Nevertheless, the comparison provides some level of confidence to the results of the present work.

From the various correlations available in the literature it is obvious that the permeation rate is exponential with temperature. Therefore, the hydrogen permeation rate into the hot end of the cell is much larger than the permeation rate out of the cell from the cold end allowing the accumulation of hydrogen near the condenser side. Since it is not clearly understood what happens to the hydrogen that permeates into the cell, model calculations were done under various assumptions. The assumptions common to all models are:

1. Hydride formation is neglected.
2. Hydrogen does not form a bubble and deprime the artery.
3. Hydrogen which permeates into the hot side is immediately swept to the cold side.
4. The temperature and pressure on the cold side is 623 K and 20 Pa, respectively.
5. The total cell volume is about 115 cc, out of which the volume of the low pressure side is 100 cc.

Model I

One possible scenario is that the hydrogen simply collects on the cold side and blocks the condenser surface reducing the efficiency of the converter. Specific assumptions to this model are:

1. The partial pressure of hydrogen in the plenum on the hot side is zero.
2. The partial pressure of hydrogen inside on the cold side cannot exceed the partial pressure of hydrogen on the outside of the cell.
3. The permeation rate of hydrogen out of the cell from the cold side is negligible.

Under these assumptions the moles permeating into the cell per second, the corresponding increase in pressure on the low side, the total pressure on the low side (including sodium pressure) under steady conditions, and the volume occupied by hydrogen on the low pressure side are all listed in Table 4. The results indicate that the permeation rate is very high and the equilibrium condition is reached with in a matter of minutes. However, with 40 or 50% excess air, only a marginal drop in performance of the cell may be expected.

It is also to be noted that some of the assumptions, such as, the diffusion rate out of the cell is negligible,

hydrogen pressure on the hot side is zero etc., make these calculations conservative. In reality the time to achieve equilibrium condition may be much longer. It could be hours, may even be days, but finally for no excess air or very low excess air conditions it is obvious that AMTEC performance will decrease unless preventive measures are taken. It is also possible that the hydrogen collecting on the condenser side besides increasing the low side pressure, blocks the path of sodium from reaching the condenser felt. This may eventually make the return artery dysfunctional and result in an evaporator dry out.

The other possibility is that the dissolved hydrogen flows with the sodium through the artery, comes to the high pressure side of the cell, sodium ions leave across the BASE tube while hydrogen collects inside the BASE tubes. The volume inside the Beta tube is 1.45 cc approximately. Assuming the hydrogen collects inside the BASE tubes at the Na vapor pressure (about 7 psi at 800°C) Table 5 gives the time required to fill up the six Beta tubes of a Series II cell under this condition. All through this period the active electrode area on the Beta tubes will be decreasing, resulting in degradation of the cell performance over time.

Model II

Table 1. Amount of Hydrogen in Flue Gases in Relation to Air/Fuel (C_3H_8) Ratio

No.	Excess air (%)	Flame Temperature (K)	Chemical Formula	Mole Fraction	Partial Pressure $P_{(H+H2)}$, Pa
1	0	2268	H H_2	0.00047 0.00334	386.5
2	10	2191	H H_2	0.00018 0.00112	132.3
3	20	2093	H H_2	0.00006 0.00041	47.9
4	30	1995	H H_2	0.000019 0.00016	18.2
5	40	1905	H H_2	0.000006 0.000065	7.3
6	50	1822	H H_2	0.0000022 0.000027	3.0

Table 2. Mock Cell Temperatures, Hydrogen Intensity and Permeation Rates

No.	Excess Air (%)	BASE (°C)	Wall (°C)	Cold (°C)	H_2 Intensity (Amps)	H_2 Permeation (cc/s)
1	0	811	508	310	$7.81*10^{-6}$	$5.05*10^{-4}$
2	10	807	504	312	$7.64*10^{-6}$	$4.94*10^{-4}$
3	20	803	501	309	$6.85*10^{-6}$	$4.42*10^{-4}$
4	30	791	494	305	$5.18*10^{-6}$	$3.33*10^{-4}$
5	40	784	488	297	$9.87*10^{-7}$	$5.90*10^{-5}$
6	50	776	481	291	$6.89*10^{-7}$	$3.95*10^{-5}$

Table 3. Available data in Reference [4]

Material	Temp (°C)	Permeation Rate1 torr, 1 mm thick [cc(STP)/hr-cm^2]	Pressure Range (torr)	No. of Observations
304 SS (oxidized)	785	$(4.5\pm0.5) \times 10^{-4}$	0.05 - 31.4	9

Table 4. Effect of Excess Air on Total Low Side Pressure

No.	Excess Air (%)	Permeation (moles/s)	Pressure Rise (Pa/s)	Total Low Side Pressure (Pa)	Cold Side Volume Occupied by H_2 (%)
1	0	$2.06*10^{-8}$	1.07	406.5	95.0
2	10	$2.02*10^{-8}$	1.05	152.3	86.6
3	20	$1.81*10^{-8}$	0.937	67.9	70.5
4	30	$1.36*10^{-8}$	0.706	38.2	47.6
5	40	$2.41*10^{-9}$	0.125	27.3	26.7
6	50	$1.62*10^{-9}$	0.084	23.0	13.0

Table 5. Effect of Excess Air on Time Required to Fill Beta Tubes with Hydrogen

No.	Excess Air (%)	Permeation (moles/s)	Time (min.)
1	0	$2.06*10^{-8}$	37.7
2	10	$2.02*10^{-8}$	38.5
3	20	$1.81*10^{-8}$	43.0
4	30	$1.36*10^{-8}$	57.1
5	40	$2.41*10^{-9}$	322.8
6	50	$1.62*10^{-9}$	481.9

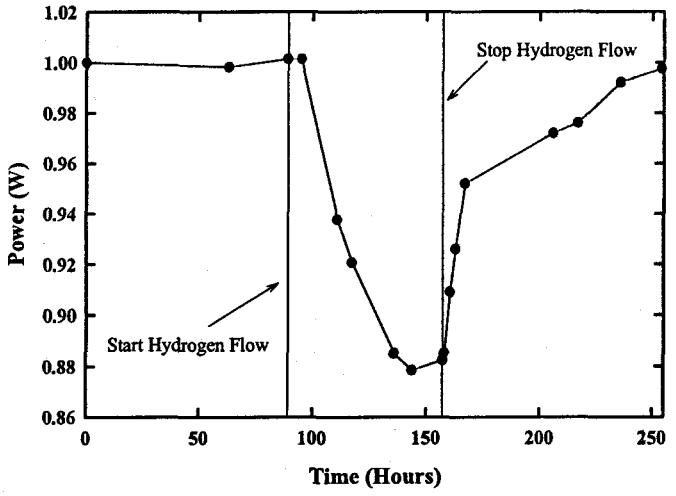

Figure 5. Effect of Hydrogen on AMTEC Cell Performance

EXPERIMENT (B)

The normalized power of the GASTEC 4 cell is plotted vs. time (hours) to show the effect of hydrogen permeation on the cell performance. The power has been normalized by the steady state power of the cell to clearly see the percent change in performance over time. The effect of hydrogen permeation is not seen immediately. The 1% hydrogen in nitrogen flow rate was about 1 cc/s. The chamber volume in which the cell was placed had a volume of about 16,000 cc. Hence there was a time lag between the start of hydrogen flow and start of cell degradation.

As can be seen from Figure 5, the cell power dropped by about 12% during approximately 60 hours of operation with hydrogen flow. The cell has recovered to about 98% of original power during the last 60 hours of operation with the hydrogen flow shut off. This experiment conclusively proved that hydrogen permeation is detrimental to AMTEC cell performance and a solution strategy needs to be developed to overcome this problem.

There are number of possible options by which we can reduce permeation, though, for most of these options the mechanism by which the penetration is suppressed is not well understood. It may involve one or all of several factors: inhibition of hydrogen dissociation, low solubility and low diffusion constant. *Possible options of reducing hydrogen permeation include:*

1. Prevent the hydrogen from entering the cell with a hydrogen-permeation resistant barrier,
2. Modify the operating conditions to minimize hydrogen permeation,
3. Develop a method to rapidly vent or getter any hydrogen that permeates into the cell.

Alumina, Beryllium oxide, Aluminum oxide are possible coatings to reduce permeation rate. Another possible option is use of a porous layer of powder metal placed between two containment walls. The large surface area allows recombination to form molecular hydrogen which is subsequently vented to space. Use of a condenser with gas pockets is another option. The structure can be a single closed end annular cavity formed by an inner tube and an annular ring which closes the end of the annulus toward the evaporator. Hydrogen can be trapped in the cavity.

EXPERIMENT (C)

The effect of wall thickness, coatings and getters was evaluated in this experiment. The results are summarized in Table 6 and Figure 6. Column 1 in Table 6 gives the cell wall temperature in K. Permeation rate for the baseline 0.028" thick wall cell is given in column 2. Permeation rate for the baseline 0.065" thick wall cell is given in column 3. The permeation rate with getter for the 0.028" cell is given in column 4. The getter was very effective at the low permeation rates and as a consequence no pressure rise was observed due to hydrogen permeation. The permeation rate for the 0.065" aluminide coated cell is given in column 5. The aluminide coating reduced the permeation from the baseline value by a factor of about 3 as given in column 6.

Table 6. Effectiveness of Coatings and Getter Against Hydrogen Permeation

Temperature (K)	Hydrogen Permeation Rate (cc/s)				
	0.028" Wall	0.065" Wall	0.028" with Getter	0.065" with A	Coating Reduction
923	7.4×10^{-6}	3.2×10^{-6}	2.3×10^{-7}	8.1×10^{-7}	3.9
773	3.7×10^{-6}	1.6×10^{-6}	no rise in pressure	5.2×10^{-7}	3.0
573	2.6×10^{-7}	1.2×10^{-7}	no rise in pressure	5.0×10^{-8}	2.4

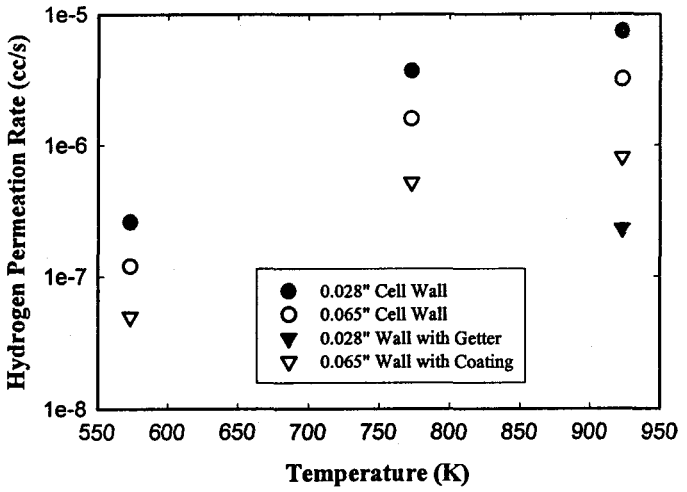

Figure 6. Hydrogen Permeation Rate vs. Temperature

CONCLUSION

The permeation rate seems to be asymptoting to a maximum of approximately 1 x 10^{-5} cc/s for the 0.028" stainless steel cell wall.

Based on the assumption Ti getter will eat H_2 mole for mole, at a permeation rate of 1 x 10^{-5} cc/s, 2.5 grams of Ti getter will last for about 3.5 years.

Maximum accumulation of hydrogen recommended by SAES for St 707 is 20 torr l/g. Accumulation of hydrogen in excess of 20 torr l/g, can lead to embrittlement and particulation due to the change of the lattice parameters. Based on this assumption, 2.5 grams of St 707 getter can last 70 days for the permeation rate of 1 x 10^{-5} cc/s. If embrittlement is not a concern, hydrogen can be sorbed at concentrations higher than 100 torr l/g which means a getter life of more than a year.

Column 5 in Table 6 lists the permeation rate with Aluminide coating. The coating reduces the permeation rate by a factor of at least 3 (column 6) in the temperature range of interest. This means that the 2.5 grams of getter will last 210 days without possibility of embrittlement and can last up to 1.5 years with some probability of embrittlement and particulation. Aluminide coating was done only on the outside. Interestingly, the coating effectiveness seems to be increasing with temperature.

The Nitride coating did not work in this experiment as the coating was applied on both inside and outside surface of the cell wall and there was a lot of outgassing from the inside coating which masked the reduction in hydrogen permeation due to the outside coating. Even with Nitride coating only on the outside, it is suspected that the coating may not last long at the cell operating temperatures.

A wall thicker than 0.028" can probably not be used due to the increase in parasitic conduction losses but the cell wall can be made out of an alloy which is expected to cut the permeation rate down by another factor of at least 2 or 3 (if not an order of magnitude as the literature indicates). This will increase the life of 2.5 grams of getter by another 210 days at the minimum, for a total of about 420 days of getter life without embrittlement.

All the numbers here are conservative estimates so the getter life will be longer than calculated for all the cases above. For example, there is a factor of 2 conservative estimate in the hydrogen concentration used for the present test, factor of 5 if getter embrittlement is not an issue, factor of 2 with cell walls made of a Nickel based alloy and finally, there is no reason why we cannot put 15 grams of getter instead of 2.5 grams to give us another factor of 6 margin on cell life. All these permeation resistance ideas combined together can increase the burner heated AMTEC cell life to more than 10 years.

On the other hand, this experiment and calculations also indicate that to eliminate speculation we will either need to design more tests to evaluate life of AMTEC on burner using the solution schemes suggested above or we will need to modify the cell design (include porous walls, hot fingers, etc.) to eliminate the hydrogen permeation problem in a combustion environment if we want the AMTEC cells to operate for more than a couple of years.

SOLUTION STRATEGY

Use of getters is a well known strategy to clean vacuum systems. The getters operate by pumping on all active gases including hydrogen. Based on the present experiments it may be concluded that if sufficient getter is placed inside AMTEC cells, the AMTEC cell life can be enhanced for desired lengths of operation. Getters will also help in reducing the bake-out time in AMTEC cells. Another crucial issue is how and where to place the getter so that it is most effective with least disruption to cell operation.

In the proposed solution, getters may be placed at two locations. One, a getter foil concentric with the cell wall near the hot end and two, pellets packed inside a gas porous inert container near the cold end. The foil near the hot end is anticipated to do multiple tasks. It will act as a second barrier (after cell wall) for hydrogen permeation. This will force the permeating hydrogen to move towards the condenser in the channel between the foil and the cell wall. The balance of the permeating hydrogen will be sorbed by the getter foil. Since this getter is close to the hot end, it may regenerate (part of the sorbed hydrogen will be released). This hydrogen will also be flushed towards the cold end by the flowing sodium vapor. This will allow none or minimal amounts of hydrogen to reach the BASE brazes. Since the getter is regenerated continuously it is not expected to reach the embrittlement limit. The hydrogen collecting near the condenser will be sorbed by the getter pellets tacked to the first rib on the cell wall near the cold end so the condenser will not be blocked. The pellets might sorb

enough hydrogen over the life of the cell to become brittle but since they are contained in a gas porous container, getter particulates will not be able to float around inside the cell.

In the other design, getter pellets are placed near the cold end as before but towards the hot end the getter foil is wrapped around the individual BASE tubes. The benefits remain the same. The decision as to which concept should be used will be based on manufacturability and modeling (of pressure drop) in both cases.

Other possibilities include placing the getter foil under the wick near the condenser end, using a getter foil instead of pellets near the condenser end or making the heat shield out of getter material. The preferred embodiment is placing the getter pellets inside a inert gas porous container near the cold end and a getter foil on the inside surface of the cell wall (but not touching) near the hot end. Getter alloys may be placed in AMTEC cells in other ways and forms (e.g., strips, pills, washers, even coatings). Getters may also be placed in AMTEC cells even if they are not exposed in a hydrogen environment. This will reduce the bake-out time since active gases such as oxygen and nitrogen are also permanently fixed by the getters.

ACKNOWLEDGMENTS

This work is supported by R&D budget of AMPS, Inc.

REFERENCES

1. Alger, D. L., "Effective use of Hydrogen in Stirling Engines," *Proceedings of the 23rd Intersociety Energy Conversion Engineering Conference*, Denver, CO, July 31-August 5, 1988, The American Society of Mechanical Engineers, New York, Vol. 1, pp. 79–86, 1988.
2. Anderson, W. G., Hartenstine, J. R., M. T. North and L. Lundberg, "Hydrogen-Tolerant Heat Pipes for Bimodal Systems," *Proceedings of the 30th Intersociety Energy Conversion Engineering Conference*, Orlando, Fl, July 31-August 4, 1995, The American Society of Mechanical Engineers, New York, Vol. 1, pp. 679-684, 1995.
3. Birnbaum, H. K. and Wert, C. A., "Diffusion of Hydrogen in Metals," Journal of Metals, Vol. 76, pp. 806–816, 1972.
4. Garber, J. H., "Studies of the Permeation and Diffusion of Tritium and Hydrogen in TFTR," WFPS-TME-012, October 1975.
5. Khalili, K. Godett, T. M., Meijer, R. J. and Verhey, R. P., "Design and Testing of a Heat Pipe Gas Combustion System for the STM4-120 Stirling Engine," *Proceedings of the 24th Intersociety Energy Conversion Engineering Conference*, Washington, D.C., August 6-11, 1989, The Institute of Electrical and Electronics Engineers, New York, Vol. 5, pp. 2283–2287, 1989.
6. North, M. T. and Anderson, W. G., "Hydrogen-Resistant Heat Pipes for Bimodal Reactors," *Proceedings of the 1st Conference on Synergistic Power and Propulsion Systems Technology*, Albuquerque, NM, January 26-30, 1997, American Institute of Physics, New York, AIP Conference Proceedings 387, Vol. 1, pp. 345–352, 1997.
7. Sievers, R. K., Pantolin, J. E. and Svedberg, R. C., "Series II AMTEC Cell Design and Development," *Proceedings of the 32nd Intersociety Energy Conversion Engineering Conference*, Honolulu, HI, July 27-August 1, 1997, American Institute of Chemical Engineers, New York, Vol. 2, pp. 1125-1129, 1997.
8. Strehlow, R. A. and Savage, H. C., "The Permeation of Hydrogen Through Structural Metals at Low Pressures and Metals with Oxide Film Barriers," *Nuclear Technology* 22, p. 127, 1974.
9. Weber, N., "A Thermoelectric Device Based on Beta-Alumina Solid Electrolyte," *Energy Conversion* 14, pp. 1-8, 1974.

Appendix C.

33rd Intersociety Engineering Conference on Energy Conversion
Colorado Springs, CO, August 2-6, 1998

INVESTIGATIONS OF DC ELECTRICAL DISCHARGES IN LOW-PRESSURE SODIUM VAPOR WITH IMPLICATIONS FOR AMTEC CONVERTERS

Adrian Barkan
Advanced Modular Power Systems, Inc.
4667 Freedom Drive
Ann Arbor, MI 48108
(734) 677-4260
abarkan@ampsys.com

Thomas K. Hunt
Advanced Modular Power Systems, Inc.
4667 Freedom Drive
Ann Arbor, MI 48108
(734) 677-1262
thunt@ampsys.com

ABSTRACT

Upcoming designs for AMTEC modules capable of delivering as much as 150 watts will see the introduction of higher voltages into sodium vapor at pressures spanning a wide range. In theory, with any value for two out of three parameters: voltage, pressure, and electrode geometry, a value exists for the third parameter where DC electrical breakdown can occur; due to its low ionization energy, sodium vapor may be particularly susceptible to breakdown. This destructive event is not desirable in AMTEC modules, and sets a limit on the maximum voltage that can be built-up within any single enclosed module. An experimental cell was fabricated with representative electrode configurations and a separately heated sodium reservoir to test conditions typically expected during start-up, operation, and shutdown of AMTEC cells. Breakdown voltages were investigated in both sodium vapor and, for comparison, argon gas. The dependence on electrode material and polarity was also investigated. Additional information about leakage currents and the insulating properties of α-alumina in the presence of sodium vapor was collected, revealing a reversible tendency for conductive sodium films to build up under certain conditions, electrically shorting-out previously isolated components. In conclusion, safe operating limits on voltages, temperatures, and pressures are discussed.

I. INTRODUCTION

In present day AMTEC systems, individual "cells" providing a limited amount of current and voltage are connected in series and parallel to form power supplies.[1] For purposes of efficiency, a number of β-Alumina Solid Electrolyte (BASE) tubes, all fed in parallel from a common sodium vapor source, are electrically connected in series within a cell to build-up a larger voltage. For example, in the Pluto Express (PX) cell design,[2] six BASE tubes are connected so that the cell has a maximum open-circuit voltage six times larger than a single BASE tube provides. In a future cell design, as many as 48 BASE tubes may be connected in series giving voltages as high as 72 volts.[3] Components inside the cell placed within 1-2 mm of each other may have the maximum voltage difference between them, and at the same time they are surrounded by low-pressure sodium vapor. In a simple model, two pressures are found inside a cell: the vapor pressure of sodium at the temperature of the hot end of the cell (850°C ↔ $9 \cdot 10^4$ Pa) and of the cold end of the cell (350°C ↔ 20 Pa). During start-up of the cell as it is heated from room temperature to the operating temperatures, some voltage is usually present in the cell and a wide range of sodium vapor pressures is encountered. Thus, during normal operation, one may have hot electrodes at 1-100 volts and sodium vapor pressures of $0\text{-}9 \cdot 10^4$ Pa.

These conditions are conducive to several electrical phenomena which may occur at high temperatures and/or in low-pressure gases. Specifically, if free electrons are created within a cell by either field emission or thermionic emission, they will make up a current which reduces the maximum power output of the cell. Furthermore, if the electric field is strong enough, the electrons may be accelerated to sufficient energies to ionize the

surrounding sodium vapor, resulting in DC electrical breakdown of the vapor. Since the ionized gas (a plasma) is highly conductive, this is effectively a short-circuit between previously isolated cell components.

In reality, the theoretical indications are that these phenomena are not likely to occur in planned AMTEC cells, as explained below. However, there exists no data which is exactly suited to the conditions in an AMTEC cell (the closest match being the literature on sodium lighting[4]). An experiment to test similar conditions and geometries is easy enough to perform so three brief experiments were performed using two different apparatuses. This paper reports the results of those experiments. In Section II additional theory is presented. In Section III the experimental setups are described. Section IV describes the experiments and the results. Finally, in Section V the conclusions from all three experiments are summarized.

II. THEORETICAL BACKGROUND

From previous data, it is unclear whether the suspect electrical phenomena might occur inside of an AMTEC cell. This section explains why each phenomenon was expected to be a problem, leading to the experiments described in Section III.

A. DC Breakdown

When a voltage is applied to two electrodes in a low pressure gas, the atoms/molecules of the gas may be ionized; furthermore, if ions then arrive at the cathode with sufficient energy to release secondary electrons, the breakdown process may become self-sustaining. The occurrence of DC electrical breakdown in a gas is dependent on many variables: electrode spacing, electrode shape, electrode material, electrode potential (breakdown occurs at V_b, the breakdown voltage), and gas pressure (or mean free path in the gas). Three of these variables are most strongly dependent on each other, namely the pressure, p, the electrode spacing, d, and V_b. The relationship between these three is often expressed in a Paschen curve similar to that shown in Figure 1 for argon. [5]

It can be seen in the figure that there is a minimum in the voltage needed to cause breakdown. Away from this minimum, larger voltages are needed

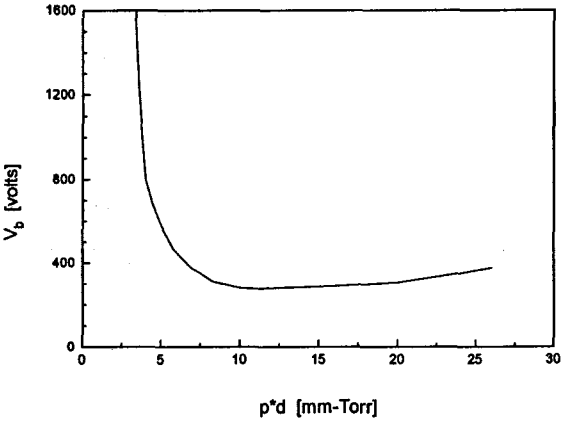

Figure 1. Breakdown voltages for brass electrodes in argon.

due to either decreased probability of collisions (smaller p•d) between electrons and atoms, or due to too frequent collisions (larger p•d).[6] In the interest of suppressing breakdown at all pressures, the minimum V_b should not be exceeded. A quick survey of minimum breakdown voltages in various gases shows values generally above 200 volts, often greater than 400 volts. While a Paschen curve for sodium vapor is not readily available, this general trend leads one to suspect that V_b will be more than 100 volts. However two other factors leave one still wondering. The first is the fact that sodium has a low ionization potential compared to species more typically used to study breakdown, so that a smaller electrode voltage is needed to create the cascade of electrons needed to sustain the plasma. The second factor is that the V_b is partly affected by the choice of electrode material. Specifically, changing the electrode material causes a change in the minimum V_b. A lower-ionization-potential electrode material causes a lower V_b, and in particular for the case of a sodium-coated electrode, V_b may be less than 90 volts.[5]

B. Field Emission and Field Ionization

Should the *electric field* between two electrodes become large enough, electrons can be emitted from the cathode and/or absorbed from passing atoms by the anode. If the freed charges are in a suitably low-pressure gas, this may trigger the DC breakdown just described. Additionally, even if a low pressure gas is not present, the field-emitted electrons would still constitute a small current between the two electrodes. Inside of an AMTEC cell, this would be an undesirable connection between otherwise isolated components, reducing the power output of the device. Typically, field emission involves very high fields,

roughly $5 \cdot 10^9$ volts/meter, and fields required for field ionization are only slightly lower.[7] Therefore, this would not appear to be an issue for AMTEC cells with maximum internal voltage drops of $\sim 10^2$ volts. However geometrical considerations cause some uncertainty. Certain electrical parts may be separated by 1 mm or less, where, for example, a parallel plate capacitor would house an electric field of 10^5 V/m. Moreover, a more representative geometry would be a sharp point (0.127mm wire cut sharply); large, diverging fields are present around pointed conductors, making it difficult to estimate their magnitude reliably.

C. Thermionic Emission

When heated sufficiently, metal surfaces emit electrons at a rate determined by the metal's work function according to:[7]

$$i_0 = 120T^2 \exp^{-\phi/kT} \text{ A/cm}^2. \qquad (1)$$

Once again, the impact of thermionic emission would at first seem to be negligible since, for example, at 850°C the emission from most metals ($\phi \approx 4.6$ eV) is about $3 \cdot 10^{-13}$ A/cm^2. But the rather low work function of sodium (2.75 eV) raises this figure eight orders of magnitude to $7 \cdot 10^{-5}$ A/cm^2. In the future when improved braze seals allow temperatures above 1000°C, a sodium-coated surface might emit 10 mA/cm^2 and this would have a measurable impact on the performance of a cell. Also, the combination of high temperatures and electric fields work together to increase the rate of electron emission, and the best way to test this is to proceed with some representative experiments.

III. APPARATUSES

Two separate experimental setups were used to investigate the above phenomena. First, an imitation cell was built using the same materials used in AMTEC cells. The cell was a stainless steel tube, 3.5 cm I.D. x 15 cm long, with projections for four electrical feedthroughs (Figure 2). Projecting from the bottom was a sealed tube, 1cm I.D. x 10 cm long. This smaller tube served as a sodium reservoir, and it's temperature could be regulated separately from the main body of the imitation cell. Inside the cell, the four feedthroughs were connected to seven different electrodes and isolated from the grounded cell wall using thick-walled alumina tubes in such a way that 14 different electrode pairings were possible (not all of them were actually used). The electrodes included: a flat stainless steel plate; a pair of fine molybdenum wires pointed at each other; another fine Mo wire pointed at the stainless steel plate; a thick (1.3 mm) wire pointed at the plate; and a completed BASE tube assembly with electrical connections to the anode, cathode, and metal weld-base. A separate tube was used to fill and evacuate the cell.

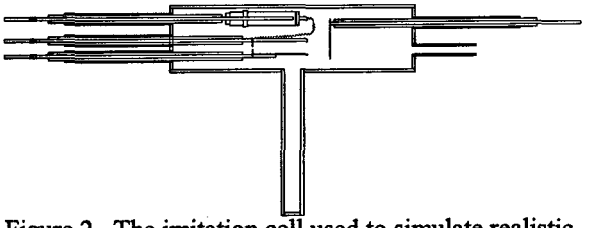

Figure 2. The imitation cell used to simulate realistic electrode configurations, showing the various electrodes, the sodium reservoir, and the pumpout line.

Another setup (Figure 3) consisted simply of a vacuum chamber for quickly arranging other electrode configurations. This chamber was unheated, so sodium vapor could not be used. The chamber was used to look for breakdown with larger electrode separations. Also, thermionic emission effects with cell materials were examined without the presence of sodium using a filament installed in this extra vacuum chamber.

A single electronic circuit was used for all the experiments (Figure 4). An adjustable-voltage, switchable-polarity power supply is connected to the cell, usually with the negative terminal grounded. The cell wall was often grounded, but it could be made to float and another electrode used for the ground. A 15000 Ω resistor was placed in the circuit so that when an arc or discharge was formed, the voltage drop would be absorbed by it, limiting the maximum current. The current and voltage were measured where shown; one of the three measurements is redundant so that results could be verified. In practice, the voltage V_0 would be increased slowly. At first, the voltage V across the electrodes is seen to be about the same as V_0. After a certain point, however, V is seen to drop suddenly (Figure 5), and the V_0 at which this occurs is the breakdown voltage V_b.

IV. EXPERIMENTS AND RESULTS

The first set of data taken was intended to show any effects of electrode geometry on the minimum

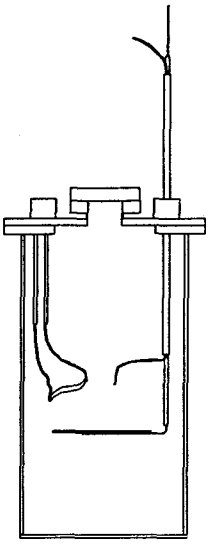

Figure 3. The vacuum chamber used for other electrode arrangements. Shown are a plate, a fine wire, and a Mo ribbon filament.

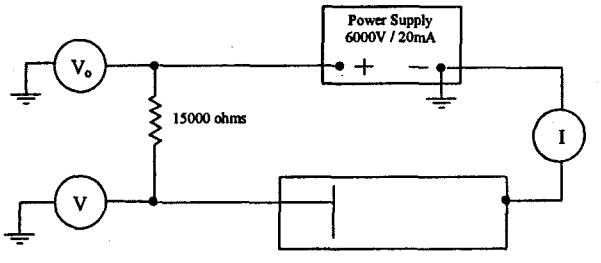

Figure 4. The circuit used to apply voltage to the cell and detect breakdown.

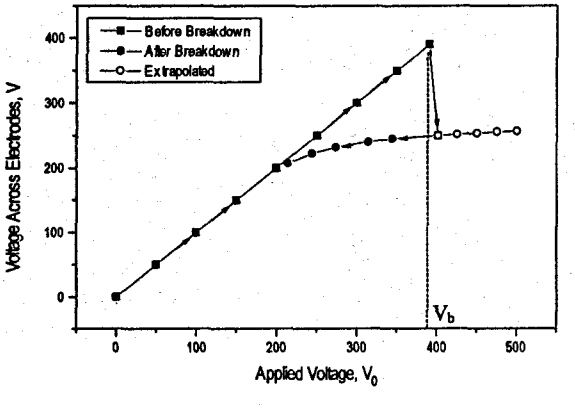

Figure 5. Evidence of DC electrical breakdown.

breakdown voltage. The assumption is made that the magnitude of change of the minimum V_b in sodium would be comparable to that in argon, since this is purely a geometrical effect. At room temperature, argon gas of varying pressure was used in both the imitation cell and in the vacuum chamber. As the pressure was changed, the breakdown voltage was noted. This was repeated for five different electrode pairs: (1) the grounded chamber walls and a stainless steel plate in the center of the vacuum chamber; (2) the grounded chamber walls and a fine Mo wire in the center of the vacuum chamber; (3) the sharp edge of the stainless steel plate, placed 1 mm from the grounded vacuum chamber wall; (4) the stainless steel plate inside the imitation cell and the grounded cell wall; and (5) the outer, Mo-screen-wrapped electrode on the BASE tube with the grounded cell wall. The results are shown in Figure 6. As expected, the minimum of the curve does vary with the geometry, but never drops below 200 volts. The lowest V_b in the graph is at 202 volts. That curve was for the BASE tube cathode which has many pointed wires where the molybdenum screen current collector is cut. Thus, it is clear that field emission is not occurring as the sole means of leakage current between cell components the way they are built in present day AMTEC cells. The spread in minimum V_b with various electrode geometries is about 150 volts. In many other data sets where the electrode pairing and polarity was varied, curves with minimum V_b comparable to those shown in Figure 6 were obtained.

The first experiment was then repeated in sodium vapor. The pressure of the sodium vapor was adjusted through the range of interest by changing the temperature of the sodium reservoir. A set of such data is plotted in Figure 7. For this data, the stainless steel plate in the cell was the positive electrode and the cell wall was grounded, so that the curve could be compared to the data points marked with "+" signs in Figure 6. The minimum V_B in Figure 7. is about 250 volts, safely above any desired internal AMTEC cell voltage. Because this electrode pair gave one of the lowest V_b values in argon, we expect the minimum seen in Figure 7 of about 255 volts is about the lowest to be encountered in upcoming AMTEC cells.

To determine if thermionic emission from the hot cell walls and cell components would reduce the breakdown voltages even further, a further experiment was performed in the vacuum chamber setup in argon gas. (It was not possible to do a

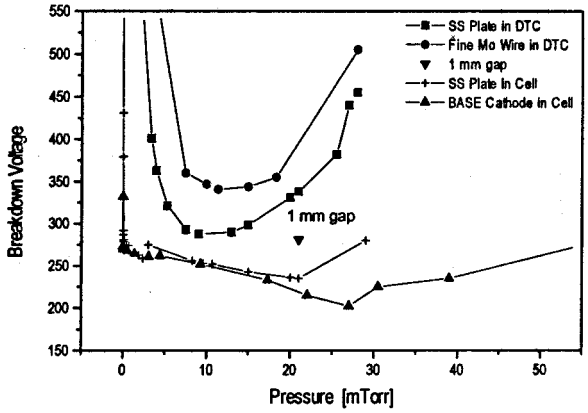

Figure 6. Breakdown voltage in argon gas.

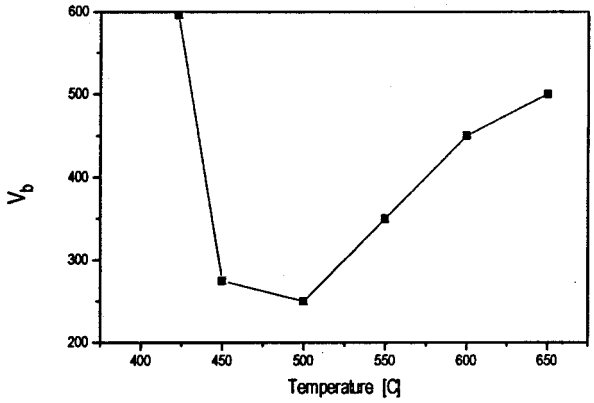

Figure 7. Breakdown voltage in sodium vapor.

simple test like this in sodium vapor because the vapor pressure is varied by changing the temperature, and the two can not be varied independently.) At a fixed argon pressure of roughly 10 millitorr (chosen to correspond with the pressure at the lowest V_b in Figure 6) the temperature of a molybdenum ribbon filament was raised and the breakdown voltage was determined. A plot of breakdown voltage as a function of filament temperature (Figure 8) shows the results. The results show that thermionic emission basically has no effect for temperatures below 1100 °C. Even above this temperature, it is not clear from the data that AMTEC cells operating at a few tens of volts would be drastically affected by the emitted electrons, since the breakdown voltage remains above 100 volts, and the emitted electrons may still not be able to cause ionization.

Figure 8. Breakdown voltage in the presence of thermionic emission.

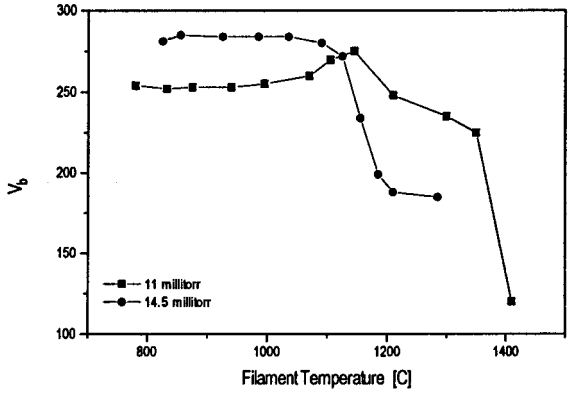

V. CONCLUSION

This concludes the planned experiments to test for the thresholds of the phenomena described in Section II. In fact, the results of the second experiment where the breakdown voltage in sodium vapor was found also partly tests *all three* phenomena simultaneously. The cell was heated to temperatures up to 850°C for that test, and since the test was performed in the imitation cell, the effect of DC breakdown would have been augmented by the small degree of thermionic emission and field effects. Therefore, the second experiment in particular puts to rest the fear that the low-pressure sodium vapor will be susceptible to breakdown when subjected to the voltages to be found in planned AMTEC cells.

The following statements can be made about acceptable parameters inside of AMTEC cells. Electrical discharges are definitely not an issue at voltages up to 40 volts. They are most likely not an issue even up to 100 volts, however another test is recommended using very closely-spaced electrodes in a sodium environment. Thermionic emission is also not an issue to worry about for the foreseeable future. However, operating temperatures greater than 1100°C will not be possible due to performance degradation by thermionic emission.

NOMENCLATURE

d	electrode spacing
ϕ	work function
i_0	emission current
k	Boltzmann's constant
p	gas pressure
T	temperature
V_b	breakdown voltage

ACKNOWLEDGMENTS

The authors would like to thank D. A. Butkiewicz and others at Advanced Modular Power Systems, Inc. for help in designing and building the imitation cell. This work was supported by the United States Department of Energy Office of Energy Research under grant DE-FG02-94ER81696.

REFERENCES

1. M. E. Carlson, J. C. Giglio, and R. K. Sievers, "Design and Fabrication of Multi-Cell AMTEC Power Systems for Space Applications," *Proc. Space Technology and Applications International Forum,* M. S. El-Genk editor, 3, 1486-1490, American Institute of Physics, Albuquerque, 1998.

2. R. K. Sievers, J. E. Pantolin, R. C. Svedberg, D. A. Butkiewicz, C. A. Borkowski, C. Huang, T. J. Hendricks, and T. K. Hunt., "Series II AMTEC Cell Design and Development," *Proc. 32nd Intersociety Energy Conversion Engineering Conference,* 2, 1125-1129, American Institute of Chemical Engineers, Honolulu, HI, 1997.

3. R. Mital, C. Huang, T. J. Hendricks, J. R. Rasmussen, R. Hundal, R. K. Sievers, "Novel Radial AMTEC Cell Design," *Proc. 33rd Intersociety Energy Conversion Engineering Conference,* paper #98-267 American Institute of Chemical Engineers, Colorado Springs, CO, 1998.

4. F. G. Spreadbury, *Electric Discharge Lighting*, Pitman and Sons, London, 1946.

5. M. Knoll, F. Ollendorff, and R. Rompe, *Gasentladungstabellen,* p. 84, J. Springer-Verlag, Berlin, 1935.

6. S. C. Brown, *Introduction to Electrical Discharges in Gases*, pp. 188-190, Wiley, New York, 1966.

7. R. Gomer, *Field Emission and Field Ionization*, pp. 1-8, 64-74, Harvard University Press, Cambridge, 1961.

Design and Testing of the Series III AMTEC Cell

Rahul Mital and Robert K. Sievers
Advanced Modular Power Systems, Inc.
4370 Varsity Drive
Ann Arbor, Michigan 48108 USA
(734) 677-4260 Phone (734) 677-0704 Fax
rmital@ampsys.com

ABSTRACT

This paper describes the design and testing of the Series III (S3) Alkali Metal Thermal to Electric Converter (AMTEC) cell which is capable of high efficiency (15-25%) and high power density (100-150 W/kg). Compared to the Series II cell which is being developed primarily for space power systems, the Series III cell design provides a significantly higher beta"-alumina solid electrolyte (BASE) tube packing density around the heat source thereby increasing cell power and minimizing heat loss. The prototype S3 cell will have 96 BASE tubes and is expected to produce about 150 We. In this cell design the BASE tube assemblies are mounted on a cylindrical tube support plate. The BASE tubes are arranged like spokes on a wheel. The inner cylinder, concentric to the tube support plate, is the hot side of the cell and the outer cylinder is the condenser.

Since the prototype S3 cell will be the first of its kind, an engineering cell with same dimensions as the prototype but with 24 BASE tubes was built first. The purpose of this cell was to identify and resolve structural, thermal, manufacturing and sodium management issues before launching into the build of a complete 96 BASE tube cell. The engineering cell has been successfully built and tested. The data of the engineering cells have been used to calibrate the SINDA/FLUINT code to predict the prototype cell performance more accurately. The build of the prototype 96 BASE tube cells is now in progress.

This paper presents the design and development of the prototype S3 cell. The fabrication and testing of the first S3 engineering cell is discussed next. Based on the test data of the engineering cell, the anticipated thermal performance of the prototype cells predicted by the calibrated SINDA model are also presented.

INTRODUCTION

Alkali Metal Thermal to Electric Converters (AMTEC) convert heat to electricity at high efficiency without moving parts and have low emissions when operated from combustion heat sources. AMTEC has been chosen by NASA and DOE as the advanced power technology for deep space missions requiring power levels up to a few hundred watts. The modular nature of the technology suggests that scale up in power 100 times is possible without fundamental changes in the basic technology. While assured performance numbers for large systems are not yet available, there is ample reason to believe that the inherent characteristics of AMTEC systems could provide high performance and value for any power range applications.

A variety of army and military missions, including remote site applications, ground support for the Air Expeditionary Forces (AEF) and Unmanned Aerial Vehicle (UAV) systems, will benefit significantly from light weight, portable electric power generating equipment that can function efficiently on a wide range of fuels found in field environments. AMTEC offers a great deal of promise for hybrid systems as well. A hybrid system utilizing AMTEC and a battery can potentially offer advantages of high specific energy, high energy density, high specific power, high power density, low cost and logistics for the dismounted soldier, portable power and microclimate cooling. If the microclimate cooling is done using absorptive cooling, advantage could be taken of the high quality waste heat from the AMTEC unit and the system weight could be reduced considerably.

System volume and mass are critical for practical operation of portable power systems. AMPS is working on the design and development of one such novel radial cell which is capable of higher efficiency (15-25%) and higher power density (125 W/kg or 100 W/l). This new cell design will offer improved power density, higher efficiency and reduced manufacturing cost.

AMTEC BACKGROUND

AMTEC converters are thermally regenerative concentration cells utilizing sodium as the working fluid and sodium (BASE) as the ion selective membrane through which a nearly isothermal expansion of sodium can generate high current/low voltage power at high efficiency. The principles of AMTEC operation have been described in the literature and all of the basic characteristics have been successfully demonstrated in many laboratory trials (Cole, 1983). Recent advances in AMTEC cell design have led to greatly simplified assembly and operating procedures and enhanced durability (Sievers et al., 1997). Performance analyses suggest that AMTEC can provide a very competitive option for high power systems. With the extensive data on AMTEC performance under known temperature conditions, the major issues in design of complete cells and systems involve efficient coupling of the heat source to the BASE tubes, which are the critical elements at the heart of AMTEC cells.

MAPPS SYSTEM OVERVIEW

The prototype Multi-Fuel AMTEC Portable Power System (MAPPS), shown in Fig. 1, contains four series-connected annular AMTEC cells. Each cell produces 145 W at 8 V: total power production is 580 W projected to be at 32 V. Cell conversion efficiency (thermal to electric) is expected to be approximately 18%. Overall system efficiency (fuel to net electric) is approximately 12%. The parasitic power requirements are estimated to be approximately 50 W at start-up and approximately 80 W at full power.

The four AMTEC cells are stacked to form the enclosure for the combustion system. The combustion system is composed of an electrostatic fuel atomizer and a radiation shield which serves to evenly distribute radiative and convective heat to the evaporating walls of the AMTEC cells. The combustor is supplied preheated air by a reverse flow, radially configured recuperator which also provides tangential air entry to the combustor for aerodynamic swirl stabilization. The condensing walls of the AMTEC cells are impingement cooled with air supplied from two vaneaxial blowers. The spent cooling air is mixed with the recuperator exhaust gasses so as to reduce thermal signature. A portion of this oxygen rich mixture is drawn from the exhaust stack into the recuperator and combustion system with a rotary vane blower.

The prototype system weight is estimated at 10.7 kg, within 20% of the Phase I weight goals. The four AMTEC cells account for 49% of the system weight. The heaviest components in the rest of the system are the recuperator (10%), the outer housing/condenser (7%) and the combustor radiation shield (6%). An optimized design making use of two larger AMTEC cells operating at 15 V each could meet the 9 kg weight goal. The weight savings are attributed to: elimination of several annular cell walls; replacement of the current 0.25" evaporator design with a 0.125" design, thereby allowing 10-12% more BASE tubes per unit heat input area; and reduction of the cell stack height.

AMTEC CELL DEVELOPMENT

The Series II cell, shown in Fig. 2, is cylindrical in shape. It is about 4 inches long and 1.5 inches in diameter. It has five main components designed to effectively control the small amount of sodium inventory required for the conversion process, the condenser, the artery, the hot end, the BASE tubes and the cell walls. This cell produces anywhere from 4-6 W depending on the operating temperature. The MAPPS power supply under development called for a novel AMTEC cell configuration called the S3 cell, also shown in Fig. 4. The MAPPS cell is of annular configuration, with the inner diameter of the cell being the evaporator or hot side and the outer diameter the condenser or cold side. Each cell contains 96 BASE tubes and 12 evaporators, arranged in three rings.

There are various advantages of the S3 cell over the Series II (S2) cell. The S3 cell provides a higher power density because it has more BASE tubes per unit area. The compactness reduces non-power producing regions in the cell, cutting down on system heat losses. The radial arrangement opens up the vapor flow channels and hence reduces pressure drop. The radial configuration with hot zone in the center is compatible with most heat sources.

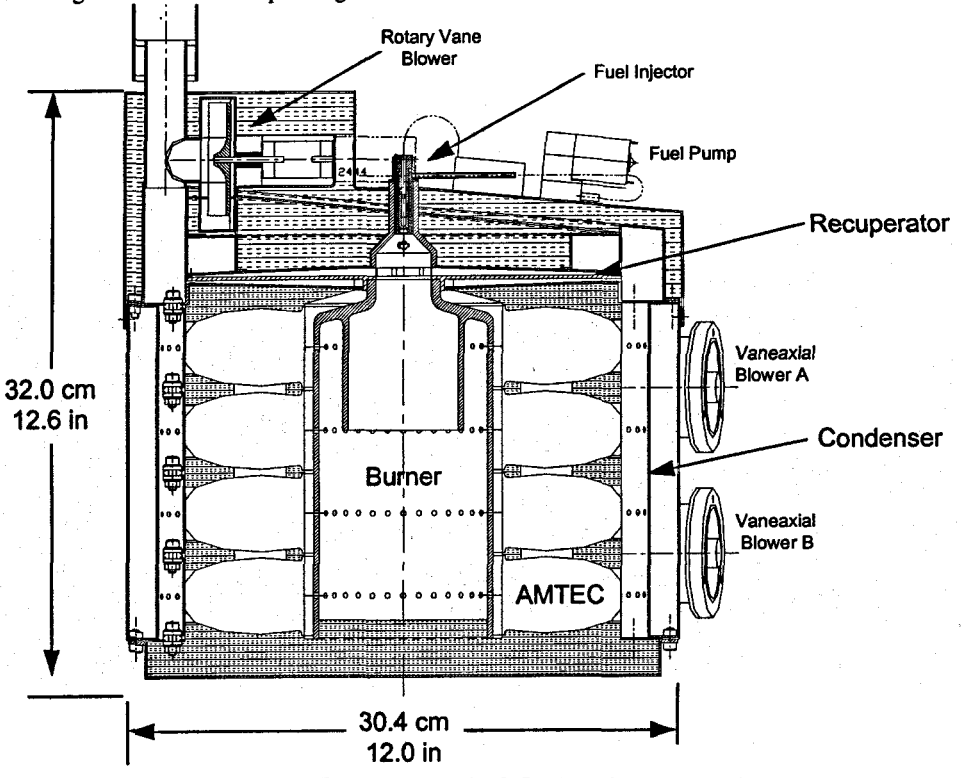

Figure 1. Prototype MAPPS System Arrangement

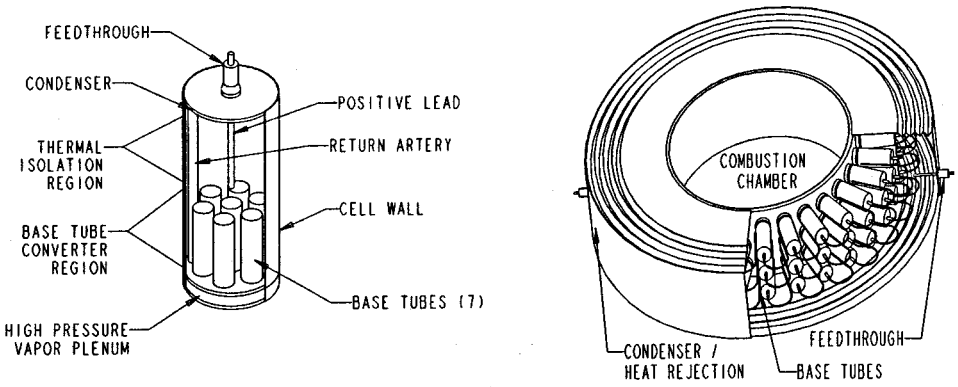

Current Multi-tube Cell Configuration **Proposed MAPPS Cell Configuration**

Figure 2. Current P_x cell and proposed MAPPS cell schematics

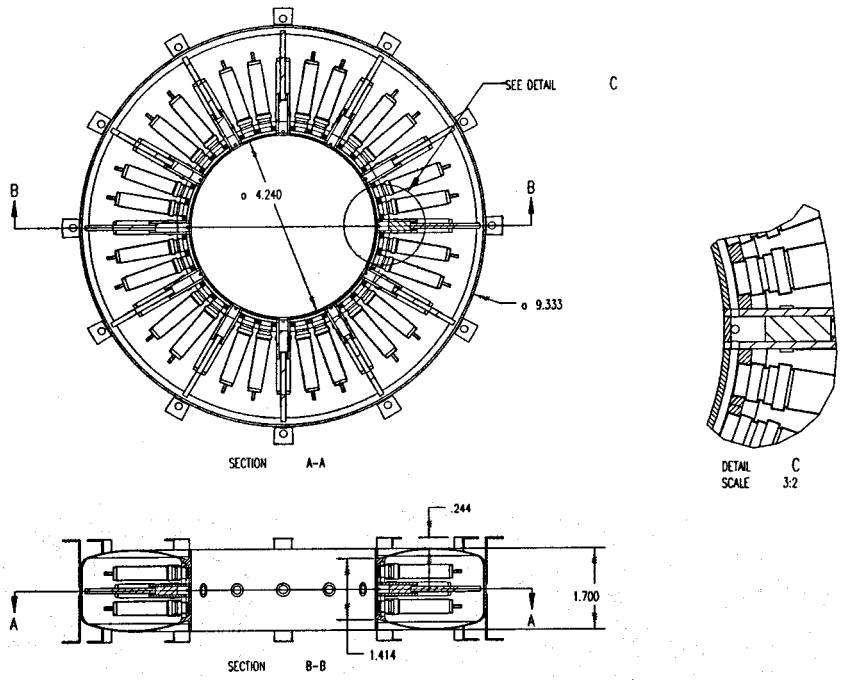

Figure 3. Schematic of the MAPPS cell

The novel cell design, shown in Fig. 3, is specifically configured to optimize thermal efficiency. The cell design is the result of a complex series of tradeoff analyses among the many competing performance requirements: low mass, low volume, high power, high efficiency, good structural integrity, etc. The internal diameter of the cell is 10.7 cm while the outer diameter is 23.7 cm. The cell height is approximately 4.3 cm. The cell mass is expected to be less than 1300 grams. The break-down of the weight estimates is provided in Table 1.

Cell Structural Analysis

The cell structural performance was evaluated using COSMOS/M finite element analysis model. A solid model was developed in Pro/Engineer, which was meshed and imported electronically to COSMOS/M for structural analysis. The structural performance of the AMTEC cell was analyzed and optimized using a multi-dimensional, 11364-element COSMOS/M analytic design model. To simulate the clamping mechanism of the cell three nodes were used. One node was constrained in all six degrees of freedom and the remaining two nodes were constrained in the vertical direction. The materials used for structural

analysis were Haynes-25 for the cell wall and hot end, nickel for the BASE support plate and stainless steel for the cell cold end. Three separate structural design analyses were performed on this cell design (fatigue, creep and buckling), with the goal of establishing acceptable margins of safety while minimizing cell mass. The structural analyses were performed with the entire structure at the anticipated cell operating temperatures, so that the appropriate thermal expansion stresses associated with full operation are simulated in the analysis.

Table 1. MAPPS cell component weight estimates

Component	Weight (g)
Hot end	177
BASE support	95
Domes	171
Cold end	78
12 evaporators	163
BASE tubes	460
TOTAL	**1143**

(Additional weight: felt material, sodium, feedthroughs.)

1. Fatigue Analysis. After optimization, the design chosen was such that the maximum strain was 0.3% and the cell could withstand more than 1000 thermal cycles without danger of fatigue failure. The cell walls and condenser are 0.38 mm thick, the hot end is 1.27 mm thick and the BASE support plate is 1.52 mm thick. The thermal expansion showed that the maximum displacement at the hot end where the strain is about 0.3%.

2. Creep Analysis. Plastic deformation of the Haynes 25 cell wall as a function of time under a constant atmospheric load was also investigated. The maximum creep stress under atmospheric pressure load was found to be 2.6 ksi. The rupture stress of Haynes 25 at 1700°F (925 °C) is about 8 ksi, thereby giving a margin of safety of over 3.

3. Buckling Analysis. A factor of safety slightly higher than 2 was obtained in the buckling analysis under a constant atmospheric load. In general, for a new design, a factor of 3 or more is preferable to work with. That can be achieved by increasing the condenser wall thickness. This, however, dramatically increases the weight of the cell since the condenser diameter is large. The above results are summarized in Table 2.

Table 2. Summary of structural analysis

Analysis	Max. Stress	Comments
Thermal expansion for material fatigue	71.5 ksi	Maximum strain is 0.3%. Material can stand more than 1000 cycles.
Creep stress under pressure load	2.6 ksi	Rupture stress of Haynes 25 at 1700 °F (925 °C) is about 8 ksi.
Buckling under pressure load		Buckling load factor is 2.08.

Cell Thermal Analysis

The thermal/electrical performance of the cell was a critical design driver in the design development process. A coupled fluid dynamic/thermal/ electrical model was developed for the cell to investigate and quantify the critical design performance tradeoffs. The SINDA, FLUINT, RadCAD model contained approximately 112 nodes and integrated all the thermal, fluid dynamics and electrochemical effects of the AMTEC cell. Due to the symmetry of the cell only one section of the cell consisting of 8 BASE tubes and one evaporator was analyzed. After developing the model, which has been well calibrated in the past using P_X-cell test data, a number of parametric studies were performed to optimize the cell design.

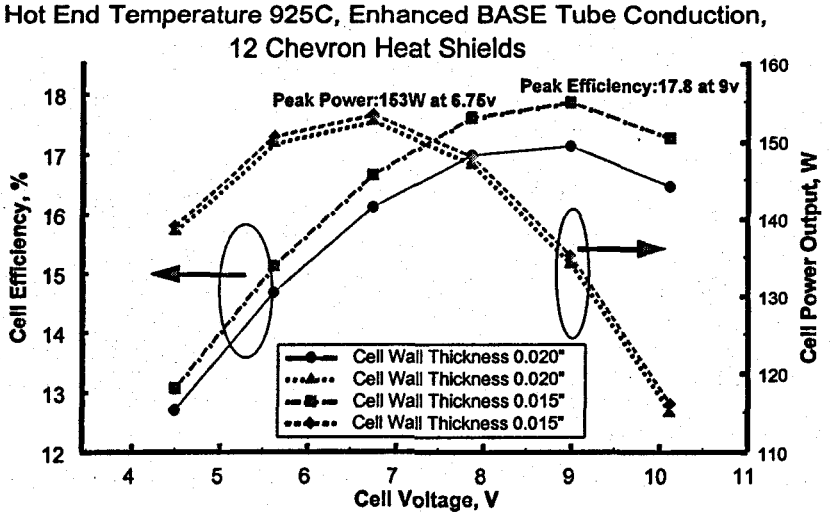

Figure 4. Effect of wall thickness on cell performance

Figure 4 shows the effect of cell wall thickness on cell power output and efficiency. Thicker cell walls increase the parasitic conduction loss, thereby decreasing the cell power output and efficiency for a fixed hot end temperature. However, decreasing cell wall thickness reduces the structural integrity of the cell so there is a trade-off. Nevertheless, for the cell wall thickness of 0.015" (0.38 mm) for which the cell is structurally sound (as shown in the structural analysis above), the present cell can achieve almost 18% efficiency and a peak power of more than 150 W. This cell design uses chevron shaped heat shields to reduce radiative losses inside the cell and keep the thermal gradient along the length of the BASE tubes as low as possible. The radial dimension of the cell was also optimized. A smaller cell radial length is advantageous because of the resulting low cell mass. However, a small cell radial length promotes conduction and radiation losses and hence decreases the cell efficiency. The analysis indicates that a 3" (7.5 cm) cell length has better performance than both the 2.5" and 3.5" cell lengths but the difference between 2.5" and 3" is marginal. The specific power was highest for the 2.5" (6.35cm) cell, hence this length was chosen for the present design.

ENGINEERING CELL

Since series III cell is a completely new design, there were a number of issues that needed to be resolved. Therefore, the first radial cell that was built did not have all the 96 BASE tubes in it. This cell, called the Engineering Cell, had only 24 BASE tubes. Primarily, it was built to identify the manufacturing issues involved, such as sequence of assembly, condenser felt design, effect of welding on cell dimensions, bake out and sodium filling of the cell. This cell provided information about issues such as sodium management (thermal and fluid) and cell structural integrity. The data collected from this cell was used to validate the cell model. The engineering cell is illustrated in Fig. 5.

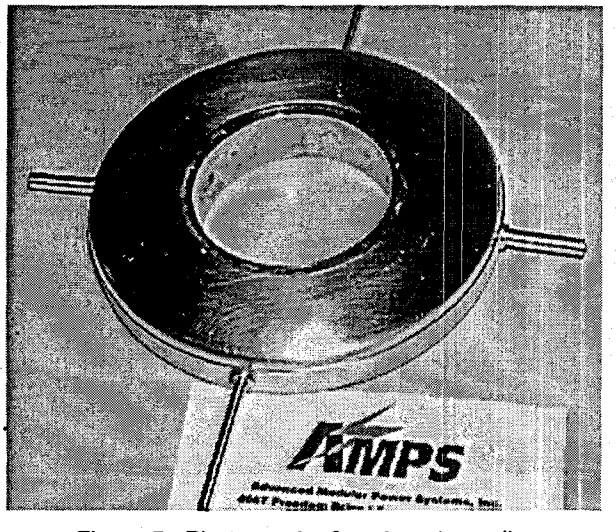

Figure 5. Photograph of engineering cell

This cell was not expected to perform as well as the complete prototypes because the operating temperature range was limited due to the stainless steel walls, the heat loss from the hot end to the cold end of the cell was higher because of absence of top and bottom row of BASE tubes and the evaporator had been pushed back from the hot end to keep the temperature margin (difference between BASE and evaporator temperature) positive. Nevertheless, the successful building and testing of this cell was crucial for the program. Proving the radial cell can be built and that the radial design concept works were the biggest technical hurdles of the program.

Instead of the regular heat shields, a new design feature was used to improve the performance of the radial cell. A molybdenum sleeve was installed on the outside of the BASE tubes. Since the heat input is from the bottom of the BASE tubes, the molybdenum sleeves improve performance by conducting more heat along the length of the BASE tube and by cutting down on the radiation heat loss from the BASE tubes due to their reduced emissivity. SINDA/FLUINT model predictions for the engineering cell with the molybdenum sleeve are given in Tables 3 and 4. In Table 3 the emissivity of the BASE is assumed to be that of Beta alumina while in Table 4 it is assumed 0.3 which is more representative of molybdenum. The two tables separate the radiative effect of the molybdenum sleeve. From Table 3 we can see that as the stand off length (distance between hot end and evaporator) increases, the peak power decreases while the temperature margin increases. A positive margin must be maintained in order to eliminate the possibility of internally shorting the inner electrode to the mounting plate as a result of sodium condensation. In Table 4 the standoff length is fixed and the cell performance is tabulated for two values of cell voltage. The model predicts a temperature margin of 59.6°C and peak power of about 22 watts at 681°C evaporator temperature.

ENGINEERING CELL TEST RESULTS

The cell was heated using a hot end heater and two cell wall heaters. The pumpout ports extending out from the condenser end were also kept hot using heater tapes to prevent any sodium condensation in its tubes. These ports will be pinched off in the prototype cells. The condenser was kept at the desired temperature using impingement cooling. The cell was instrumented with four hot end thermocouples, four cold end thermocouples, two BASE tube thermocouples, two evaporator thermocouples and one tube support plate thermocouple. The thermocouples were placed uniformly around the circumference in each case to verify radial uniformity. There were two electrical circuits in the cell, each circuit consisting of 12 BASE tubes.

Representative temperature data for the various thermocouples are given in Table 5. The hot end thermocouples showed the most variation in readings (±30°). The hot end thermocouples are sandwiched between the hot end wall and the heater coil. The huge variation could be because, in some cases, the thermocouple bead was actually reading the heater coil temperature rather than the hot end temperature. The cold

end variation was smaller (±15°) and could easily be due to non uniform air flow in the impingement cooling process. The evaporator and base temperatures are listed in the Table and indicate reasonable radial uniformity during cell operation.

The test results of the engineering cell are given in Tables 6. The power of the cell is plotted as a function of the evaporator temperature in Fig. 6. The solid circles are the test data. The continuous line is the best fit curve for the test data. Using that correlation the open square is an extrapolated test data point. The open triangles are the SINDA model predictions. As can be seen from Fig. 7, the test data matches well with the predicted values. This being a stainless steel cell, we chose not to push the cell temperatures any higher, but the extrapolated value of the test data matches the predicted results within 10%. The AMTEC technology took a huge step forward when the engineering cell operated as expected. The data was also very useful for model validation and calibration purposes.

The experimental BASE tube temperature was not used to plot the results in Fig. 6 because it was quite possible that the actual BASE temperature was lower than the thermocouple reading. This cell was only 6.35 cm long (distance between cold end and hot end). Therefore, the top end of the BASE tube was very close to the relatively cold condenser. The thermocouple which was on the inside of the BASE tube was probably a few degrees higher than the actual outside temperature of the BASE tube.

The test results of the Engineering cell were used to fine tune the model further. Due to the uncertainty in the hot end temperature, the tube support plate (TSP) temperature was used to calibrate the model. The minor modifications made to the program were; changed Rct from 0.15 to 0.2, changed electrode parameter B from 240 to 168 and the conduction paths and parameters were improved. The predictions of the tuned model are given in Table 7. The results, including the predicted BASE and evaporator temperatures match well with the test data in Table 6. Based on these revised parameters the performance of the prototype cell is predicted in Table 8. The peak power at 900°C is 130 W. At 925°C it will be lower by a few percent from the originally anticipated 150 W. The first prototype cell has been fabricated and is ready for bake out, sodium fill and testing. The partially assembled cell is shown in Fig. 7.

Table 3. Prediction of engineering cell performance (with molybdenum sleeve on BASE and emissivity = 0.95)

No.	Standoff Length (mm)	Temperature Margin (C)	Peak Power (W)	Voltage (half circuit) (V)	Current (A)	T_{BASE} (K)	T_{ev} (K)
1	9.9	4.5	23.0	3.75	3.07	985.9	981.4
2	13.8	26.0	21.2	3.75	2.83	988.1	962.2
3	24.5	82.8	14.9	3.75	1.98	986.3	903.5

Table 4. Prediction of engineering cell performance (with molybdenum sleeve on BASE and emissivity = 0.3)

No.	Standoff Length (mm)	Temperature Margin (C)	Peak Power (W)	Voltage (half circuit) (V)	Current (A)	T_{BASE} (K)	T_{ev} (K)
1	13.8	59.6	22.1	3.75	2.94	1014.1	954.5
2	13.8	22.8	17.0	3.75	1.42	1018.1	996.0

Table 5. Temperature data of the radial cell under different operating conditions

No.	Operating condition	Hot End (K)	Cold End (K)	BASE A (K)	BASE B (K)	EVAP A (K)	EVAP B (K)
1	Bake out	773	648	747	747	732	734
2	Testing	1073	623	903	918	865	861

Table 6. Engineering cell test results (with molybdenum sleeve on BASE)

No.	TSP (K)	Wall (K)	Cold End (K)	BASE (K)	Evap (K)	Peak Power (W)
1	945	873	573	833	778	3.2
2	994	923	573	868	817	4.6
3	1039	923	573	888	832	5.72
4	1015	973	623	911	867	6.6
5	1068	988	623	953	888	9.32
6	1116	1008	623	993	918	13.64

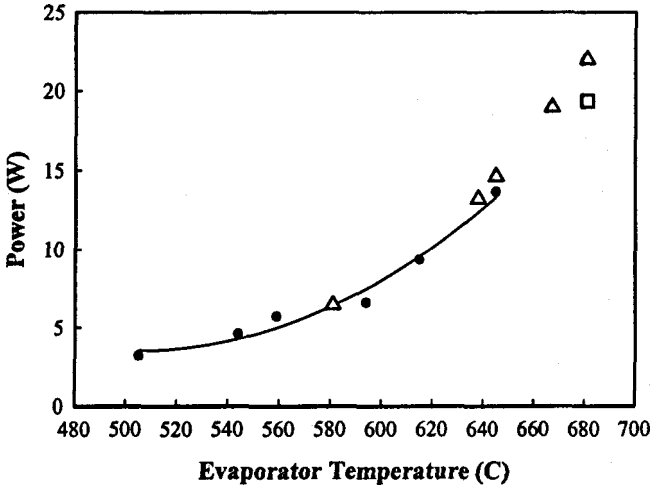

Figure 6. Test results of the engineering cell and comparison with model (• test data, Δ model predictions, □ extrapolated test data)

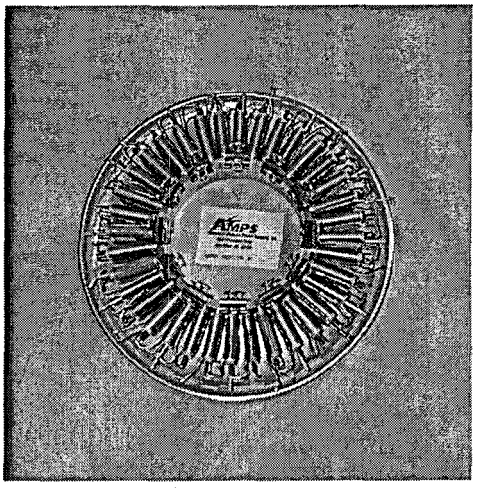

Figure 7. Status of the prototype 96 BASE tube cell

Table 7. Engineering cell model prediction

No.	TSP (K)	Voltage (V)	BASE (K)	Evap (K)	Peak Power (W)
1	1019	3.75	929	878	3.56
2	1067	3.75	963	897	5.10
3	1116	3.75	997	916	6.85

Table 8. Prototype cell model prediction using calibrated model

No.	Hot End (K)	Voltage (V)	Efficiency (%)	Peak Power (W)	BASE (K)	Evap (K)	Temp. Margin (C)
1	1173	6.75	13.9	130	1069	1049	20

SUMMARY

Significant progress has been made in developing the Series III cell. The higher power density, efficiency and modularity make this cell design suitable for numerous applications including MAPPS, solar AMTEC and cogeneration. The successful fabrication and testing of the engineering cell eliminated the biggest technical hurdle for the MAPPS program. The major issues now are manufacturing and cost of the cell, but no further technical hurdles in terms of thermal performance are expected from the prototype cell.

There are some short lead time design changes, like contact resistance, surface coatings and thinner cell walls which can further improve the performance of the cell by a few watts in power and a point or two in efficiency. Some long lead time design changes like the liquid anode concept, longer and bigger diameter BASE tubes can improve the cell performance by a couple of tens of watts and three to four points in efficiency.

Prototype hardware has been fabricated for the MAPPS program and work in the near future will focus on the separate testing and experimental optimization followed by the fabrication and testing of a prototype integrated power supply.

ACKNOWLEDGMENTS

This work was carried out under the support of DARPA and the Army Research Office. The authors would like to acknowledge the support and valuable contributions of Dick Paur at ARO, Jay Stedman, Bob Nowak at DARPA, and Peter Loftus and Roberto Pellizzari at ADL, Inc. Modeling work was done by Chen Huang and Terry Hendricks of AMPS, Inc.

REFERENCES

Cole, T., 1983, "Thermoelectric Energy Conversion with Solid Electrolytes," *Science* **221**, (4614) 915-930.

Sievers, R. K., Pantolin, J. E. and Svedberg, R. C., 1997, "Series II AMTEC Cell Design and Development," Proceedings of the 32nd Intersociety Energy Conversion Engineering Conference, Vol. 2, pp. 1125-1129.